

Comparison of RANS and Potential Flow Force Computations for the ONR Tumblehome Hullform in Vertical Plane Radiation and Diffraction Problems

Parker Lawrence Field

Thesis submitted to the faculty of the Virginia Polytechnic Institute and State University in partial fulfillment of the requirements for the degree of

Master of Science
In
Ocean Engineering

Wayne L. Neu, Chair
Alan J. Brown
Leigh S. McCue-Weil

April 18, 2013
Blacksburg, VA

Keywords: ONR Tumblehome, RANS, Potential Flow, Radiation, Diffraction

Comparison of RANS and Potential Flow Force Computations for the ONR Tumblehome Hullform in Vertical Plane Radiation and Diffraction Problems

Parker Lawrence Field

ABSTRACT

The commercial CFD software STAR-CCM+ is applied as a RANS solver for comparison with potential flow methods in the calculation of vertical plane radiation and diffraction problems. A two-dimensional rectangular cylinder oscillating in an unbounded fluid is first considered, and the added mass result shown to agree well with the analytical potential flow solution. Hydrodynamic coefficients are then determined for the cylinder oscillating in heave and sway about a calm free surface. Predicted values are observed to coincide with available experimental and linear potential flow results for most amplitudes and frequencies of oscillation examined. A three-dimensional radiation problem is then studied in which 1-DoF heave and pitch motions are prescribed to the ONR Tumblehome hullform in calm water at zero forward speed and F_n 0.3. Combinations of amplitude and frequency of oscillation ranging from small to large are considered. Results are compared with several potential flow codes which utilize varying degrees of linearization. Differences in the force and moment results are attributed to particular code characteristics, and overall good agreement is demonstrated between RANS and potential flow codes which employ a nonlinear formulation. The ONR Tumblehome is next held static in incident head waves of small and large steepness and zero forward speed or F_n 0.3. Force and moment time histories of the periodic response are compared with the same set of potential flow codes used in the radiation problem. Agreement between potential flow and RANS is reasonable in the small wave steepness case. For large wave steepness, the nonlinear wave response is seen to be important and the RANS solution does not generally agree well with potential flow results.

TABLE OF CONTENTS

1 INTRODUCTION.....	1
1.1 BACKGROUND.....	1
1.2 OBJECTIVE AND OUTLINE.....	3
2 COMPUTATIONAL METHODS.....	3
2.1 STAR-CCM+ RANS CODE.....	3
2.1.1 Governing Equations.....	4
2.1.2 Boundary Conditions.....	4
2.1.3 Numerical Method.....	5
2.2 OVERVIEW OF POTENTIAL FLOW THEORY.....	8
3 HYDRODYNAMIC COEFFICIENTS OF 2D RECTANGULAR CYLINDER.....	10
3.1 HYDRODYNAMIC COEFFICIENT CALCULATION.....	10
3.2 OSCILLATION IN AN UNBOUNDED FLUID.....	12
3.3 OSCILLATION IN HEAVE AND SWAY ABOUT A CALM FREE SURFACE.....	13
3.3.1 Influence of Near-Wall Grid Spacing and Time Step.....	14
3.3.2 Oscillation in Heave Results.....	15
3.3.3 Oscillation in Sway Results.....	17
3.4 ADDITIONAL PARAMETER EVALUATION.....	20
3.4.1 Turbulence Model Effects.....	20
3.4.2 Bottom Effects.....	22
4 ONR TUMBLEHOME IN PRESCRIBED MOTIONS AND WAVES.....	24
4.1 GEOMETRY.....	24
4.2 PRESCRIBED 1 DOF HEAVE AND PITCH OSCILLATIONS.....	26
4.2.1 Computational Mesh and Approach.....	27
4.2.2 Mesh and Time Step Uncertainty.....	29
4.2.3 Force and Moment Results.....	35
4.2.4 Evaluation of Simulation Parameters.....	43
4.3 FIXED 0 DOF IN HEAD WAVES.....	46
4.3.1 Computational Mesh and Approach.....	46
4.3.2 Mesh and Time Step Uncertainty.....	47
4.3.3 Force and Moment Results.....	50
4.3.4 Influence of Overset Mesh Interpolation.....	55
5 SUMMARY, CONCLUSIONS AND FUTURE WORK.....	57
5.1 SUMMARY.....	57
5.2 CONCLUSIONS AND FUTURE WORK.....	58
REFERENCES.....	59
APPENDIX A: ONRTH PRESCRIBED MOTION RESULTS.....	61
APPENDIX B: ONRTH INCIDENT WAVE UNCERTAINTY TIME HISTORIES.....	65

LIST OF FIGURES

Figure 1.	Unbounded fluid case domain mesh.....	12
Figure 2.	Corner and boundary layer mesh refinement	12
Figure 3.	Free surface case mesh	13
Figure 4.	Non-dimensional added mass (top) and damping (bottom) coefficients in heave as function of non-dimensional frequency; experimental values in black and white, RANS results in red and potential flow theory solutions using conformal mapping given by solid (best section fit mapping) and dashed (Lewis form) lines	16
Figure 5.	Hydrodynamic components of force in heave: $B/T = 4$, $\omega^* = 1.71$, $z_a = 0.03$ m	17
Figure 6.	Vorticity contours and velocity vectors in heave at $t/T = 0, 0.25, 0.50, 0.75$: $B/T = 4$, $\omega^* = 1.71$, $z_a = 0.01$ m (top) and $z_a = 0.03$ m (bottom)	17
Figure 7.	Non-dimensional added mass (top) and damping (bottom) coefficients in sway as function of non-dimensional frequency; experimental values in black and white, RANS results in red and potential flow theory using conformal mapping given by solid (best section fit) and dashed (Lewis form) lines	18
Figure 8.	$B/T = 2$ added mass (left) and damping (right) sway-roll coupling coefficients; conformal mapping solutions given by solid (best section fit) and dashed (Lewis form) lines	19
Figure 9.	$B/T = 4$ added mass (left) and damping (right) sway-roll coupling coefficients; conformal mapping solutions given by solid (best section fit) and dashed (Lewis form) lines	19
Figure 10.	$B/T = 8$ added mass (left) and damping (right) sway-roll coupling coefficients; conformal mapping solutions given by solid (best section fit) and dashed (Lewis form) lines	19
Figure 11.	Vorticity contours and velocity vectors in sway at $t/T = 0, 0.25, 0.50, 0.75$: $B/T = 4$, $\omega^* = 1.71$, $z_a = 0.01$ m (top) and $z_a = 0.03$ m (bottom)	20
Figure 12.	Total hydrodynamic force in heave: $B/T = 4$, $\omega^* = 1.71$, $z_a = 0.03$ m	21
Figure 13.	Vorticity contours and velocity vectors in heave at $t/T = 0, 0.25, 0.50, 0.75$: $B/T = 4$, $\omega^* = 1.71$, $z_a = 0.01$ m (top) and $z_a = 0.03$ m (bottom) using $k-\omega$ turbulence model	21
Figure 14.	Overset mesh in red, background mesh in blue, $B/T = 4$	22
Figure 15.	Non-dimensional added mass (top) and damping (bottom) coefficients in heave as function of non-dimensional frequency; experimental values in black and white, RANS results in color and potential flow theory using conformal mapping given by solid (best section fit) and dashed (Lewis form) lines	23
Figure 16.	ONRTH body plan.....	25
Figure 17.	ONRTH isometric view.....	26
Figure 18.	Overset mesh: acceptor cells in blue, active cells in yellow	27
Figure 19.	Background mesh: acceptor cells in blue, active cells in yellow, inactive cells in red.....	28
Figure 20.	Overset Region in red, background region in blue.....	28
Figure 21.	Grid refinement study, oscillation in heave at frequency 1.1 rad/s, amplitude 4.4 m and Fn 0.0: longitudinal force (top), vertical force (middle) and pitch moment (bottom)	33

Figure 22. Time step refinement study, oscillation in heave at frequency 1.1 rad/s, amplitude 4.4 m and Fn 0.0: longitudinal force (top), vertical force (middle) and pitch moment (bottom)	33
Figure 23. Grid refinement study, oscillation in pitch at frequency 1.1 rad/s, amplitude 5 deg. and Fn 0.0: longitudinal force (top), vertical force (middle) and pitch moment (bottom)	34
Figure 24. Time step refinement study, oscillation in pitch at frequency 1.1 rad/s, amplitude 5 deg. and Fn 0.0: longitudinal force (top), vertical force (middle) and pitch moment (bottom)	34
Figure 25. Pitch moment for oscillation in pitch at freq. 0.2079 rad/s, amp. 5 deg. and Fn 0.0	36
Figure 26. Centerline stern section free surface in pitch at freq. 0.2079 rad/s, amp.5 deg. and Fn 0.0.....	36
Figure 27. Vertical force from RANS for oscillation in heave at freq. 0.2079 rad/s, amp. 0.55 m, Fn 0.0 & 0.3	37
Figure 28. Vertical force for oscillation in heave at freq. 0.2079 rad/s, amp. 0.55 m, and Fn 0.3	37
Figure 29. Time history of free surface: heave oscillation, freq. 1.1 rad/s, amp. 4.40 m, & Fn 0.0	39
Figure 30. Oscillation in heave at frequency 1.1 rad/s, amplitude 4.4 m and Fn 0.0: longitudinal force (top), vertical force (middle) and pitch moment (bottom)	40
Figure 31. Oscillation in heave at frequency 1.1 rad/s, amplitude 4.4 m and Fn 0.3: longitudinal force (top), vertical force (middle) and pitch moment (bottom)	40
Figure 32. Oscillation in pitch at frequency 1.1 rad/s, amplitude 5 deg. and Fn 0.0: longitudinal force (top), vertical force (middle) and pitch moment (bottom)	41
Figure 33. Oscillation in pitch at frequency 1.1 rad/s, amplitude 5 deg. and Fn 0.3: longitudinal force (top), vertical force (middle) and pitch moment (bottom)	41
Figure 34. Velocity vector and vorticity contour time history from RANS for transverse section at 95% of L: oscillation in pitch at frequency 1.1 rad/s, amplitude 5 deg., and Fn 0.0.....	42
Figure 35. Comparison of temporal discretization order and fixed mesh; oscillation in heave at frequency 1.1 rad/s, amplitude 4.4 m and Fn 0.0: longitudinal force (top), vertical force (middle) and pitch moment (bottom).....	44
Figure 36. Comparison of temporal discretization order; oscillation in pitch at frequency 1.1 rad/s, amplitude 5 deg. and Fn 0.0: longitudinal force (top), vertical force (middle) and pitch moment (bottom)	44
Figure 37. Comparison of $k-\varepsilon$ and $k-\omega$ turbulence models; oscillation in heave at frequency 1.1 rad/s, amplitude 4.4 m and Fn 0.0: longitudinal force (top), vertical force (middle) and pitch moment (bottom)	45
Figure 38. Comparison of $k-\varepsilon$ and $k-\omega$ turbulence models; oscillation in pitch at frequency 1.1 rad/s, amplitude 5 deg. and Fn 0.0: longitudinal force (top), vertical force (middle) and pitch moment (bottom)	45
Figure 39. Overset (red) and background (blue) mesh: incident waves of 7.7 m amp. (top) and 1.28 m amp. (bottom).....	47
Figure 40. Extra fine mesh; overset (red) and background (blue) mesh: incident waves of 7.7 m amp.	49

Figure 41.	$H/\lambda = 60$ and $Fn = 0.0$: wave elevation (top), longitudinal force (1st middle), vertical force (2nd middle) and pitch moment (bottom)	52
Figure 42.	$H/\lambda = 60$ and $Fn = 0.3$: wave elevation (top), longitudinal force (1st middle), vertical force (2nd middle) and pitch moment (bottom)	52
Figure 43.	$H/\lambda = 10$ and $Fn = 0.0$: wave elevation (top), longitudinal force (1st middle), vertical force (2nd middle) and pitch moment (bottom)	53
Figure 44.	$H/\lambda = 10$ and $Fn = 0.3$: wave elevation (top), longitudinal force (1st middle), vertical force (2nd middle) and pitch moment (bottom)	53
Figure 45.	Time lapse of free surface at $t/T = 0, 0.25, 0.50, 0.75$: $Fn = 0.0, H/\lambda = 1/10$	54
Figure 46.	Comparison of overset and fixed mesh solutions; $H/\lambda = 60$ and $Fn = 0.0$: longitudinal force (top), vertical force (middle) and pitch moment (bottom)	56
Figure 47.	Comparison of overset and fixed mesh solutions; $H/\lambda = 10$ and $Fn = 0.0$: longitudinal force (top), vertical force (middle) and pitch moment (bottom)	56

LIST OF TABLES

Table 1. Influence of near-wall grid spacing on hydrodynamic coefficients, rectangular cylinder in heave, $B/T = 4$	14
Table 2. Influence of time step on hydrodynamic coefficients, rectangular cylinder in heave, $B/T = 4$	15
Table 3. Turbulence model comparison, hydrodynamic coefficients for heave motion, $B/T = 4$	21
Table 4. List of Force Study Codes	24
Table 5. ONRTH Particulars	25
Table 6. Prescribed Oscillation Cases	26
Table 7. STAR-CCM+ Abbreviations	26
Table 8. Verification parameter results: heave, frequency 1.1 rad/s, amplitude 4.4 m, Fn 0.0	32
Table 9. Verification parameter results: pitch, frequency 1.1 rad/s, amplitude 5 deg, Fn 0.0	32
Table 10. Grid and time step uncertainties: high amplitude and frequency, Fn 0.0	32
Table 11. Legend for time history plots	35
Table 12. Fixed in head waves cases	46
Table 13. Verification parameter results: fine mesh, fine time step, $H/\lambda = 1/10$, Fn 0.0	49
Table 14. Verification parameter results: extra fine mesh, extra fine time step, $H/\lambda = 1/10$, Fn 0.0	49
Table 15. Grid and time step uncertainties, $H/\lambda = 1/10$, Fn 0.0	50

1 INTRODUCTION

1.1 BACKGROUND

Historically, hydrodynamicists have been able to rely on past experience and empirical data when determining the seakeeping characteristics of a conventional hullform [1]. Based on this knowledge an estimate of the limiting design conditions could be obtained with relative ease. However, recent advances in hullform design have been geared towards the development of unconventional forms such as trimarans, SWATH and tumblehome for a variety of reasons and applications. The advent of these advanced hullforms has increased reliance on experimentation and numerical simulation in order to assess their performance [2]. Because experiments are expensive, it is desirable to develop reliable computational tools which fully consider all of the relevant physics and are capable of simulating a number of conditions in a time frame reasonable for design. This is beyond the current state of the art. Instead, tradeoffs must be made in current methods between accuracy of the solution and the computational effort required.

Potential flow is a widely utilized and computationally efficient approach to modeling the flow about a ship in a seaway. This approach assumes that the flow is inviscid, irrotational, and incompressible. Generally, these methods can be categorized according to their treatment of the nonlinearities relevant to potential flow. That is, those associated with the free surface boundary conditions, nonlinear behavior of waves and body geometry. Linearization of the problem comes in assuming that motions are small and thus the nonlinear phenomena can be neglected. There are a number of theoretical approaches to both the linear and nonlinear problem. The strip theory method is a popular approach to the linear problem which assumes that the ship's beam and draft are small relative to the length and its oscillation is of a high-frequency [3]. The three-dimensional problem can then be simplified to a series of two-dimensional problems on transverse planes distributed longitudinally along the ship. In two or three-dimensions, the problem is linearized by applying the body boundary condition at its mean position and using the linearized free surface boundary condition. A boundary element method is often used which formulates the solution as singularity integrals over the surfaces bounding the fluid domain [4]. Typically this approach is referred to as a panel method since the hull geometry is discretized by elements over which some source or dipole is distributed. The strength of the singularity distributions over each panel is calculated in order to satisfy the chosen boundary conditions and computations are performed in the frequency or time domain. In the other extreme, the fully nonlinear free surface boundary conditions are considered, and a "body-exact" approach is taken which satisfies the hull boundary condition on the exact wetted surface of the body. This problem is a time-variant system and must be solved in the time domain. Typically a mixed Euler-Lagrange approach, introduced by Longuet-Higgins and Cokelet [5], is used to obtain a solution. This method has been applied successfully to steady flow (e.g. [6]). However, its applications to seakeeping computations have been limited to simple problems since it is still computationally expensive and faces difficulties due to breaking waves and stability of the time stepping method [4]. Much of the work has been to avoid these issues by suppressing wave breaking or introducing linearizations. Blended methods are an engineering approximation which blends nonlinear and linear computational techniques. Typically, they take advantage of the nonlinearities which are easily computed, i.e. satisfying the hydrostatic and Froude-Krylov components of the potential on the instantaneous wetted hull while maintaining a linear approximation of the more difficult to compute radiation and diffraction components.

Nonlinearities are the main source of difficulty in seakeeping simulations and are typically prevalent in the problems of greatest interest, such as large amplitude motions and waves. Nonlinearities in seakeeping computations stem from viscosity, velocity squared terms in the pressure equation, body geometry, free surface boundary conditions and the behavior of incident waves [4]. Potential flow solutions are able to incorporate these nonlinearities to some extent but in all cases lack viscous effects, such as flow separation, and typically cannot capture violent free surface phenomena like breaking waves. Viscous flow approximations such as Direct Numerical Simulation (DNS), Large Eddy Simulation (LES), and Reynolds Averaged Navier Stokes (RANS) have emerged with increasing computing power over the last two decades. Of these, RANS is the most computationally efficient, and best suited for analysis of ship motions in the present and near future. In this approach, the complete Navier-Stokes equations are solved on a computational grid, with models for turbulence and the free surface interface. For RANS, the entire turbulence spectrum is modeled, and only the large scales of motion are resolved. A variety of models of turbulence have been developed, including linear eddy viscosity models such as the two-equation $k-\varepsilon$ and $k-\omega$ models which are commonly used for ship hydrodynamics [7]. Free surface interfaces are typically represented by an interface tracking or interface capturing method. In an interface tracking scheme, the computational grid deforms to satisfy a kinematic boundary condition at the free surface and the governing equations are solved in the water phase. Interface capturing methods, such as Volume of Fluid (VOF), level-set, and front tracking, solve the governing equations in both air and water and are able to model large free surface deformations and green water on deck. Solutions to the RANS problem are obtained through several numerical approaches which determine the grid, discretization scheme and solution algorithms employed.

Applications of RANS to seakeeping problems have increased significantly over the past decade. Much of this work has been focused on comparison with experimental results for validation of heave and pitch in head waves. The Wigley hull [8] and DTMB 5512 [9] were examined in heave and pitch using CFDShip-Iowa with interface tracking and single-phase level set methods respectively. Predicted motions compared well with experimental data for regular, linear head waves. At the 2010 Workshop on Numerical Ship Hydrodynamics in Gothenburg, solutions for the KCS container ship and KVLCC2 tanker models in head waves were presented from five codes for validation [10]. RANS simulations have also been used to study specific phenomena such as parametric roll and roll damping. Sadat-Hosseini [11] conducted captive and free-running simulations for parametric rolling, broaching, surf-riding, and periodic motion of the ONR Tumblehome model which generally compared well with experimental results. Roll decay of DTMB 5415 and DTMB 5613-1 with and without bilge keels was examined as part of a study of the physical phenomena associated with roll damping [12]. However, computational speeds are still insufficient to viably model the large number of variants needed for design using RANS based methods. There has thus been some recent interest in comparing RANS with potential flow methods. Belknap et al. [13] compared two body-exact potential flow methods with linear free surface conditions to RANS and nonlinear potential flow codes in a series of two and three-dimensional prescribed heave tests. A S175 container ship model was examined in head seas using a RANS code and blended potential flow method by Grasso et al [14]. The Cooperative Research Ships (CRS) group conducted a systematic study in which several potential flow, RANS and other CFD codes are compared in their solutions of a container ship and ferry advancing at forward speed in regular waves [15].

1.2 OBJECTIVE AND OUTLINE

The key aim of this thesis is to distinguish to what extent current potential flow methods are able to capture the nonlinearities experienced by a ship undergoing vertical plane motions in calm water and held static in a head sea as compared to a fully nonlinear RANS solution. Section 2 gives an overview of the RANS computational method and a brief review of potential flow theory. In Section 3, hydrodynamic coefficients of a rectangular cylinder are calculated using the RANS approach. Initially, results are obtained for added mass of the rectangle in an unbounded fluid and compared with the closed-form potential flow solution. A calm free surface is then added, and hydrodynamic coefficients are determined for harmonic oscillations of several amplitudes and frequencies in heave and sway. The coefficients are compared to potential flow solutions and experimental data for validation. Effects of the RANS simulation time step, turbulence model and near-wall grid spacing on the solution are examined. Forces and moments on the ONR Tumblehome hullform model during prescribed single degree-of-freedom (DoF) heave and pitch motions and held static with an incident head wave are given in Section 4. Several amplitudes and frequencies of prescribed oscillation and two wave heights are considered such that regimes are represented where linear approximations are expected to adequately describe the flow physics and where nonlinearities are expected to be important. Predictions are compared with several potential flow codes using varying degrees of linearization which took part in a computational “Force Study” [2],[16]. A brief summary of this study and the potential flow codes which it features are given. Differences between the potential flow and RANS solutions are correlated with characteristics of each solution method to show the significance of particular sources of nonlinearity. Uncertainty in the RANS solution associated with grid spacing and time step is determined through a systematic study of solution convergence and the effect of additional simulation parameters such as turbulence models and order of the temporal discretization scheme are considered. Finally, conclusions from the study and recommendations for future research are discussed in Section 5.

2 COMPUTATIONAL METHODS

2.1 STAR-CCM+ RANS CODE

This study uses the commercial CFD code STAR-CCM+ versions 7.02 and 7.04 as a RANS solver. STAR-CCM+ is a product of CD-adapco and is a comprehensive simulation package capable of modeling and meshing geometry, employing a variety of physical models and solvers and post-processing within a single interface. The solution to a free surface flow is obtained through a finite volume discretization of the domain. A VOF method is employed to capture the position of the phase interface. The formulation is second order accurate in space and in time. Equations are solved as an uncoupled system using a segregated flow solver which employs a SIMPLE algorithm with Rhie-Chow correction for pressure-velocity coupling. The RANS equations are closed by modeling the Reynolds stress tensor using the Realizable $k-\varepsilon$ or SST $k-\omega$ turbulence model.

2.1.1 Governing Equations

The Navier-Stokes equations are given in the integral form for a cell of volume V as:

$$\frac{d}{dt} \int_V \rho dV + \oint_A \rho(\mathbf{v} - \mathbf{v}_g) \cdot d\mathbf{a} = 0 \quad (1)$$

$$\frac{d}{dt} \int_V \rho \mathbf{v} dV + \oint_A \rho \mathbf{v} \times (\mathbf{v} - \mathbf{v}_g) \cdot d\mathbf{a} = - \oint_A p \mathbf{I} \cdot d\mathbf{a} + \oint_A \mathbf{T} \cdot d\mathbf{a} + \int_V \mathbf{F} dV \quad (2)$$

Here, \mathbf{v} is the velocity, \mathbf{v}_g is the grid velocity, ρ is the density, p is the pressure, \mathbf{I} is the identity matrix, \mathbf{T} is the viscous stress tensor and \mathbf{F} is an external body force, in this case due to gravity. The face area vector is given by \mathbf{a} . The terms on the left hand side of Eqn. 2 are the transient and convective flux terms respectively. Pressure gradient, viscous flux and body force terms are given on the right hand side.

Using an eddy viscosity model, the complete stress tensor for a turbulent flow invokes the Boussinesq approximation such that:

$$\mathbf{T} = \mu_{eff} [\nabla \mathbf{v} + \nabla \mathbf{v}^T - \frac{2}{3} (\nabla \cdot \mathbf{v}) \mathbf{I}] \quad (3)$$

Here μ_{eff} is the sum of the laminar and turbulent viscosities μ and μ_t , and the superscript T indicates the transpose of the differential matrix. Turbulent viscosity is used to model the Reynolds stress tensor as a function of mean flow quantities so that the governing equations are closed.

2.1.2 Boundary Conditions

Domain boundaries control fluid flux into and out of the domain and vary for given simulation conditions. The boundaries used for a particular mesh and simulation are stated in *Sections 3 and 4*. Here the basic formulation of each boundary type is given.

A velocity inlet boundary condition permits user specification of the inlet face velocity vector. Boundary face pressure is extrapolated from the adjacent cells using reconstruction gradients.

Pressure outlet boundary conditions allow user specification of the boundary pressure. The boundary face velocity is extrapolated from interior cells. In the free surface application, the boundary pressure is governed by a field function which monitors the instantaneous pressure on, above and below the free surface at the boundary.

Symmetry plane boundaries are used to mirror the domain such that the total cell count of the mesh is reduced. The symmetry plane is commonly placed on the centerline when motion is only in the x-z plane. Shear stress at the symmetry boundary is zero. Velocity and pressure face values are extrapolated from interior cells.

A no-slip and non-penetration condition is placed on wall surfaces of the model. The wall surface tangential velocity is set to a specified value, zero in the case of no wall motion. Boundary face pressure is extrapolated from adjacent cells.

2.1.3 Numerical Method

A finite volume method is used to discretize the domain as a finite number of control volumes (CVs) corresponding to computational grid cells. The discretized conservation equations are applied at each CV in a collocated arrangement. The result is a set of coupled, non-linear equations at each CV centroid. Each equation is a function of pressure and velocity at the CV center and in all neighboring CVs. All space integrals are approximated using the mid-point method in which surface integrals are the product of the integrand at the cell face center and the area of the face and volume integrals are the product of the mean integrand value and the CV volume. These are both of second-order accuracy given that the integrand value is also computed with second order accuracy. Eqn. 2 is discretized for a cell-centered CV, leaving off the body force term, as:

$$\frac{d}{dt}(\rho \mathbf{v}V) + \sum_f [\mathbf{v}\rho(\mathbf{v} - \mathbf{v}_g) \cdot \mathbf{a}]_f = - \sum_f (\rho \mathbf{I} \cdot \mathbf{a})_f + \sum_f (\mathbf{T} \cdot \mathbf{a})_f \quad (4)$$

2.1.3.1 Transient and Convective Terms

The transient term derivative is approximated by a one-sided, second-order finite difference scheme dependent upon the solution at the current iteration, and that from the previous two time levels. The time step dt is specified by the user. Time step calculation and analysis is given in *Sections 3* and *4*.

A nominally second-order upwind scheme is used for the convection term in which velocity values at the face are linearly interpolated from neighboring cell values using reconstruction gradients (see *Section 2.1.3.6*). Limiting the reconstruction gradients introduces greater dissipation than a central-differencing scheme, helping to reduce local extrema [17]. While this method is more accurate than a first-order scheme, reduced numerical dissipation may lead to convergence issues.

2.1.3.2 Turbulence Modeling

The Boussinesq approximation given in Eqn. 3 makes use of a turbulent viscosity concept to model the Reynolds stress tensor as a function of mean flow quantities. To close the Reynolds averaged equations a turbulence model must be added which determines this turbulent viscosity value. STAR-CCM+ offers a variety of eddy viscosity models which use the stated approximation, and also permits use of several Reynolds Stress turbulence models which encompass greater complexity.

Generally, a realizable, two-layer form of the k - ε model is employed in this study. The k - ε turbulence model is a two-equation model which solves transport equations for the turbulent kinetic energy k and its dissipation rate ε . This model is widely used in industrial applications and provides a good compromise between robustness, computational cost and accuracy [17]. The realizable model contains a different transport equation for the dissipation rate, and a realizable eddy viscosity formulation which has shown improvement over the standard k - ε model. A two-layer approach is used to better capture the peaked turbulent kinetic energy and dissipation profiles near the wall [18]. The formulation blends the realizable, two transport equation model with a one-equation model which solves for k but prescribes ε and μ_t

algebraically with distance from the wall [17]. In the layer adjacent to the wall the latter formulation is used and the values of ε are blended smoothly with the two equation model values far from the wall using a blending function.

The SST $k-\omega$ model is an alternative two-equation model to the $k-\varepsilon$ formulation which is also used at points in this study. This model solves transport equations for turbulent kinetic energy k and a specific dissipation rate ω which is defined as the dissipation rate per unit turbulent kinetic energy, $\omega = \varepsilon/k$. The $k-\omega$ model generally demonstrates improved performance for adverse pressure gradients and separated flows when compared with the $k-\varepsilon$ model. However, the general $k-\omega$ model is sensitive to free stream/ inlet conditions. To solve this problem, the SST approach [19] effectively blends a $k-\varepsilon$ model in the far-field with a $k-\omega$ model near the wall.

In either turbulence model, mean flow quantities near the wall are calculated according to an all y^+ , blended wall treatment. This approach is flexible in its ability to handle a range of local mesh refinement levels near the wall. Cells with low y^+ values are assumed to be properly resolved such that no wall treatment is necessary, while cells of $y^+ > 30$ are treated as in the logarithmic region. The wall treatment affects the near wall velocity, turbulent production and turbulent dissipation.

2.1.3.3 SIMPLE Algorithm

The discretized governing equations are solved in a segregated manner using a predictor corrector approach. Here, the SIMPLE algorithm is employed. This method can be described generally as an implicit technique which calculates velocity based on a predicted pressure value then updates the pressure and velocity to satisfy continuity. The process is repeated over multiple iterations within a single time step until the difference between the discretized solution and exact solution meets some tolerance or a maximum number of iterations have occurred. The algorithm's performance is highly dependent upon the size of the time step [18].

The mass conservation equation, Eqn. 1, is discretized as:

$$\sum_f (\dot{m}_f^* + \dot{m}'_f) = 0 \quad (5)$$

Where \dot{m}_f^* is the uncorrected face mass flow rate and \dot{m}'_f is the mass flow correction necessary to satisfy continuity. A solution of the discrete momentum equations is obtained using pressure values of the previous iteration. The resulting velocity terms and a Rhie-Chow type dissipation are used in calculating the uncorrected mass flow rate. The Rhie-Chow correction is necessary for smoothing of oscillations which can occur in the mass flux of a collocated grid. Enforcing continuity yields the mass flow correction as a function of pressure correction values. Discrete equations for pressure correction are solved for in an analogous manner to the velocity values of the discrete momentum equations. The total mass fluxes and velocity terms are then updated. The process is repeated in subsequent iterations using the pressure values obtained in the previous iteration.

2.1.3.4 VOF Interface Capturing

The air-water interface at the free surface is captured using the volume of fluid (VOF) method. VOF assumes a common velocity and pressure field for all phases within a single CV, and monitors the phase fraction. The governing equations for mass and momentum continuity in a single-phase flow are thus solved for an equivalent fluid whose physical properties (density and laminar viscosity) are a function of the constituent phase's properties and volume fractions within each CV. This is often known as the volume-fraction method. The transport of volume fraction is described by an additional conservation equation.

$$\frac{d}{dt} \int_V \alpha_i dV + \int_S \alpha_i (\mathbf{v} - \mathbf{v}_g) \cdot d\mathbf{a} = 0 \quad (6)$$

Where α_i represents the volume fraction. VOF is an interface capturing method, capable of tracking breaking waves and spray but lacking the sharp interface of interface-tracking methods. The critical issue with this method is the discretization of Eqn. 6. Typical low order schemes tend to smear the interface and introduce artificial mixing of the two fluids. The High Resolution Interface Capturing (HRIC) discretization scheme used in STAR-CCM+ is designed to mimic the convective transport of immiscible fluid components to improve the VOF interface tracking capabilities.

2.1.3.5 Algebraic Multigrid Solution Method

A linear equation system is obtained for the velocity and pressure terms at the CV centroid through the SIMPLE method which must be solved implicitly through iteration. This becomes an inner iterative process to the outer process of iteration via the SIMPLE algorithm. The equation to be solved, written in delta form for a general scalar φ is:

$$\frac{a_p}{\omega} \Delta \varphi_p + \sum_n a_n \Delta \varphi_n = b - a_p \varphi_p^k - \sum_n a_n \varphi_n^k \quad (7)$$

The coefficient a is obtained from the discretized terms of the cell of interest p and its neighboring cells n . The coefficient b represents the explicit contribution to the discretized equation evaluated at iteration k . The delta term is defined as $\Delta \varphi_p = \varphi_p^{k+1} - \varphi_p^k$. An under-relaxation factor is given by ω . The term on the right hand side is the residual and goes to zero when the exact solution to the discretized equation is reached. An algebraic multigrid method (AMG) is used to solve the linear system given by Eqn. 7 iteratively. Computation time is reduced by deriving a system of coarse-grid equations from arithmetic combinations of the fine-grid coefficients and performing some of the iterative work on the coarser level. This behaviour is due to the pace of information travel at one cell per iteration. In an elliptic problem, the information must travel across a great number of cells back and forth to reach convergence. If the cells are fine, then this iterative process is time consuming. The method is also more effective at removing low-frequency components of error.

2.1.3.6 Interpolation Methods

Variable values are calculated at CV centroids only. Reconstructing the face values and cell gradients in STAR-CCM+ involves three steps. First, reconstruction gradients are calculated using a hybrid Gauss/weighted LSQ method for both pressure and velocity. The reconstructed values are then limited so they do not exceed the maximum and minimum of the neighboring CV centroid values. Cell gradients are copied from the LSQ-based reconstruction gradients which are linear-exact.

2.1.3.7 Parallel Computing

RANS computations of a three-dimensional free surface flow are computationally intensive. It was therefore essential to use parallelization in computing. Simulations were generally run on 1 to 6 nodes of the Ithaca system at the Virginia Tech Advanced Research Computing Center. The system is an IBM iDataPlex with 8 processors, 2.26 GHz in speed and 24 GB of memory per node. Prescribed motion simulations in *Section 4* for example, with an overset mesh on the order of 10 million cells, required approximately 3500 s of computational time per time step (97 hours per second for $dt = 0.01$ s). By splitting the simulation on 48 processors this was effectively reduced to approximately two hours of wall time for every second of simulation time.

2.2 OVERVIEW OF POTENTIAL FLOW THEORY

Potential flow methods are used for comparison with the RANS results. The derivation of potential flow solutions is based on the assumptions of an inviscid, incompressible, homogeneous fluid and an irrotational velocity field applied to the complete Navier-Stokes equations. Given these conditions, the velocity field may be represented by a scalar velocity potential, Φ , which must satisfy the Laplace equation for conservation of mass in the fluid domain. This allows the problem to be reduced to the solution of a single linear partial differential equation instead of the coupled, nonlinear set of partial differential equations considered in a RANS approach. Here the full nonlinear formulation is given, and then linearization is discussed.

Following the notation of [4], a right handed coordinate system Oxyz translating in the negative x-direction with time-dependent velocity of the ship $U_0(t)$ is chosen. Setting the origin along the calm waterline with z pointing upward, the velocity potential in the time domain may be expressed as

$$\Phi(x, y, z; t) = U_0(t)x + \varphi(x, y, z; t) \quad (8)$$

Where $\varphi(x, y, z; t)$ is the perturbation potential. The Laplace equation is then

$$\nabla^2 \Phi = 0 \quad (9)$$

The difficulty comes in the application of boundary conditions to all surfaces which enclose the fluid domain: the body surface, the bottom, the free surface, and the surrounding fluid at infinity. The kinematic boundary condition is applied on the instantaneous position of the body wetted surface.

$$\frac{\partial \varphi}{\partial \mathbf{n}} = -U_0(t)n_1 + \mathbf{V} \cdot \mathbf{n} \quad (10)$$

Where \mathbf{V} is the body velocity relative to Oxyz and $\mathbf{n}(n_1, n_2, n_3)$ is the unit normal into the body with components n_1, n_2, n_3 in the x, y and z directions. A similar relation may be applied for a finite depth boundary. At infinite depth, $\nabla \varphi \rightarrow 0$ as $z \rightarrow -\infty$. On the instantaneous free surface dynamic and kinematic conditions must be satisfied. The amplitude of the free surface is unknown in the nonlinear case and must be determined as part of the solution. For a free surface elevation $z = \eta(x, y; t)$, the kinematic condition that the normal velocity of a particle on the free surface equals the normal velocity of the free surface itself is

$$\frac{\partial \eta}{\partial t} = \frac{\partial \varphi}{\partial z} - \nabla \varphi \cdot \nabla \eta - U_0(t) \frac{\partial \eta}{\partial x} \quad (11)$$

The dynamic condition that pressure on the free surface is everywhere equal to a known ambient pressure, P_a , can be given using Bernoulli's equation as

$$\frac{\partial \varphi}{\partial t} = -g\eta - \frac{1}{2} \nabla \varphi \cdot \nabla \varphi - U_0(t) \frac{\partial \varphi}{\partial x} - \frac{P_a}{\rho} \quad (12)$$

Where g is the gravity and ρ is the density of the fluid. In the time domain initial values of the free surface elevation and potential must be specified. For the frequency domain, time dependence is replaced by the real part of $e^{i\omega t}$. At infinity, waves due to the body disturbance must be outgoing in the frequency domain. For a problem with no incident waves in the time domain $\nabla \varphi \rightarrow 0$ as the distance from the body goes to infinity.

In order to linearize the nonlinear problem, various approximations of the involved physics are made. The common assumptions are the linearization of the free surface boundary conditions, and satisfaction of the body boundary condition at its mean position rather than on the instantaneous wetted surface. In the linear free surface boundary condition, higher order terms are neglected in Equations 10 and 11, and the condition is imposed on the undisturbed free surface plane. Methods which use this free surface condition and evaluate the body boundary condition on the mean wetted surface are typically categorized as linear, while nonlinear codes consider the 2nd order terms in the free surface boundary condition and satisfy the hull boundary condition on its changing wetted surface. In addition, blended methods have emerged which take advantage of the nonlinearities that are easily computed. Typically, the hydrostatic and Froude-Krylov components of the potential are calculated using the body-exact and nonlinear free surface boundary conditions, while a linear approximation of the more difficult to compute radiation and diffraction components is used.

3 HYDRODYNAMIC COEFFICIENTS of 2D RECTANGULAR CYLINDER

The estimation of a ship's response in waves relies on the accurate calculation of hydrodynamic coefficients and exciting forces. Using linear ship motions theory, the problem is separated into a radiation problem in which added mass and damping coefficients are determined, and an excitation problem which seeks Froude-Krylov and diffraction forces. To simplify the calculation of these hydrodynamic coefficients, a strip theory method is often used in which the frequency dependent added mass and damping terms are found for a number of two-dimensional transverse sections and integrated along the ship length to obtain the three-dimensional coefficients. Most estimates of two-dimensional coefficients are found using linear potential flow approaches including distributed sources and conformal mapping techniques such as Lewis forms. However, viscous and rotational effects have been shown to be important in certain cases. Previous studies have demonstrated good agreement between added mass and damping coefficients calculated using RANS methods and experimental results for simple two-dimensional sections (e.g. [20],[21]).

In this section, the STAR-CCM+ RANS solver is employed in calculating the hydrodynamic coefficients of a two-dimensional rectangular cylinder. For validation of the method, the added mass of the rectangle in an unbounded fluid is determined and compared to the analytical potential flow result. A calm free surface is then added, and hydrodynamic coefficients are determined for harmonic oscillations of several amplitudes with the cylinder situated at beam-to-draft ratios, $B/T = 2, 4$ and 8 . Results are compared with the potential flow solutions and experimental work of Vugts [22] over a series of frequencies.

3.1 HYDRODYNAMIC COEFFICIENT CALCULATION

Hydrodynamic coefficients are obtained by oscillating the body according to some harmonic function and measuring the total force response in the direction of motion. As an example, a harmonic function of the form $z_3 = z_a \sin(\omega t)$ is considered in heave. According to linear theory, the total radiation force result of a body in sinusoidal heave motion in otherwise calm water is

$$F_{R_3} = -[a_{33}(\omega)\ddot{z}_3 + b_{33}(\omega)\dot{z}_3 + c_{33}z_3] \quad (13)$$

Where a and b are the added mass and damping respectively as functions of frequency, and c is the hydrostatic restoring term. The restoring force, $F_{restoring_3} = -c_{33}z_3$, is estimated according to the body cross-sectional geometry and position relative to the mean waterline over time. This is alternately defined by

$$F_{restoring_3} = \nabla d \rho g \quad (14)$$

Where ∇ is the instantaneously submerged cross-sectional area with respect to the mean waterline, d is the depth of the approximately two-dimensional body, ρ is the freshwater density, and g is the gravitational acceleration. Removing this component of force leaves the purely hydrodynamic force, given by

$$F_{H_3} = -a_{33}(\omega)\ddot{z}_3 - b_{33}(\omega)\dot{z}_3 \quad (15)$$

Since the added mass term is in phase with the heave motion, and damping is in quadrature, the two terms may be separated by a Fourier phase analysis. Instantaneous values of each coefficient are obtained from the force time history by analyzing discrete windows equal to a single period of oscillation [23]. Thus, the coefficients in heave are

$$a_{33} = \frac{1}{\pi Z_a \omega} \int_{t-T/2}^{t+T/2} F_{H_3} \sin(\omega t) dt \quad (16)$$

$$b_{33} = \frac{1}{\pi Z_a} \int_{t-T/2}^{t+T/2} F_{H_3} \cos(\omega t) dt \quad (17)$$

A similar formulation can be given for the coefficients in sway (a_{22}, b_{22}). However, in sway and in the case of motion in an unbounded fluid there is no restoring force. Coupled sway-roll coefficients are determined by monitoring roll moment about the center of gravity G induced by sway motion. In the experimental results, coefficients are defined for motion about a point O which is centered at the intersection of the centerline and waterline. The total hydrodynamic moment in 1-DoF sway is then given as

$$F_{H_4} = -(a_{24}(\omega) + OG \cdot a_{22}(\omega))\ddot{x}_2 - (b_{24}(\omega) + OG \cdot b_{22}(\omega))\dot{x}_2 \quad (18)$$

Where OG is the distance between O and G , which is zero for $B/T = 2$. The coupled sway-roll coefficients, a_{24} and b_{24} , are calculated by substituting into Eqn. 16 and 17 and subtracting the coordinate system change component using the pre-computed a_{22} and b_{22} values. As a result, the coupling coefficients are equal to the small difference between two large quantities such that accuracy in the analysis is low. Coefficients are non-dimensionalized as

$$\begin{aligned} a_{jj}^* &= \frac{a_{jj}}{\rho A_x} & b_{jj}^* &= \frac{b_{jj}}{\rho A_x} \sqrt{\frac{B}{2g}} \\ a_{24}^* &= \frac{a_{24}}{\rho B A_x} & b_{24}^* &= \frac{b_{24}}{\rho A_x} \sqrt{\frac{B}{2g}} \end{aligned} \quad (19)$$

Where B is the beam of the cylinder and A_x is the mean submerged area. Time history results from STAR-CCM+ are not rigorously analyzed for settling of transients, but a visual examination is used to determine the starting point for data analysis. At least 3 periods of oscillation are allowed to pass before the analysis in all cases. Hydrodynamic coefficients are obtained from subsequent periods and averaged together.

3.2 OSCILLATION IN AN UNBOUNDED FLUID

An analytical solution is available for the added mass of a circular cylinder in an unbounded fluid using potential flow assumptions. Taking advantage of the conformal transformation of a circle to a rectangle of equal dimensions the added mass in any translation direction is $4.754 \rho a^2$ where the height and beam dimensions are equal to $2a$ [24]. For submerged bodies without proximity to a free surface, there is added mass but no damping in potential flow. A rectangular geometry with dimensions matching those used in experiments; height and beam of 0.4 m, and sharp corners was considered. Although a finite volume formulation is employed, STAR-CCM+ allows the extraction of a two-dimensional mesh from a one cell thick three-dimensional mesh in cases which do not involve a VOF model of the free surface. Essentially the mesh remains one unit cell thick, but the two-dimensionality is acknowledged by STAR-CCM+ which saves computational time and some complexity in the definition of boundary conditions. The mesh is unstructured, with local refinement about the body and a body-fitted prism layer. The near-wall prism layer thickness is 10^{-4} such that a $y^+ \leq 10$ is maintained. The domain, shown in Figure 1, is 4.4 x 4.4 m and totals 62,253 cells. Local mesh refinement around the sharp corners and the prism layer mesh are shown in Figure 2. The mesh is rigid and body-fixed such that the body oscillation involves movement of grid points.

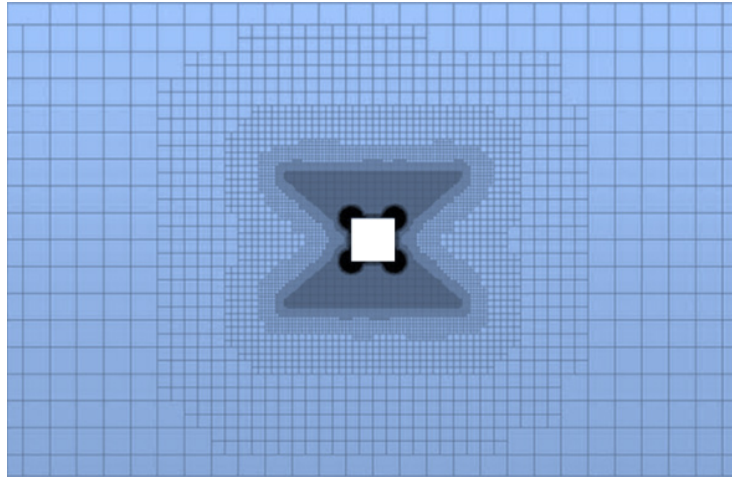


Figure 1. Unbounded fluid case domain mesh



Figure 2. Corner and boundary layer mesh refinement

To best match the analytical potential flow solution in which there are no frequency or amplitude effects, the prescribed oscillation in heave was of the lowest amplitude, $z_a = 0.01$ m, and frequency, $\omega = 1.5$ rad/s considered in [22]. Time step size, dt , was governed by the CFL number which relates cell dimension Δ to flow speed U by $CFL = \frac{Udt}{\Delta}$. This is the ratio between time step, and the time required for a disturbance to convect across a cell. For numerical stability, local CFL numbers should in general be kept less than unity. A time step of 0.005 s was used to satisfy this criterion for most cells through time. No-slip and non-penetration boundary conditions apply on the surface of the cylinder. Bottom, top and side boundaries are pressure outlets which maintain the constant far field pressure of an unbounded fluid. Oscillation in the vertical direction permitted use of a symmetry plane through the cylinder center to mirror the domain on one side and halve the total number of cells. As expected at the low amplitude and frequency chosen to most closely resemble the potential flow case, damping in the RANS result is small. The added mass exhibited little variation between periods that were analyzed. The averaged result, $a_{33} = 189.64$ kg/m, shows excellent agreement with the analytical solution, $a_{33} = 189.70$ kg.

3.3 OSCILLATION IN HEAVE AND SWAY ABOUT A CALM FREE SURFACE

A calm free surface is added, and hydrodynamic coefficients are determined for the rectangular cylinder oscillating in heave and sway at several beam-to-draft ratios and frequencies. To create the mesh, rounded bilges were added to the previous geometry using a fillet of radius 2.5 mm. The computational domain was enlarged to match approximately the physical proportions of the experimental basin with width 400 m. Within 25 m on either side of the cylinder the mesh is similar to that shown in Figure 1 and Figure 2. Extending from 25 m off of the centerline to the edge of the domain are extruded cells of growing aspect ratio. These cells widen the domain and create a numerical beach for limitation of wave reflections without significantly increasing the total number of cells. Local refinement around the bilges and around the body below the waterline is maintained and refinement of the free surface about the mean waterline is added. Symmetry about the centerline is applicable in heave, but not in sway and total cells number 134,560 and 268,949 respectively. The mesh without symmetry plane is shown in Figure 3. A periodic boundary interface is used with a one cell thick mesh to mimic a two-dimensional flow. The interface maps flux through one boundary to the second boundary, setting up a cyclic repeat of information and approximating an infinite geometry. All other boundaries match those described in the previous section. Turbulence is modeled using a $k-\varepsilon$ approach.

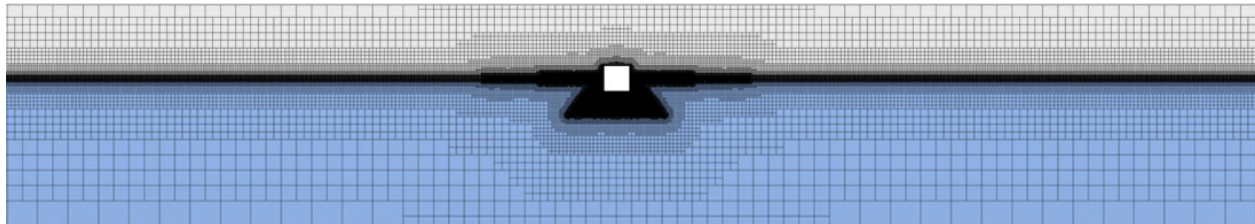


Figure 3. Free surface case mesh

3.3.1 Influence of Near-Wall Grid Spacing and Time Step

A systematic study of the effect of wall-normal grid spacing in the boundary layer is presented in Table 1 for $B/T = 4$ with the cylinder in heave. To create each mesh, the distance of the first grid line from the wall was changed while tangential cell spacing remained constant. The solution with near-wall thickness $y_0 = 0.0001$ m is shown to be reasonably well converged. This resolution was used for the rest of the study. It results in maximum y^+ values of 10 or less and average y^+ values of approximately 1 or less for the near-wall cell in the boundary layer.

Table 1. Influence of near-wall grid spacing on hydrodynamic coefficients, rectangular cylinder in heave, $B/T = 4$

ω^*	z_a (m)	$y\theta$ (m)	y^+ max	y^+ avg	a_{33}^*	b_{33}^*
1.71	0.01	0.001	30.76	4.15	1.89	0.12
		0.0005	17.27	2.31	1.89	0.12
		0.0001	5.52	0.54	1.90	0.12
	0.03	0.0005	60.06	5.81	1.92	0.29
		0.0001	11.95	1.15	1.95	0.41
		0.00001	1.02	0.12	1.95	0.40
1	0.01	0.001	30.76	4.15	1.51	0.60
		0.0005	17.27	2.31	1.52	0.56
		0.0001	5.52	0.54	1.55	0.53
	0.03	0.0005	60.06	5.81	1.59	0.72
		0.0001	11.95	1.15	1.65	0.75
		0.00001	1.02	0.12	1.65	0.75
0.4	0.01	0.001	6.79	1.25	2.21	1.10
		0.0005	4.67	0.71	2.20	1.10
		0.0001	1.61	0.15	2.15	1.11
	0.03	0.0005	9.41	1.28	2.17	1.21
		0.0001	3	0.28	1.88	1.28

A time step convergence study was conducted for cases with the highest frequency considered and two amplitudes of oscillation. Time steps were systematically refined by a ratio of 2, with the smallest time step being 0.003 s for $z_a = 0.01$ m and 0.001 s for $z_a = 0.03$ m. Added mass and damping coefficients are given for simulations using each time step in Table 2. The convergence appears oscillatory; however, the relative difference between the medium and small time step solutions was seen as sufficiently small. The smallest time step examined was thus used for all other simulations. CFL numbers were seen to vary between 0.8 and 1.2 through most cells at the highest frequencies of oscillation, and were generally less than 0.25 at the lowest frequencies.

Table 2. Influence of time step on hydrodynamic coefficients, rectangular cylinder in heave, $B/T = 4$

ω^*	z_a (m)	Time Step	a_{33}^*	b_{33}^*
1.71	0.01	0.012	1.85	0.05
		0.006	1.81	0.15
		0.003	1.90	0.12
1.71	0.03	0.004	1.96	0.37
		0.002	1.92	0.45
		0.001	1.95	0.41

3.3.2 Oscillation in Heave Results

A rectangular cylinder harmonically heaving at a free surface with beam-to-draft ratios $B/T = 2, 4$ and 8 was examined. Non-dimensional circular frequencies $\omega^* = \omega\sqrt{B/2g}$ between 0.40 and 1.71 were used with amplitudes $z_a = 0.01$ and 0.03 m. Results are compared to the experimental data and linear potential flow calculations of Vugts [22]. Figure 4 gives added mass and damping coefficients as a function of the non-dimensional frequency, with potential flow solutions according to the best section fit mapping shown by solid lines and those according to the Lewis form by dashed lines. In general, good agreement is shown between RANS, potential flow and experimental results. At $\omega^* = 0.4$ the damping tends to be over-predicted by RANS. This is due to bottom effects in the experimental results which were not considered in this RANS solution, but are examined in *Section 3.4.2*. In cases of high amplitudes and frequencies of oscillation the total hydrodynamic force becomes nonlinear with significant deviation from sinusoidal form. The Fourier analysis to determine constant added mass and damping coefficients breaks down in this circumstance. Figure 5 shows a time history of the hydrodynamic force over one period of oscillation, and the approximation of added mass and damping forces using constant coefficients for the $B/T = 4$, $\omega^* = 1.71$, $z_a = 0.03$ m case. Nonlinearity of the hydrodynamic force may be attributed to several effects. The linear approximation of hydrostatic force is a poor assumption in the case of a nonlinear free surface and hydrostatic elements could remain in the total hydrodynamic force as a result. A contribution to added mass arises from variation in wetted surface area such that nonlinearities in the free surface can also cause time variation in the added mass coefficient. Also, viscous eddies propagating along the body invoke an unsteady component which may manifest itself in time-dependence of the hydrodynamic coefficients. The viscous effects are clearly visible in Figure 6, in which vorticity contours and velocity vectors are shown for two different amplitudes of oscillation at the same B/T and ω^* as in Figure 5. Nonlinearity was most substantial at $\omega^* \geq 1.25$ for $B/T = 8$ and $z_a = 0.03$ m. Results for these cases are not shown since analysis using constant coefficients was not viable. It is surmised that eddy formation and diffusion in particular may be the root cause for deviation of the RANS and experimental damping coefficients from the potential flow solutions at high frequencies for cases of high amplitude oscillation. Separation at the sharp bilges corresponds with an energy loss due to the formation of eddies. Because the dissipation of energy is represented by damping coefficients it is reasonable that their increase with amplitude and frequency is related to the increase in eddy strength. Since the viscous flow field undergoes significant modification as oscillation

amplitude and frequency are increased, it is also plausible that the added mass is becoming time dependent (through its flow field dependence) and the increase in the damping is a result of the Fourier analysis attempting to produce the best match to the nonlinear hydrodynamic force.

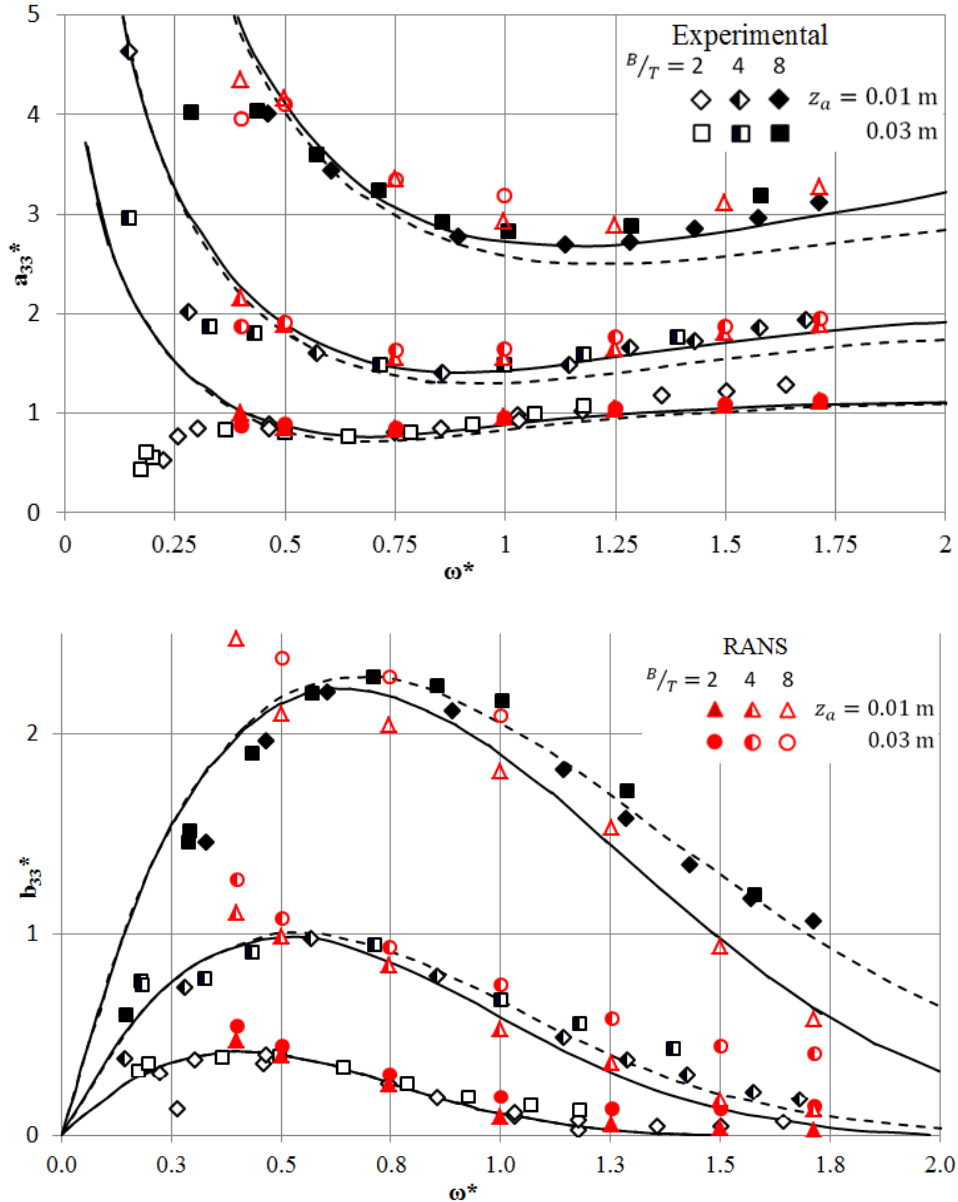


Figure 4. Non-dimensional added mass (top) and damping (bottom) coefficients in heave as function of non-dimensional frequency; experimental values in black and white, RANS results in red and potential flow theory solutions using conformal mapping given by solid (best section fit mapping) and dashed (Lewis form) lines

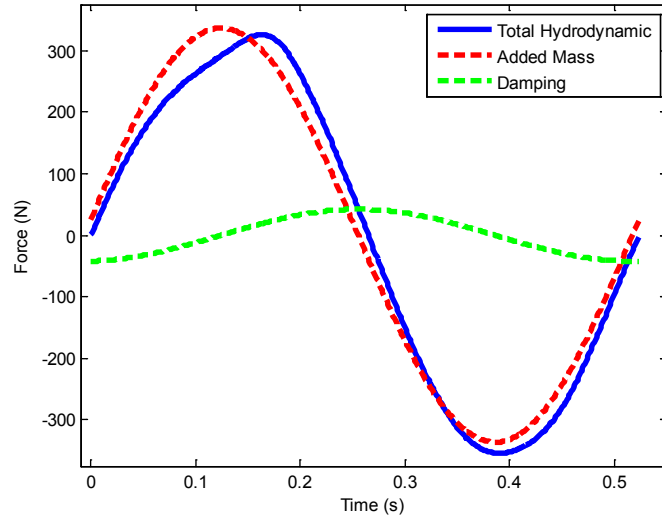


Figure 5. Hydrodynamic components of force in heave: $B/T = 4$, $\omega^* = 1.71$, $z_a = 0.03$ m

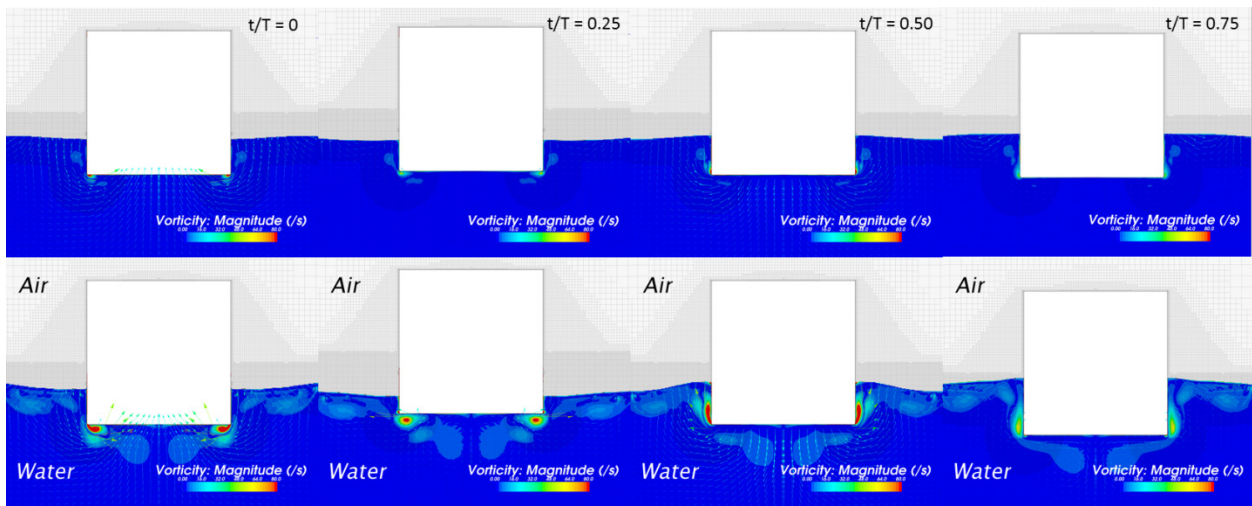


Figure 6. Vorticity contours and velocity vectors in heave at $t/T = 0, 0.25, 0.50, 0.75$: $B/T = 4$, $\omega^* = 1.71$, $z_a = 0.01$ m (top) and $z_a = 0.03$ m (bottom)

3.3.3 Oscillation in Sway Results

The case of a rectangular cylinder harmonically swaying at a free surface was studied at the same beam-to-draft ratios and frequencies examined in heave. Amplitudes of oscillation $z_a = 0.01$ m were simulated for all beam-to-draft ratios, and $z_a = 0.03$ m was tested at $B/T = 4$ in order to assess any influence of amplitude. The added mass and damping coefficients in sway are given in Figure 7. Good agreement is shown between RANS and experimental results, particularly for added mass. Sway damping is somewhat over-predicted at $B/T = 8$, and under-predicted at $B/T = 2$. In the $B/T = 2$ case the RANS solution aligns approximately with the linear potential flow solution, while experimental results show damping forces which are greater than theoretical predictions. Overall, the RANS and potential flow solutions appear to match

experimental results equally well. Sway-roll coupling coefficients are given in Figure 8 through Figure 10. The coupling coefficients are small and unreliable as realized during the experimental study and corroborated by the RANS results. Nevertheless, the RANS results generally match the experimental values more closely than potential flow. In examining the influence of amplitude for $B/T = 4$, no regular trend is apparent. Further, as Figure 11 shows, the scale of eddies generated at $z_a = 0.03$ m is much smaller in sway than in heave and congruently no significant nonlinearity appears in the hydrodynamic force.

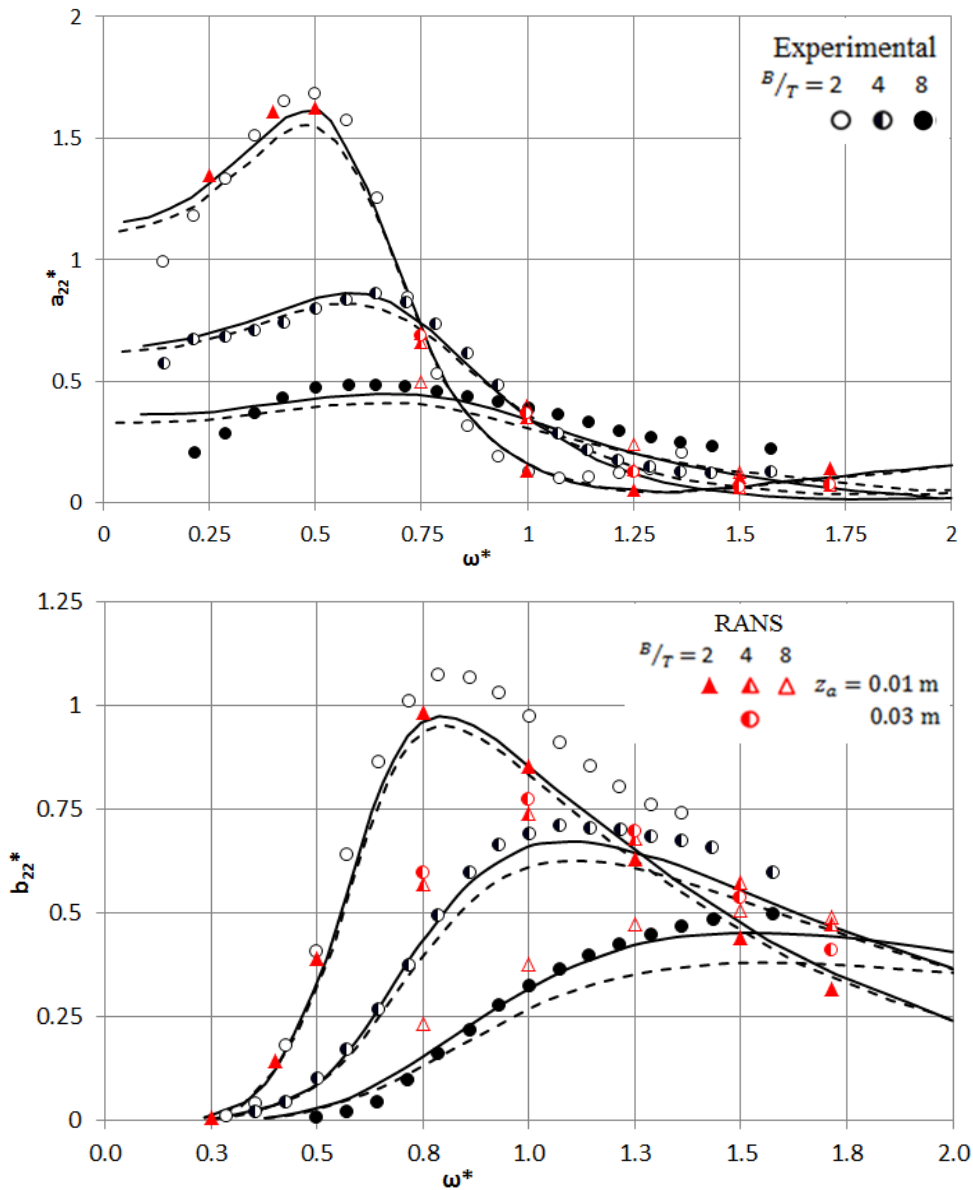


Figure 7. Non-dimensional added mass (top) and damping (bottom) coefficients in sway as function of non-dimensional frequency; experimental values in black and white, RANS results in red and white, and potential flow theory using conformal mapping given by solid (best section fit) and dashed (Lewis form) lines

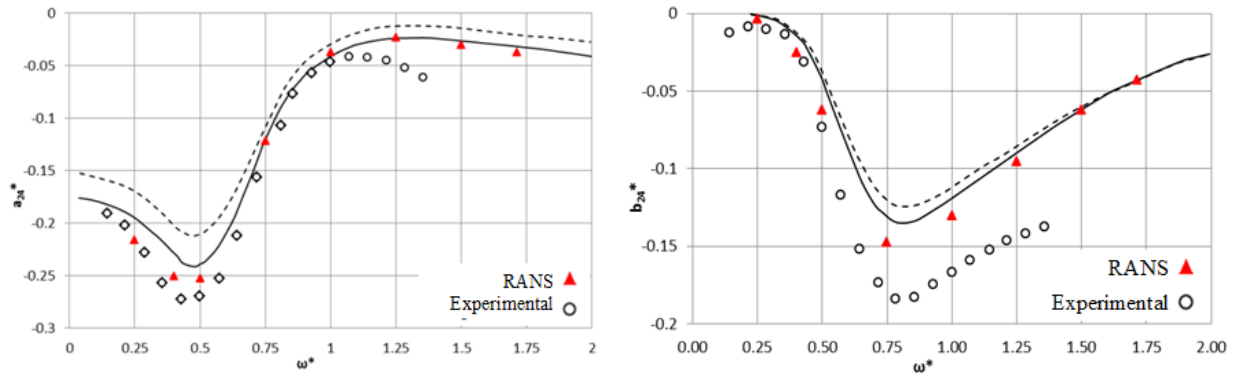


Figure 8. $B/T = 2$ added mass (left) and damping (right) sway-roll coupling coefficients; conformal mapping solutions given by solid (best section fit) and dashed (Lewis form) lines

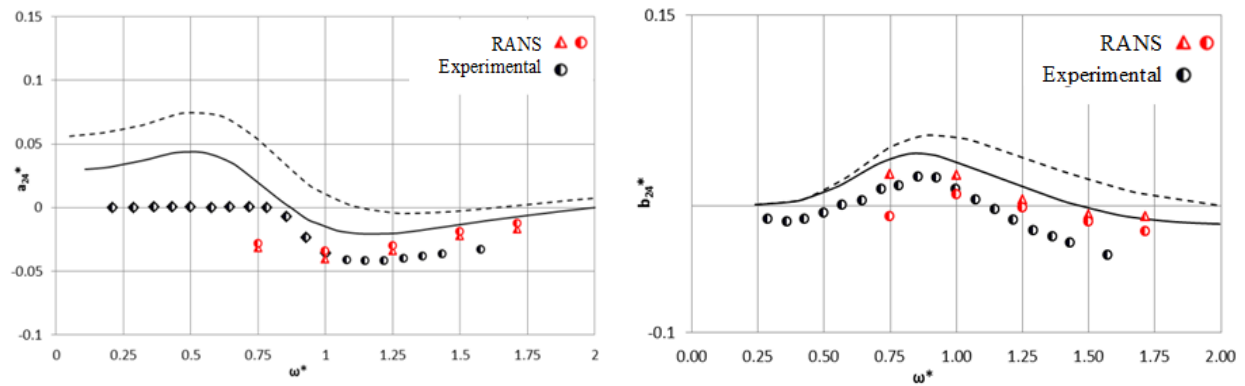


Figure 9. $B/T = 4$ added mass (left) and damping (right) sway-roll coupling coefficients; conformal mapping solutions given by solid (best section fit) and dashed (Lewis form) lines

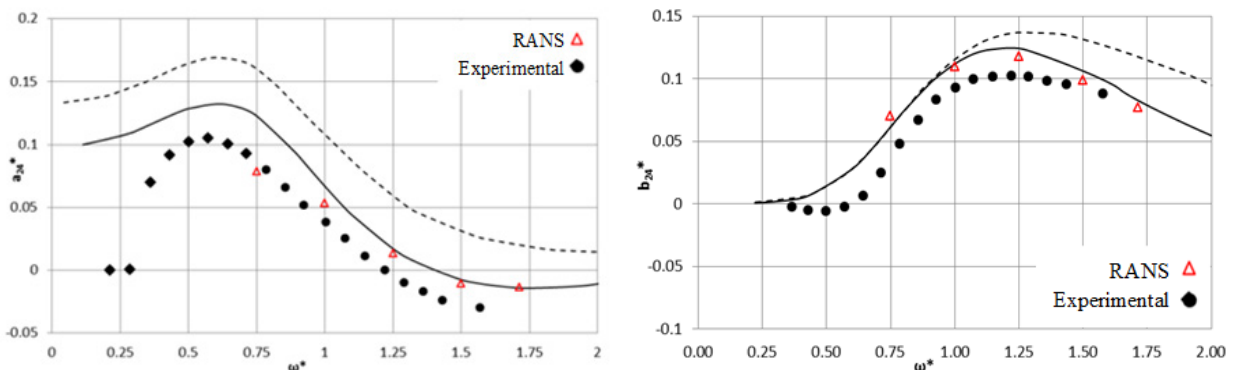


Figure 10. $B/T = 8$ added mass (left) and damping (right) sway-roll coupling coefficients; conformal mapping solutions given by solid (best section fit) and dashed (Lewis form) lines

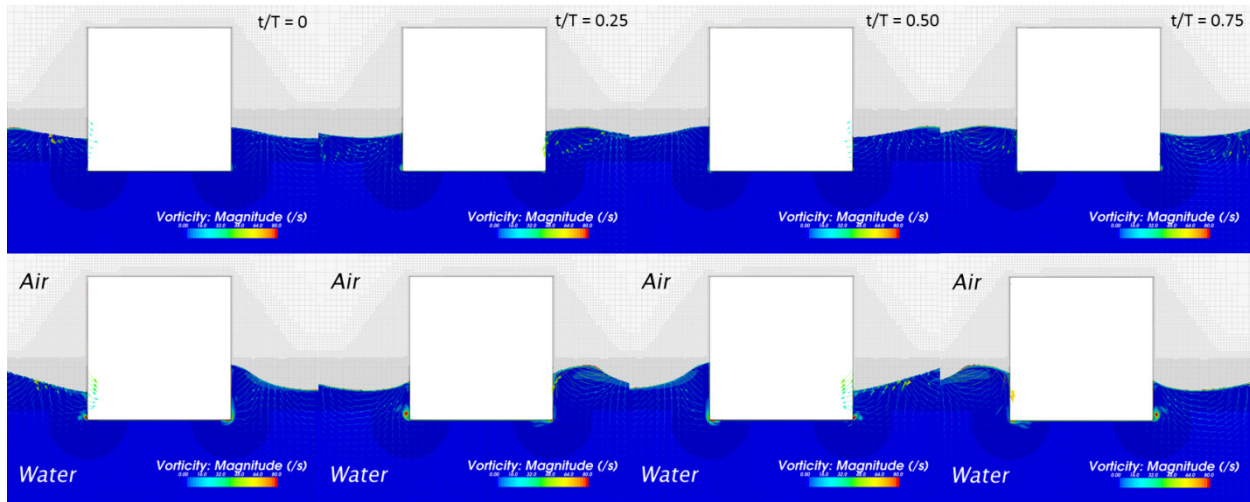


Figure 11. Vorticity contours and velocity vectors in sway at $t/T = 0, 0.25, 0.50, 0.75$: $B/T = 4$, $\omega^* = 1.71$, $z_a = 0.01$ m (top) and $z_a = 0.03$ m (bottom)

3.4 ADDITIONAL PARAMETER EVALUATION

3.4.1 Turbulence Model Effects

To show the influence of turbulence modeling, added mass and damping coefficients determined using the $k-\varepsilon$ and $k-\omega$ models described in *Section 2.1.3.2* are given in Table 3 for $B/T = 4$ in heave at select frequencies. At low frequency, turbulence has little effect on the hydrodynamic coefficients and the modeling approach is inconsequential. At higher frequencies, the $k-\omega$ model damping coefficients are larger than those produced using the $k-\varepsilon$ model although added mass values remain consistent. While the damping coefficients produced by the $k-\varepsilon$ model match more closely with experimental values, inferences about the accuracy of each turbulence model are impractical since there is no experimental force time history available. The comparison for validation is limited to linear approximations of added mass and damping, which are a poor representation of the actual force time history at high frequency. Nevertheless, differences between the two turbulence models are evident in the hydrodynamic coefficients, force time histories and flow features. For instance, the discrepancies shown between the time histories of hydrodynamic force in Figure 12 appear to be due to the tendency for eddies in simulations using a $k-\omega$ model to be larger and separate more easily from the body than those produced by the $k-\varepsilon$ model. Figure 13 shows snapshots over time of the vorticity contours and velocity vectors for the $B/T = 4$, $\omega^* = 1.71$, $z_a = 0.03$ m case using the $k-\omega$ model. Comparing this with Figure 6 illustrates the flow feature differences between solutions using each model.

Table 3. Turbulence model comparison, hydrodynamic coefficients for heave motion, $B/T = 4$

z_a (m)	ω^*	y+ max	y+ avg	$k-\epsilon$		$k-\omega$	
				a_{33}^*	b_{33}^*	a_{33}^*	b_{33}^*
0.01	0.4	1.58	0.14	2.15	1.11	2.9	1.10
	1	3.31	0.34	1.55	0.53	1.52	0.61
	1.71	5.52	0.54	1.90	0.12	1.91	0.19
0.03	0.4	2.65	0.28	1.88	1.28	1.92	1.29
	1	5.8	0.66	1.65	0.75	1.63	0.84
	1.71	11.95	1.15	1.95	0.41	1.93	0.60

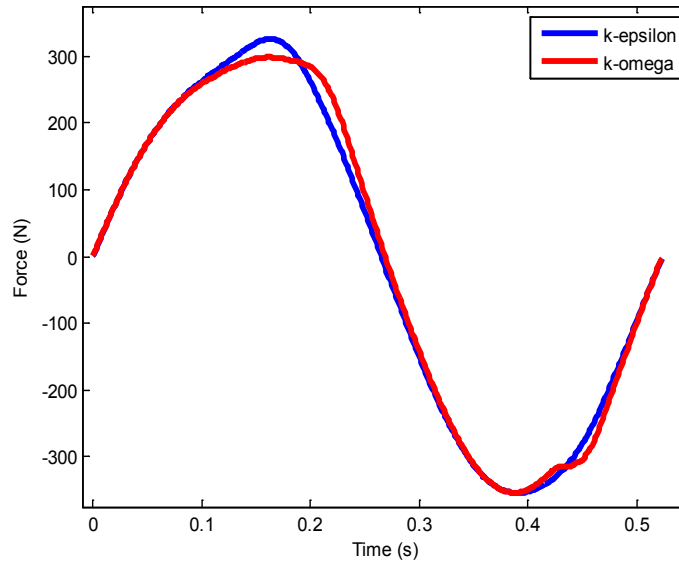


Figure 12. Total hydrodynamic force in heave: $B/T = 4$, $\omega^* = 1.71$, $z_a = 0.03$ m

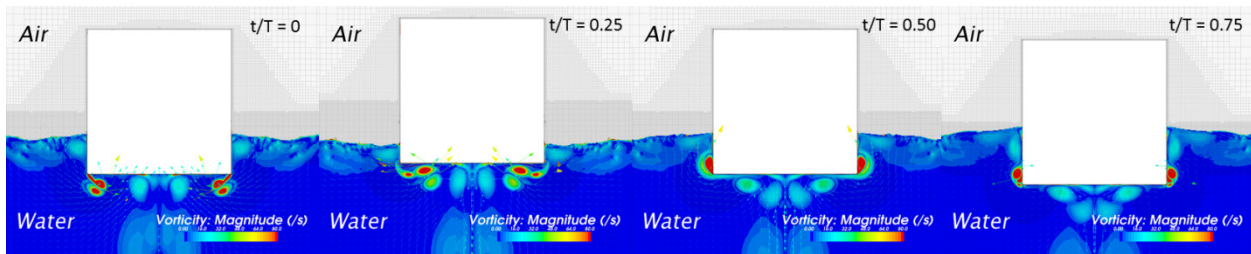


Figure 13. Vorticity contours and velocity vectors in heave at $t/T = 0, 0.25, 0.50, 0.75$: $B/T = 4$, $\omega^* = 1.71$, $z_a = 0.01$ m (top) and $z_a = 0.03$ m (bottom) using $k-\omega$ turbulence model

3.4.2 Bottom Effects

A deep-water wave approximation is practical as long as the actual water depth is greater than $\frac{1}{2}\lambda$, where λ is the wavelength. The simulation results given in *Sections 3.3.2 and 3.3.3* are for water depths of 2 m, 1.9 m and 1.85 m for $B/T = 2, 4$ and 8 respectively. These are within the stated water depth range, 1.8 m to 2.25 m, of the experimental study. However, a pressure outlet boundary condition is used in the simulations to accommodate fixed mesh motion such that the effective water depth is infinite. This approximation is sufficient for higher frequencies of oscillation in which the radiated wave lengths satisfy the deep-water criteria. At frequencies of $\omega^* \leq 0.75$, bottom effects become relevant due to the long wavelength of radiated waves. To account for bottom effects, the bottom boundary must have no-slip and non-penetration conditions. Because rigid mesh motion with a bottom wall boundary would vary the water depth with time, a new simulation was created using an overset mesh to investigate these effects. Use of an overset mesh permits motion of the body, while the background mesh and domain boundaries remain static. The overset mesh is shown in red in Figure 14 displaced to a vertical position of 0.02 m and the background mesh is shown in blue. Details of the overset mesh technique employed by STAR-CCM+ are given in *Section 4.3.1*. Figure 15 compares experimental added mass and damping coefficients with RANS results for several water depths as a function of frequency for $B/T = 4$. RANS results are given for a depth of 1.9 m between $\omega^* = 0.25$ and 0.75, and for depths of 1.8 and 2.2 m at $\omega^* = 0.40$. The inclusion of bottom effects affords a better estimate of the hydrodynamic coefficients relative to experimental values at low frequencies, particularly for damping. However, added mass and damping coefficients appear to be underpredicted relative to the experimental values for low amplitude, $z_a = 0.01$ m, cases. Comparison of results at $\omega^* = 0.40$ for three finite depths demonstrates the magnitude of change in the coefficients resulting from small changes in water depth. Since only a range of depths used in the experimental study are known, instead of exact values for particular cases, the corresponding RANS estimation may lie anywhere within this range.

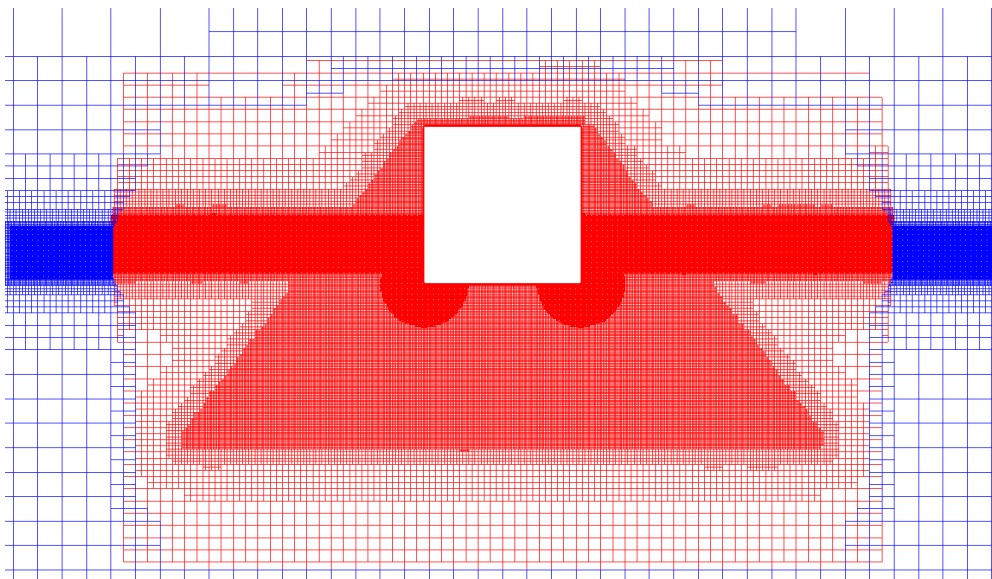


Figure 14. Overset mesh in red, background mesh in blue, $B/T = 4$

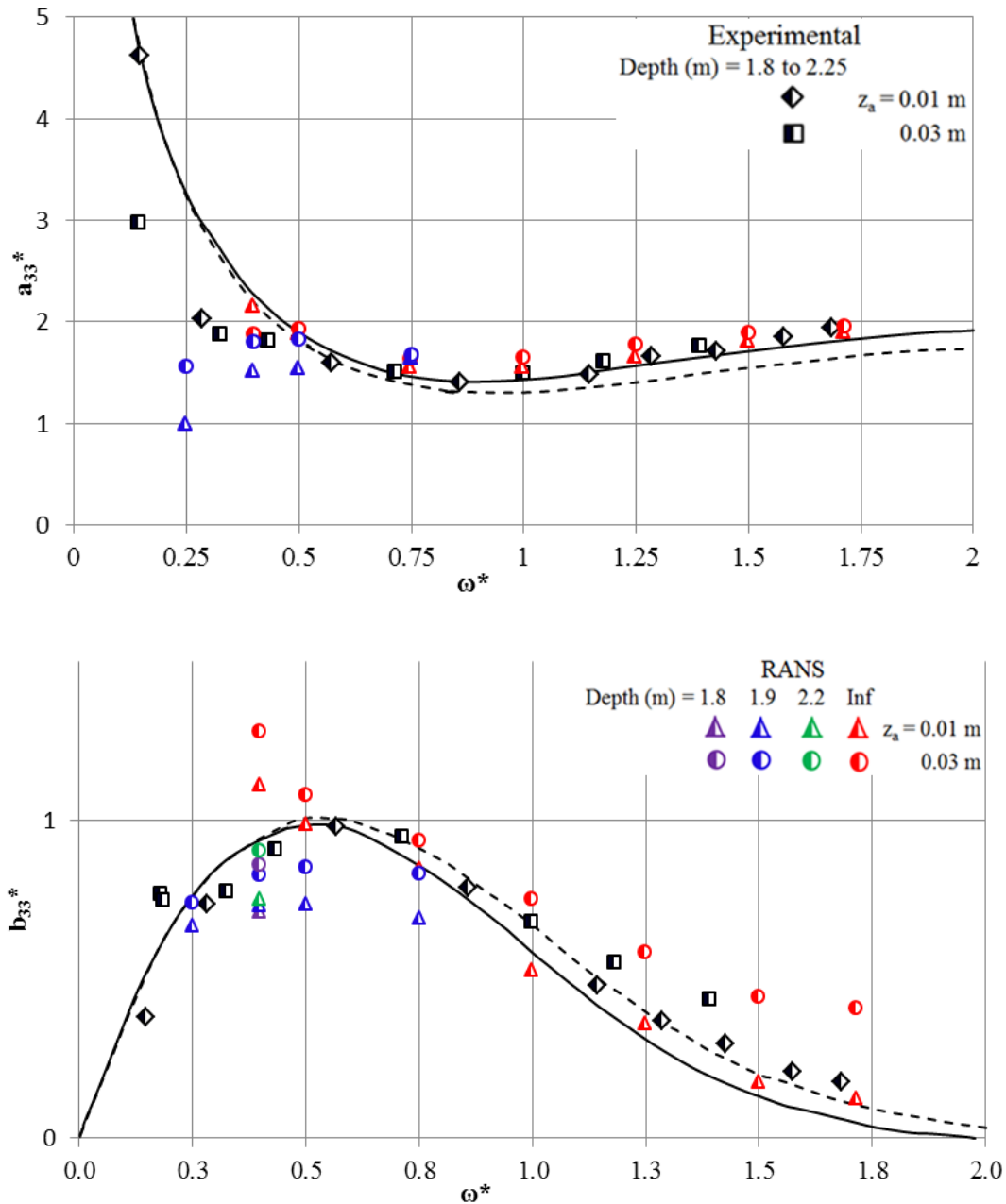


Figure 15. Non-dimensional added mass (top) and damping (bottom) coefficients in heave as function of non-dimensional frequency; experimental values in black and white, RANS results in color and potential flow theory using conformal mapping given by solid (best section fit) and dashed (Lewis form) lines

4 ONR TUMBLEHOME IN PRESCRIBED MOTIONS AND WAVES

Calculations of force and moment on the ONR Tumblehome (ONRTH) hullform during prescribed 1-DoF heave and pitch oscillations and in a 0-DoF, fixed in waves condition, are compared between STAR-CCM+ as a RANS solver and a set of potential flow codes with varying degrees of simplification. The latter results are part of a computational Force Study summarized by Belknap and Telste [16] and fully documented in an additional report [2]. The study's aim was to compare existing potential flow models with varying degrees of simplification in their ability to calculate forces and moments on the ONRTH. It consisted of a series of prescribed motions and waves representing conditions in which linear assumptions may be sufficient to model the physical response and those in which nonlinearity was expected to be significant. The specific tasks completed were 1-DoF prescribed oscillation in calm water (radiation problem), 0-DoF forward speed in waves (diffraction problem), and 2-DoF prescribed motion in waves (nominal wave contouring problem). Codes involved in the study are given in Table 4 along with an abbreviated identifier.

The potential flow methods considered are categorized as linear, blended or nonlinear, and may be three-dimensional or use a two-dimensional strip-theory approach. In general, the potential flow codes can be classified by their treatment of hydrostatic forces and moment [2]. Linear codes (A1, L1) use waterplane quantities in calculating hydrostatics while all others employ pressure integrals. Blended and nonlinear theories are separated by their treatment of radiation and diffraction forces which are typically linear and non-linear respectively. The handling of hydrostatic and Froude-Krylov forces is nonlinear for both blended and fully nonlinear methods. NFA is an Euler code based on a VOF technique. Of the codes examined in the Force Study, NFA most closely matches the STAR-CCM+ RANS solver in formulation with the key exception being its neglect of viscous effects. Due to limitations of this code at the time of the study, and the significant computational resources required for it to run, results were not given for all cases [13]. A summary of the characteristics of each code included in the study is given by Telste and Belknap [2]. In the Force Study, results provided from each code were separated into contributions from hydrostatic, radiation, diffraction and Froude-Krylov force. However, for this study only the total forces and moments are considered since the RANS computational technique does not lend itself to identifying these individual components.

Table 4. List of Force Study Codes

Abbr.	Program Name	Development Location	Theory Type
A1	AEGIR-1	Applied Physical Sciences and Flight Safety Technology	3-D, Linear
A2	AEGIR-2	Applied Physical Sciences and Flight Safety Technology	3-D, Blended
FD	FREDYN	MARIN	2-D, Blended
L1	LAMP-1	SAIC-Annapolis	3-D, Linear
L3	LAMP-3	SAIC-Annapolis	3-D, Blended
L4	LAMP-4	SAIC-Annapolis	3-D, Nonlinear
NF	NFA	SAIC-La Jolla	Euler
NS	NSHIPMO	University of Michigan	2-D, Nonlinear

4.1 GEOMETRY

The hull geometry considered is the tumblehome variant of the ONR Topsides series known as ONRTH with length 154 m and draft 5.5 m. DTMB Model #5613-1 is the corresponding model, described in detail by Bishop et al. [25]. The ship is representative of a modern surface combatant with a hullform similar in size and characteristics to the DDG51 with 10-degree sloping tumblehome sides. Sharp changes in the waterline geometry with changes in draft represent a source of nonlinearity in the response during large amplitude motions. Numerical simulations using STAR-CCM+ and in the Force Study were performed for the ship at full scale without deckhouse or appendages. The origin of the ship-fixed coordinate system is at the center of gravity with x-axis positive forward, y-axis positive to port and z-axis pointing upward. Table 5 summarizes the principal particulars of the ONRTH. A body plan of the hullform is shown in Figure 16 and an isometric view is given in Figure 17.

Table 5. ONRTH Particulars

Length, L (m)	154
Beam, B (m)	18.8
Draft, T (m)	5.5
Volume (m ³)	8543
Weight (kN)	8.59×10^4
VCG (m ABL)	5.5
LCG (m aft of FP)	79.6

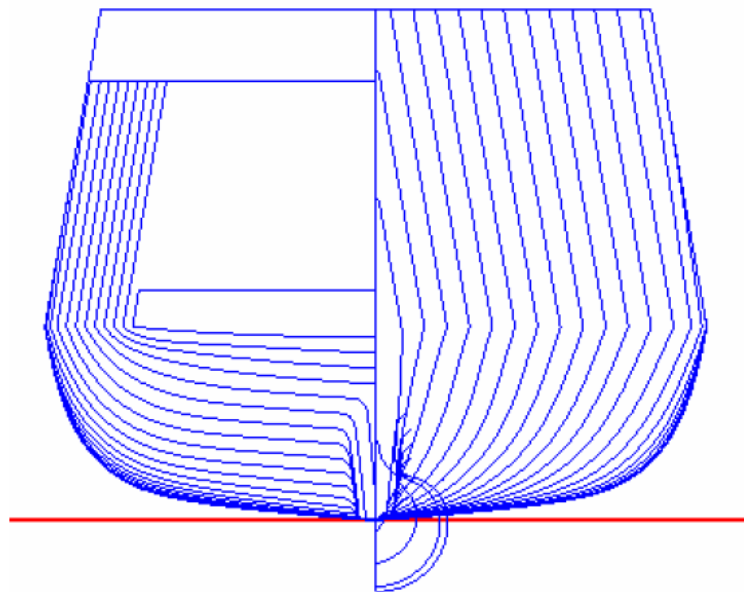


Figure 16. ONRTH body plan

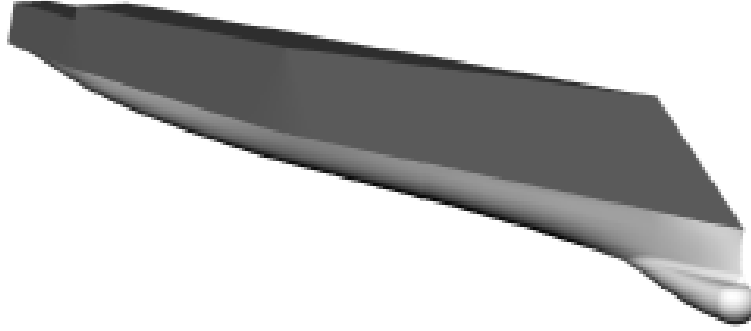


Figure 17. ONRTH isometric view

4.2 PRESCRIBED 1 DOF HEAVE AND PITCH OSCILLATIONS

Prescribed 1-DoF heave and pitch motions are examined at two frequencies and two amplitudes. Cases are considered at both zero speed and forward speed ($F_n=0.3$). Low frequency and amplitude represent highly linear cases which confirm the STAR-CCM+ solution. High frequency and amplitude cases exhibit significant nonlinearity. Table 6 gives the selected cases with heave amplitude represented as a percentage of the design draft and pitch taken about the LCG.

Table 6. Prescribed Oscillation Cases

Heave $Z = z_a \sin(\omega t)$			Pitch $\theta = \theta_a \sin(\omega t)$		
Amplitude	Frequency		Amplitude	Frequency	
z_a (% of T)	ω (rad/s)		θ_a ($^\circ$)	ω (rad/s)	
0.55 m (10%)	0.2079	1.1	1	0.2079	1.1
4.40 m (80%)	0.2079	1.1	5	0.2079	1.1

Linear ramping of the oscillation amplitude was used over the first three periods of motion for high frequency cases and the first period at low frequency. This approach smooths the transition from initial conditions to full amplitude motion, minimizing transients in the response and helping iterative convergence over the first few time steps. To initialize forward speed cases, the model was run in a static condition at $F_n 0.3$ until a steady state solution was reached. Eight inner iterations were performed during each time step. For select cases, STAR-CCM+ was run without the effect of viscosity and congruently with no prism mesh of the boundary layer. In this configuration, STAR-CCM+ solves the Euler equations and is similar to NFA. Table 7 gives the abbreviations used to denote STAR-CCM+ results.

Table 7. STAR-CCM+ Abbreviations

Abbr.	Program Name	Theory Type
SC	STAR-CCM+	RANS
SC_I	STAR-CCM+	EULER

4.2.1 Computational Mesh and Approach

An overset mesh is used to facilitate heave and pitch motion of the ONRTH. While rigid and deforming mesh motion options are available tools in STAR-CCM+, these methods have distinct disadvantages for large amplitude motion. Rigid oscillation presents difficulties for free surface refinement, particularly in pitch, and deforming meshes can cause cell quality issues. The overset region encompasses the body and moves with the prescribed body motion relative to a static background mesh of the entire domain. In the region of overlap between background and overset regions, cells are defined as active, inactive or acceptor cells. Active cells solve the discretized governing equations in a typical manner, while no calculations are performed in inactive cells. Coupling between the two regions is executed by the acceptor cells. These cells separate the active and inactive regions of the background mesh, and completely ring the outer boundary of the overset region which is otherwise composed of active cells. Acceptor cells adopt values interpolated from the nearest four active cells, or donor cells, in the other region. The acceptor cell is necessary for a solution to the discretized governing equations in interior cells in the absence of a boundary condition at the overset/ background region interface. A linear interpolation between cells is employed which applies a weighting factor to the donor cell values based on a shape function which spans the tetrahedron composed of the surrounding donor cell centroids. The variable value in an acceptor cell is described as

$$\varphi_{acceptor} = \sum \alpha_i \varphi_i \quad (20)$$

Where α_i is the weighting factor and φ_i is the variable value of the donor cell for i equal to 1 through 4. Figure 18 and Figure 19 show centerline views of the overset and background meshes respectively with acceptor cells shown in blue, active cells in yellow and inactive cells in red. The ONRTH is positioned at a positive (bow down) pitch angle of 5 degrees. An additional view of the mesh is shown in Figure 20, in which the overset mesh is in red and the background mesh in blue, in order to illustrate more clearly the overlapping acceptor cells.

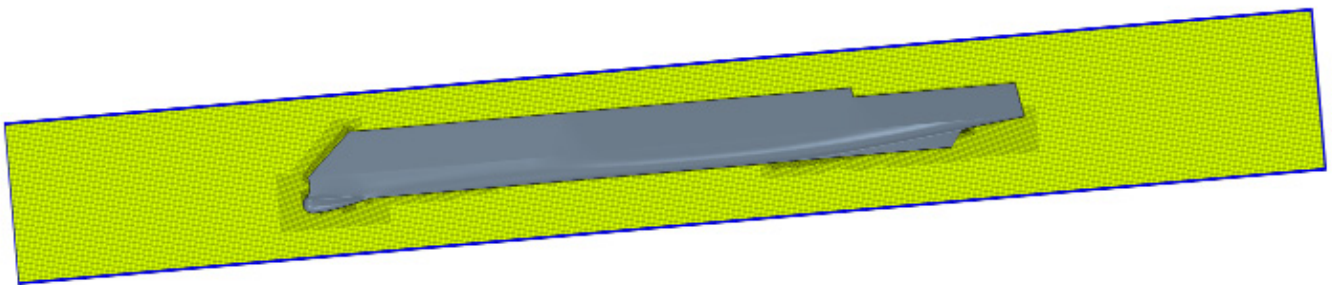


Figure 18. Overset mesh: acceptor cells in blue, active cells in yellow

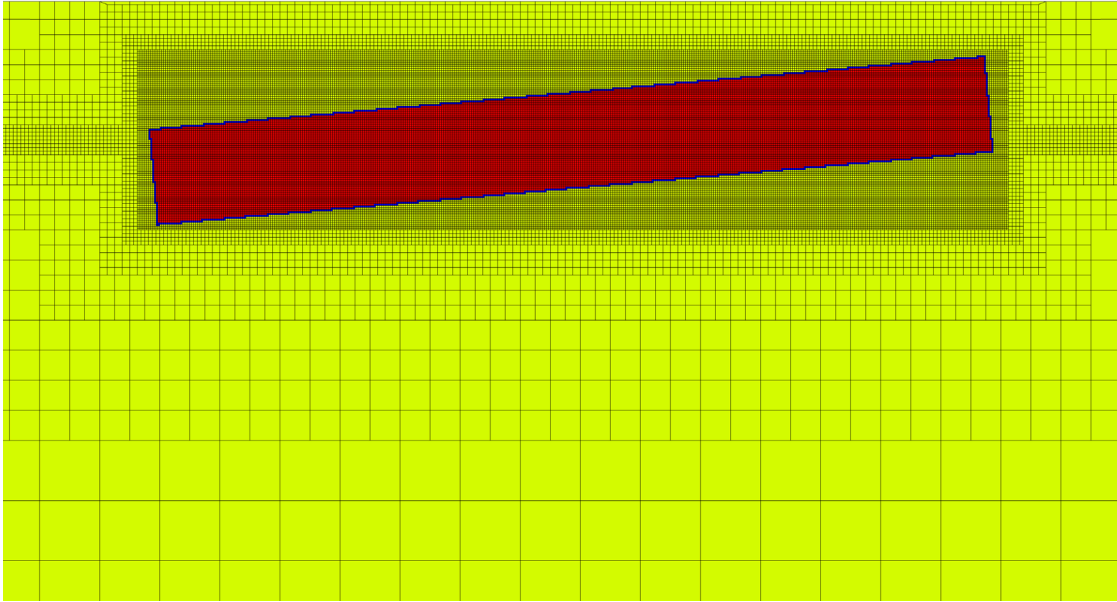


Figure 19. Background mesh: acceptor cells in blue, active cells in yellow, inactive cells in red

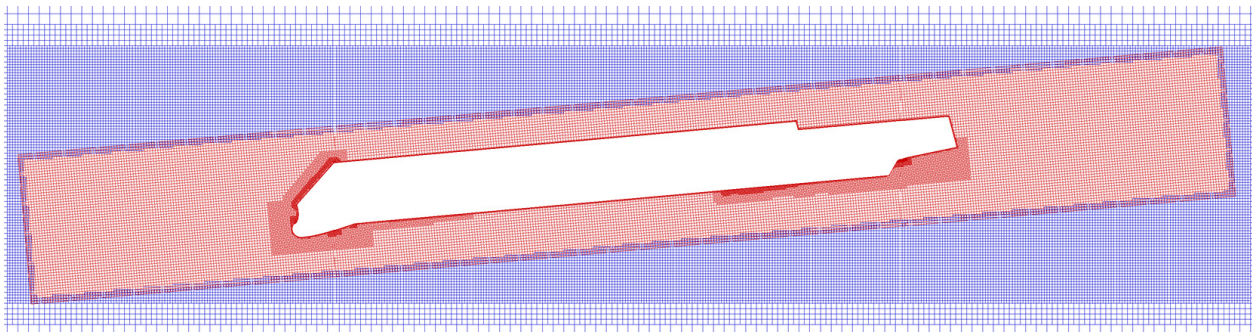


Figure 20. Overset Region in red, background region in blue

The overset and background regions are composed of trimmed hexahedra with 4.1 and 7.2 million cells respectively in the fine mesh. Many background mesh cells in the overlapping region are inactive such that the number of cells for which a solution is obtained is approximately 10.1 million. The size of the overset region is designed to limit flow variability near the coupling boundary while minimizing background mesh refinement requirements. The background mesh extends $21L$ to each side of the ship and L below the waterline. Over the last $20L$ the mesh aspect ratio increases with distance from the body to create a numerical beach, effectively eliminating contamination of the solution by reflected wave energy. Refinement of the overset and background mesh in the overlap region is the same. The mesh is locally refined in areas of interest near the body and along the free surface with a prism layer mesh of the boundary layer. The first prism layer grid line is placed 0.15 mm from the body such that the average y^+ is less than 30 for all cases and the boundary layer resolution is in the near-wall-resolving or blended regime. The prism layer mesh is composed of 12 layers and extends 31.25 mm in the direction normal to the body. Solutions are sought only for motion in the vertical-plane. Therefore, a symmetry plane is placed at the centerline to reduce the total cell count. At

zero forward speed, all domain boundaries were taken as pressure outlets. At forward speed, the forward boundary was defined as a velocity inlet boundary.

4.2.2 Mesh and Time Step Uncertainty

For a CFD simulation, error and uncertainty in the solution occur from two sources: modeling and numerical calculation. Modeling errors are related to the assumptions made in the mathematical representation of a physical problem. Sources of these errors include the governing equations, boundary conditions and turbulence models. Assessing the modeling error is termed validation, and may only be performed if corresponding experimental data is available. Because no experimental data is available for the ONRTH in prescribed heave and pitch or incident waves, the focus was on estimating the error in the numerical prediction. Numerical error is the result of approximations made in determining a solution to the modeled problem. These errors stem mainly from discretization of the problem in space and time, iterative solution techniques and computer round-off. Solution verification is the process of estimating these errors, or bounding their true value within some uncertainty interval for a specific application.

For this study, discretization errors due to grid spacing and time step are assumed to be the only significant contributions to the numerical uncertainty. To assess these uncertainties, and thus the suitability of the selected grid and time step for the present simulations, convergence studies were undertaken using the solutions on three grids and with three time steps. To the extent possible, with an unstructured grid and prism layer mesh of the boundary layer, similarity was maintained between grids. Medium and coarse meshes were created from the fine mesh described in *Section 4.3.1* by increasing cell size in all directions outside the prism layer by a refinement factor $r_g = \Delta x_{g_2} / \Delta x_{g_1}, \sqrt{2}$. In the prism layer the tangential cell spacing was changed by $\sqrt{2}$, while the wall-normal spacing was held constant. A time step of 0.01 s was used for all grid convergence simulations. Time step sensitivity was determined on the fine mesh using time steps of 0.04, 0.02 and 0.01 s such that the time step refinement factor, $r_t = dt_{t_2} / dt_{t_1}$, is equal to 2. Cases of 1.1 rad/s frequency and 4.4 m or 5 degree amplitude of oscillation in heave and pitch were chosen for uncertainty analysis since they represent the most extreme cases considered. A zero forward speed condition was used because cases with forward speed required much greater run times. CFL numbers are on typically below 0.4 for these cases with a time step of 0.01 s on the fine grid, though occasional local values exceed 1.

A systematic approach to verification proposed by Stern et al. [26] with factor of safety method [27] was used to obtain estimates of the uncertainty associated with the grid spacing and time step. The verification quantities of interest are force and moment on the body over one period of motion, which for the cases examined are highly nonlinear. Two approaches were taken in determining the time dependent solution differences between the fine, medium and coarse mesh or time steps. In the first approach, referred to subsequently as the “normalization” option (e.g. [28]), solutions on each grid, or using each time step, are matched at discrete points in time, and the solution change obtained. L2 norms of the solution change at all points in time are then used to determine global values for convergence ratio and observed order of accuracy. The “harmonic” approach (e.g. [8, 29]) utilizes solution changes between the mean value, F_0 , first harmonic amplitude F_1 , and phase, θ_1 , of each time history. Since single response quantities for the entire period are considered, instead of the value at each discrete point in time, normalization of the solutions is not necessary. Eqn. 21, 22 and 23 show the solution changes and solution change ratios respectively, where S_k is the solution for the k study (grid (g), time

step (t)), and the numerical subscripts give the refinement level with 1 indicating the finest mesh or smallest time step.

$$\varepsilon_{k_{21}} = S_{k_2} - S_{k_1} \quad (21)$$

$$\varepsilon_{k_{32}} = S_{k_3} - S_{k_2} \quad (22)$$

$$R_k = \varepsilon_{k_{21}} / \varepsilon_{k_{32}} \quad (23)$$

Three convergence conditions are possible; monotonic ($0 < R_k < 1$, MC), oscillatory ($R_k < 0$, OC) and divergent ($R_k > 1$, D). Convergence ratios in the normalization approach may become ill-conditioned if one or more solution changes go to zero. To avoid this difficulty a global convergence ratio based on the L2 norm of solution changes at all points in time is used. Unfortunately, global convergence ratios cannot be less than zero and thus this approach may not be used to assess the oscillatory convergence condition. In addition, local divergence at some points may be ignored since global convergence ratios less than 1 are assumed to demonstrate monotonic convergence. For oscillatory convergence conditions assessed using the harmonic approach, uncertainty is simply estimated based on solution maxima, S_U , and minima, S_L , i.e. the uncertainty, $U_k = \frac{1}{2}(S_U - S_L)$. Uncertainty cannot be estimated if the solution is divergent. Convergence ratios obtained using each method are given in Table 8 and Table 9. Using the normalization approach all response quantities are judged to be monotonically converging. Several harmonics are shown to be diverging, partly due to the importance of higher order terms in the nonlinear response quantities which make examination of first order harmonics for solution convergence problematic in this case. Given monotonic convergence of the solutions, an approach based on Richardson extrapolation (RE) is used. Observed order of accuracy is estimated using L2 norms of the solution change in the normalization approach, or the harmonic solution change in Eqn. 24. This formula gives a poor estimate of the order of accuracy for solutions not in the asymptotic convergence range, which is typically the case for unsteady, three-dimensional seakeeping computations. To determine the proximity of the solution to the asymptotic range a distance metric is used, and is given in Eqn. 25 where $p_{k_{est}}$ is the assumed theoretical order of accuracy (2). When solutions are in the asymptotic range, $p_{k_{est}} = p_k$ and the distance metric is equal to 1. Distance metrics are not generally close to 1 in this case, as shown in Table 8 and Table 9, demonstrating that the solutions do not approach the asymptotic range.

$$p_k = \frac{\ln(\varepsilon_{k_{32}} / \varepsilon_{k_{21}})}{\ln(r_k)} \quad (24)$$

$$P_k = \frac{p_k}{p_{k_{est}}} \quad (25)$$

A RE estimate of numerical error is obtained for the finest grid or time step using Eqn. 26. While global convergence ratio and observed order of accuracy were determined using L2 norms of the solution change in the normalization approach, here $\varepsilon_{k_{21}}$ is the solution change at each discrete point in time. Thus, an RE estimate of error is obtained for all points in the time history, while the harmonic approach results in estimates for the mean and first harmonic. Since

the magnitude of the RE error estimate is indefinite and the sign indeterminable in this case, an uncertainty interval is utilized which ideally bounds the true numerical error with a 95% level of confidence. This interval is obtained by applying a safety factor based on the distance metric to the RE error as shown in Eqn. 27. Table 8 and Table 9 contain the safety factors for each convergence study and response quantity.

$$\delta_{RE_{k_1}}^* = \frac{\varepsilon_{k_{21}}}{r_k^{p_k} - 1} \quad (26)$$

$$U_k = \begin{cases} (2.45 - 0.85P_k) \left| \delta_{RE_{k_1}}^* \right| & 0 < P_k \leq 1 \\ (16.4P_k - 14.8) \left| \delta_{RE_{k_1}}^* \right| & P_k \geq 1 \end{cases} \quad (27)$$

Uncertainty over time is obtained in the normalization method, and is plotted as a bounds relative to the fine grid or time step solution ($S_{k_1} + U_k$) and ($S_{k_1} - U_k$) in Figure 21 through Figure 24. Solutions on the medium and coarse grid or time step are also shown. The bounds are highly oscillatory because of zero solution change at crossing points and large changes near local maxima caused by small differences in the phase and amplitude of higher order components. Comparing solutions at discrete points in time accounts for convergence of amplitude, but does not properly consider phase differences. A small change in phase may thus be accounted for in the normalization approach as a major change in amplitude and thus a large peak in uncertainty. Table 10 gives the L2 norm of the uncertainty bounds as a percentage of the force and moment peak-to-peak amplitudes. The uncertainty estimates obtained in the harmonic approach are also given, with uncertainty in the first harmonic amplitude given as a percentage of its magnitude in the fine case, and the phase as a percentage of 2π . The mean is shown as a percentage of the maximum between its value and the first harmonic amplitude. The normalization approach appears to give a consistent estimation commensurate with the relative level of variation between solutions in each response quantity. For example, uncertainty is smallest for the dominant modes (i.e. Fz for heave and My for pitch) while the responses containing the greatest nonlinearity have the highest uncertainty. For the cases considered, the grid spacing and time step uncertainties are generally on the order of 10% with a minimum of 1.95 % and maximum of 34.18 %. However, this estimation is probably overly conservative since it averages in local uncertainty maxima caused by scatter in the convergence. Due to strong nonlinearity in the solutions, examination of convergence by leading order harmonics provided disjointed results. For several quantities divergence occurred, while in others correlation between the uncertainty estimate and actual convergence was marginal. Overall, little confidence may be placed in the estimated uncertainty values for this case. Likely, this problem is simply ill-suited for uncertainty analysis according to current methods due to prominent nonlinearity in the response. However, a pragmatic comparison of the convergence study time histories in Figure 21 through Figure 24 gives some assurance that the fine mesh and time step are reasonable for this case.

Table 8. Verification parameter results: heave, frequency 1.1 rad/s, amplitude 4.4 m, Fn 0.0

		Grid Convergence			Time Step Convergence		
		R_g	P_g	FS_g	R_t	P_t	FS_t
Normalization	Fx	0.79	0.33	2.17	0.76	0.39	2.12
	Fz	0.66	0.60	1.94	0.51	0.97	1.63
	My	0.82	0.30	2.20	0.85	0.23	2.25
Harmonic	Fx₀, Fx₁, θ_{x1}	-5.3, 3.3, 0.2	D,D,2.17	D,D,10.375	0.3, 0.1, 0.5	0.9, 1.5, 0.6	1.7, 9.1, 2.0
	Fz₀, Fz₁, θ_{z1}	6.8, 0.8, -5.5	D,0.38,D	D,2.13,D	0.08, 0.5, 0.9	1.9, 0.5, 0.1	15.5, 2.0, 2.4
	My₀, My₁, θ_{y1}	-1.9, 1.8, -1.1	D,D,D	D,D,D	0.9, 0.4, 0.3	0.1, 0.6, 0.8	2.4, 1.9, 1.7

Table 9. Verification parameter results: pitch, frequency 1.1 rad/s, amplitude 5 deg, Fn 0.0

		Grid Convergence			Time Step Convergence		
		R_g	P_g	FS_g	R_t	P_t	FS_t
Normalization	Fx	0.90	0.15	2.32	0.68	0.56	1.98
	Fz	0.62	0.70	1.86	0.62	0.69	1.86
	My	0.77	0.37	2.14	0.53	0.92	1.67
Harmonic	Fx₀, Fx₁, θ_{x1}	0.1, 1.2, 0.3	2.1, D, 0.8	54.6, D, 11.7	-1.6, 9.0, 0.5	D, D, 0.25	D, D, 2.0
	Fz₀, Fz₁, θ_{z1}	0.8, -0.2, -0.4	0.15, OC, OC	2.2, OC, OC	0.3, -0.1, 0.3	0.4, OC, 0.4	1.8, OC, 1.8
	My₀, My₁, θ_{y1}	1.9, -0.2, -3.8	D, OC, D	D, OC, D	2.0, -3.0, 0.2	D, D, 0.6	D, D, 2.9

Table 10. Grid and time step uncertainties: high amplitude and frequency, Fn 0.0

		Heave		Pitch	
		U_g	U_T	U_g	U_t
Normalization	Fx	12.77%	8.72%	30.19%	8.58%
	Fz	3.59%	1.95%	11.48%	9.10%
	My	31.92%	34.18%	11.83%	4.70%
Harmonic	Fx₀, Fx₁, θ_{x1}	D, D, 0.5 %	0.03,0.41,0.33 %	0.22, D, 0.89 %	D, D, 1.27 %
	Fz₀, Fz₁, θ_{z1}	D, 1.0, D %	0.02, 1.51, 7.22 %	8.94, 6.61, 2.21 %	0.26, 10.96, 0.43 %
	My₀, My₁, θ_{y1}	D, D, D %	6.56, 4.00, 0.06 %	D, 0.64, D %	D, D, 0.36 %

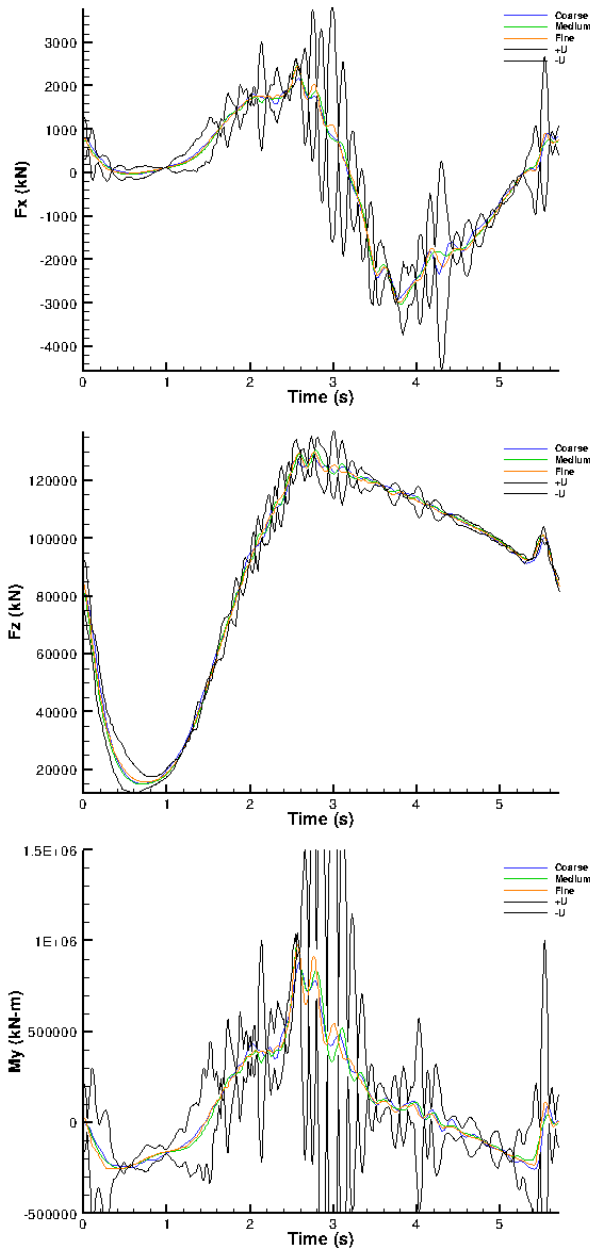


Figure 21. Grid refinement study, oscillation in heave at frequency 1.1 rad/s, amplitude 4.4 m and F_n 0.0: longitudinal force (top), vertical force (middle) and pitch moment (bottom)

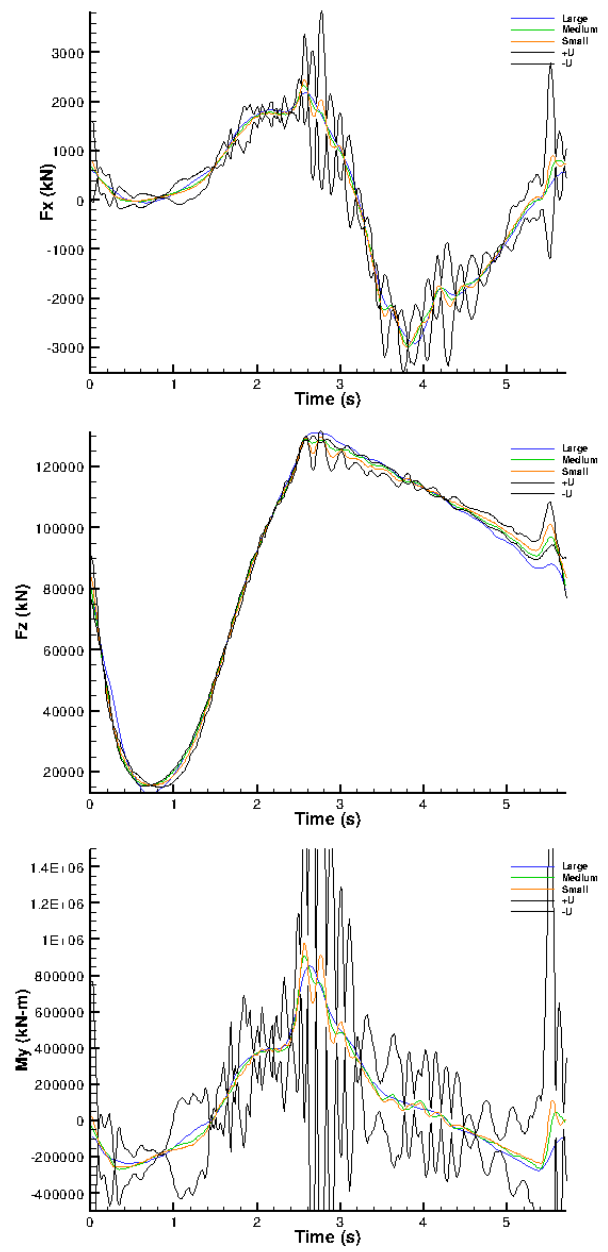


Figure 22. Time step refinement study, oscillation in heave at frequency 1.1 rad/s, amplitude 4.4 m and F_n 0.0: longitudinal force (top), vertical force (middle) and pitch moment (bottom)

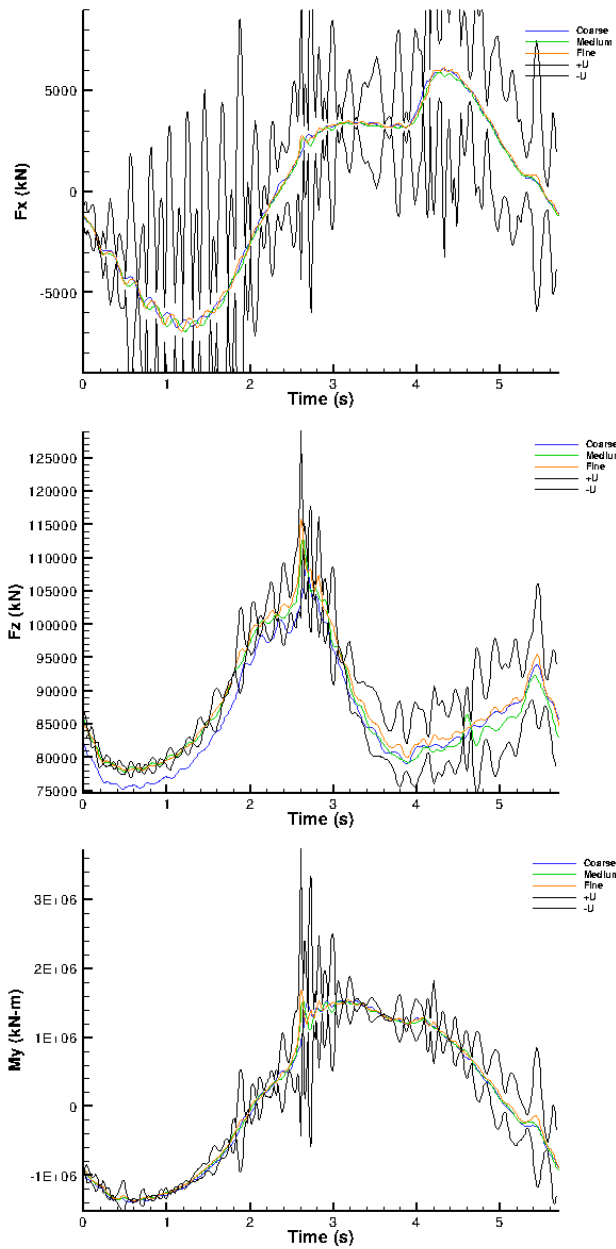


Figure 23. Grid refinement study, oscillation in pitch at frequency 1.1 rad/s, amplitude 5 deg. and F_n 0.0: longitudinal force (top), vertical force (middle) and pitch moment (bottom)

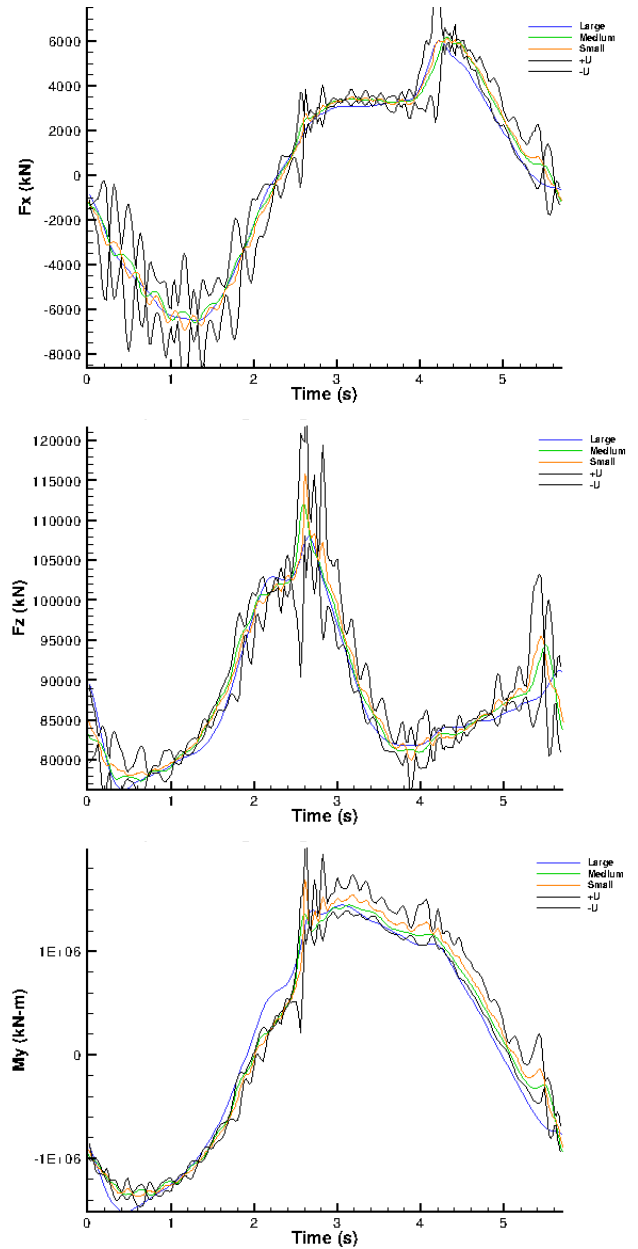









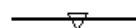


Figure 24. Time step refinement study, oscillation in pitch at frequency 1.1 rad/s, amplitude 5 deg. and F_n 0.0: longitudinal force (top), vertical force (middle) and pitch moment (bottom)

4.2.3 Force and Moment Results

Total force and moment results are given over one period of motion, exclude the weight vector and are relative to the ship fixed coordinate system. The various codes are represented by the legend given in Table 11. Results from NFA are only available for the cases of frequency 1.1 rad/s and amplitude 4.4 m or 5 degrees at forward speed. Inviscid solutions using STAR-CCM+ were obtained for oscillations of frequency 1.1 rad/s and amplitude 4.4 m or 5 degrees with no forward speed and F_n 0.3. Results are discussed in full only for these most extreme cases. However, some key observations from other cases are given and the complete results of all other cases are given in Appendix A.

Table 11. Legend for time history plots

	SC
	SC_I
	A1
	A2
	FD
	L1
	L3
	L4
	NF
	NS

4.2.3.1 Zero Forward Speed Cases

For low amplitudes of oscillation, 0.55 m or 1 degree for heave and pitch respectively, at zero forward speed the various potential flow codes and RANS solutions agree well. For motions with large amplitudes of 4.4 m or 5 degrees geometric nonlinearity becomes important. In particular, the emergence of the shallow transom of the ONRTH results in abrupt changes in waterplane area. The potential flow codes are separated in this regard by their approach to calculation of hydrostatic force and moment. In the low frequency case, this is the principal source of nonlinearity and the linear methods (A1, L1) do not agree with the blended and nonlinear potential flow results [2] or with the RANS results. This is demonstrated in Figure 25, which gives the pitch moment exerted on the hull for oscillation in pitch at frequency 0.2079 rad/s and amplitude 5 degrees. Over the first half of the period, nonlinearity is noticeable as the stern emerges above the free surface. Through the rest of the period, the response is approximately linear as the stern submerges below the calm waterline. A progression over time of the body position at centerline relative to the waterline is shown for pitch at frequency 0.2079 rad/s and amplitude 5 degrees in Figure 26.

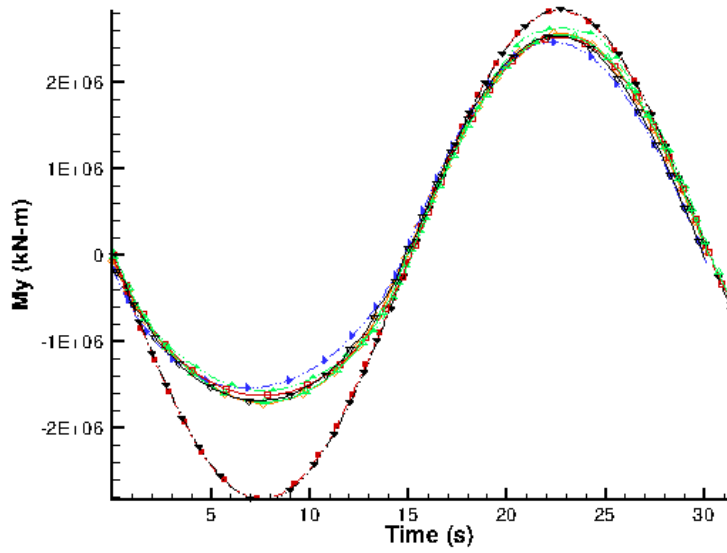


Figure 25. Pitch moment for oscillation in pitch at freq. 0.2079 rad/s, amp. 5 deg. and Fn 0.0

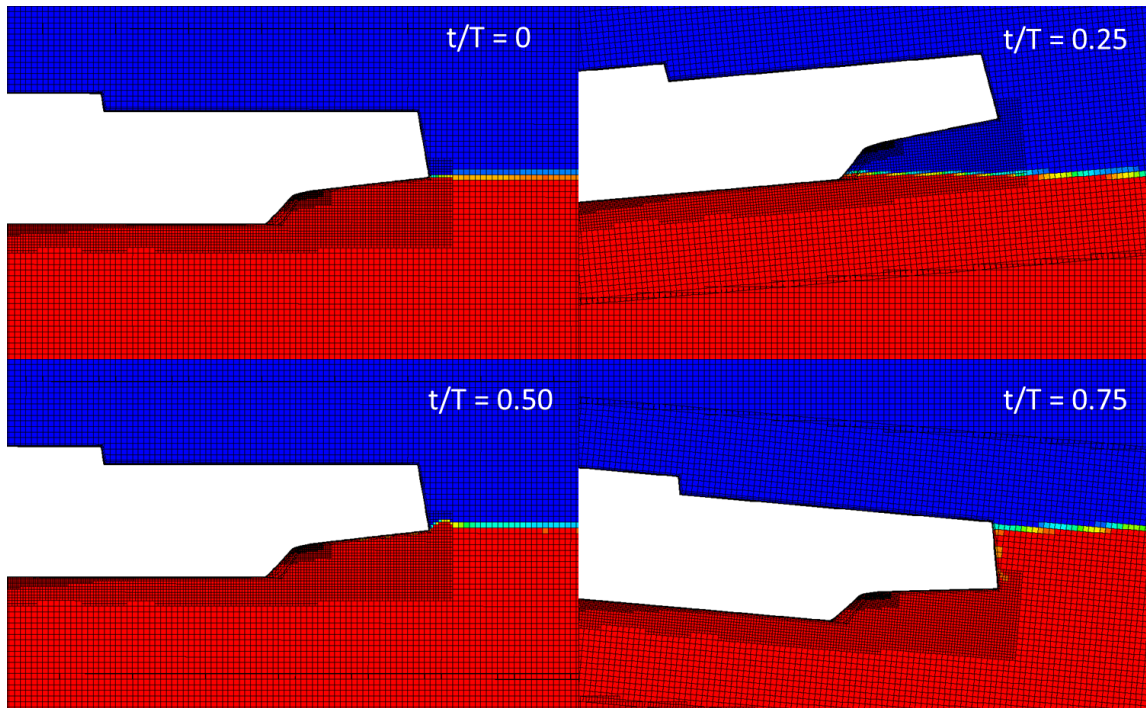


Figure 26. Centerline stern section free surface in pitch at freq. 0.2079 rad/s, amp.5 deg. and Fn 0.0

4.2.3.2 Forward Speed Cases

For low amplitude cases at both frequencies, the influence of forward speed sinkage force and trim moment effects are noticeable, though they are more than an order of magnitude lower than the hydrostatic component of force and moment. Figure 27 compares the vertical component of force from RANS at Fn 0.0 and 0.3 for heave motion of frequency 0.2079 rad/s

and 0.55 m amplitude. The sinkage effect at forward speed causes a net decrease in vertical force of approximately 4,000 kN. This effect varies with body position, causing less change in vertical force during the first half of the period when the body is above its mean position and increasing over the second half of the period as draft increases. The LAMP suite of codes includes a steady Kelvin component in the hydrodynamic force and moment at forward speed [2]. As shown by Figure 28 this results in a much closer agreement with the RANS result than the other potential flow codes which did not include such a correction.

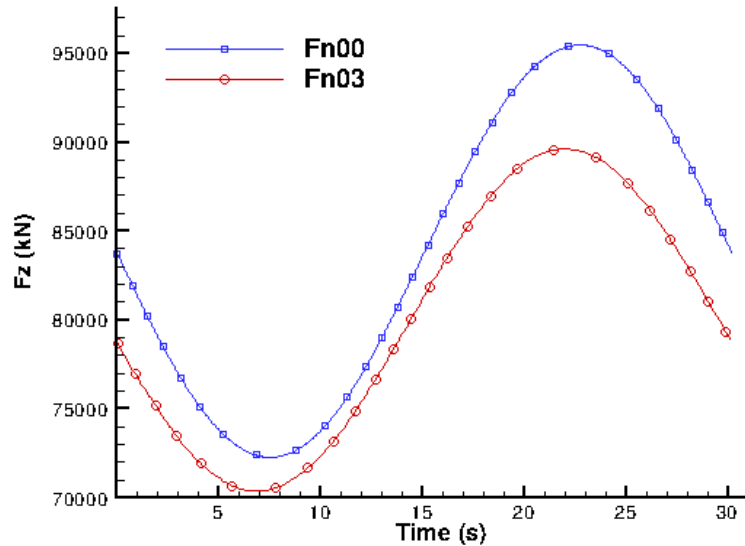


Figure 27. Vertical force from RANS for oscillation in heave at freq. 0.2079 rad/s, amp. 0.55 m, Fn 0.0 & 0.3

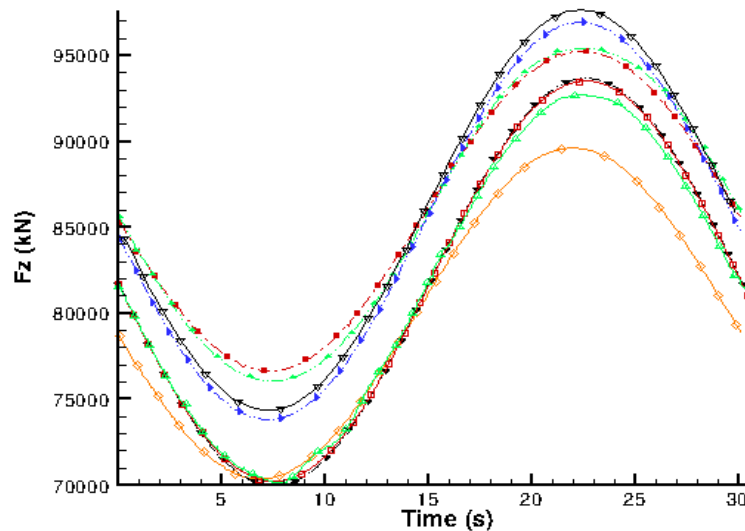


Figure 28. Vertical force for oscillation in heave at freq. 0.2079 rad/s, amp. 0.55 m, and Fn 0.3

4.2.3.3 Large Amplitude and High Frequency

The most interesting cases are those which show the greatest nonlinearity. These are prescribed oscillation at the largest amplitude, 4.4 m or 5 degrees, and frequency, 1.1 rad/s. In these cases, nonlinearity in the radiation force is important in addition to geometric nonlinearity since magnitudes of the hydrodynamic force and moment approach the hydrostatic magnitudes. Telste and Belknap [2] demonstrate this using separate plots of the potential flow radiation and hydrostatic components of force and moment. Of the cases considered, high amplitude and frequency is also most likely to exhibit a viscous influence on the solution which is captured by RANS but not the potential flow codes. Longitudinal force, vertical force and pitching moment are given in Figure 30 and Figure 31 for sinusoidal oscillation in heave and Figure 32 and Figure 33 for oscillation in pitch at F_n 0.0 and 0.3.

In Figure 30, a spike in heave force and pitch moment occurs between 2.6 and 2.8 s into the period of oscillation. This spike occurs as the shallow transom stern impacts the free surface while traversing downward toward the mean waterline. Here, the codes are especially distinct in their results for pitch moment, with the nonlinear potential flow and RANS solutions displaying a markedly different character than the blended and linear methods. In particular, the codes which do not account for nonlinearity in the radiation force miss the peak in the pitch moment time history. There is also some difference between the RANS solution and nonlinear potential flow results. The cause of this discrepancy is likely their treatment of free surface nonlinearities and viscous effects since the nonlinear radiation and hydrostatic forces are considered in both methods. Visualization of the STAR-CCM+ solution for this case in Figure 29 shows that the free surface beneath the stern is highly disturbed prior to impact due to perturbations created on the previous upstroke.

The forward speed case in which the body is undergoing prescribed heave oscillation of 4.4 m amplitude and 1.1 rad/s frequency given in Figure 31 shows a result similar to that for prescribed heave oscillation of the same amplitude and frequency with no forward speed. Solutions from NFA and STAR-CCM+ both display a difference in phase relative to the nonlinear potential flow results over the first 2 s of the period. Between 2.6 and 2.8 s the STAR-CCM+ solutions exhibit a smaller peak heave force magnitude than NFA, LAMP-4 and NSHIPMO which all agree well. In addition, the peak in pitch moment appears to occur slightly earlier in the period for the STAR-CCM+ solution than for the other nonlinear methods. Through the entire period, the two STAR-CCM+ solutions are in close agreement, except for greater noise in the inviscid result due to less dissipation. It is interesting that the STAR-CCM+ inviscid solution agrees more closely with the RANS result from the same code, than with NFA which also assumes zero viscosity. In either case, the numerical viscosity inherent in the scheme prohibits a straightforward comparison with potential flow. VOF methods capture the nonlinear free surface by tracking volume-fractions to the extent allowed by a given spatial discretization whereas nonlinear potential flow codes may employ some linearization of the free surface to avoid computational difficulty. For instance, the Lamp-4 code linearizes the free surface boundary condition with respect to the incident wave [30]. This approach assumes that radiated wave heights are small relative to the incident wave. Given that the radiated wave amplitude is approximately equal to the amplitude of prescribed heave oscillation, or 80% of the draft in this case, and the STAR-CCM+ solution shows that this wave is breaking near the body, that assumption is violated.

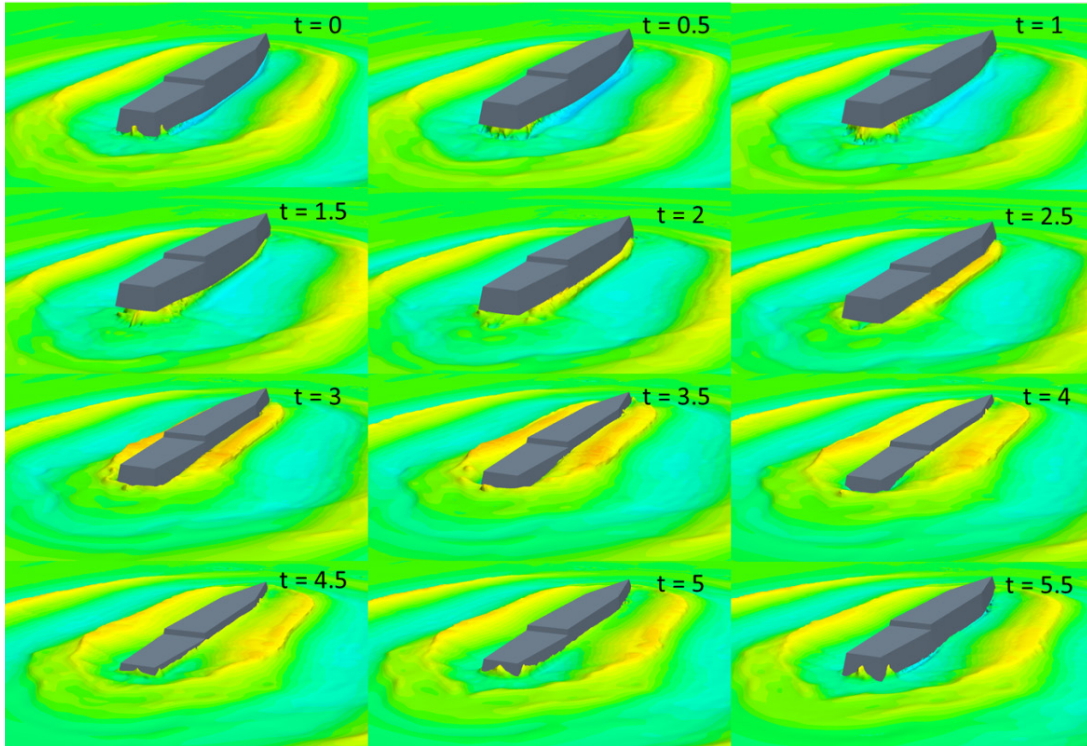


Figure 29. Time history of free surface: heave oscillation, freq. 1.1 rad/s, amp. 4.40 m, & Fn 0.0

The radiation pitch moment for prescribed oscillation in pitch at frequency 1.1 rad/s and amplitude 5 degrees given by Telste and Belknap [2] has a magnitude near that of the hydrostatic pitch moment, and is nearly 180 degrees out of phase. The hydrostatic pitch moment is also approximately linear. Consequently, the total pitch moments shown in Figure 32 and Figure 33 for Fn 0.0 and Fn 0.3 respectively are sensitive to nonlinearities in the predicted radiation force. Again, the RANS and nonlinear methods match closely while the character of the blended and linear potential flow solutions differ significantly. Also, there is a slight difference between VOF and nonlinear potential flow solutions, which is most apparent in the vertical force result. In this case there does not appear to be any notable difference between NFA and the STAR-CCM+ solutions. As in heave motion, significant deformations of the free surface are apparent in the STAR-CCM+ solution, including local wave breaking. However, the influence of free surface phenomena on the force and moment results cannot be examined independently since viscous effects and simulation characteristics unrelated to the underlying theory also introduce differences between the solutions from each code. An example of the effect of viscosity is shown in Figure 34. Here, velocity vectors and vorticity contours of a transverse, two-dimensional section at 95% of the ship length, or midway on the rise between the baseline and transom stern, are depicted. The water phase is shown only for cells in which the volume fraction of water is greater than 50 % so spray modeled by the VOF method is not visible. Separation is evident around the sharp bilges of the section as it travels vertically at $t = 0, 5$ and 5.5 s. The effect is rather similar to that realized by a two-dimensional rectangular cylinder in *Section 3.3.2*. As with the rectangle, there is likely some nonlinear viscous influence on the hydrodynamic response. However, in the RANS solution for this case, the ONRTH stern emerges above the calm waterline and viscous effects coalesce with deformation of the free

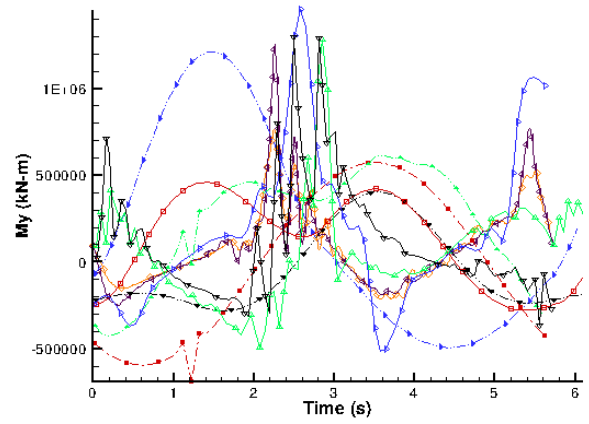
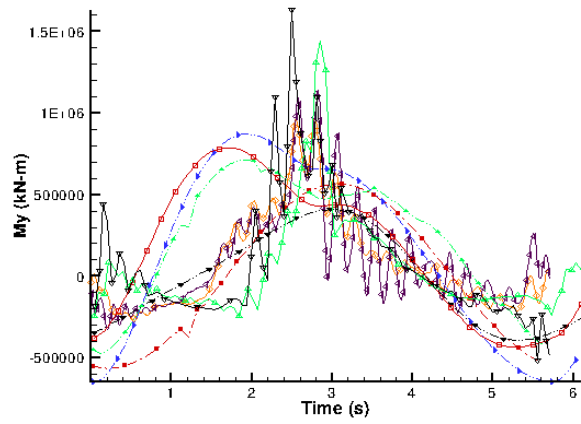
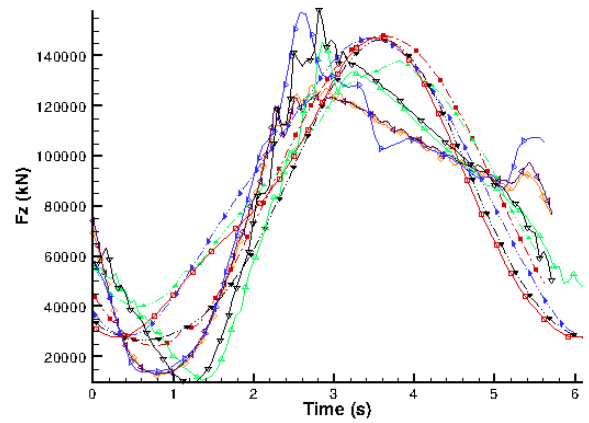
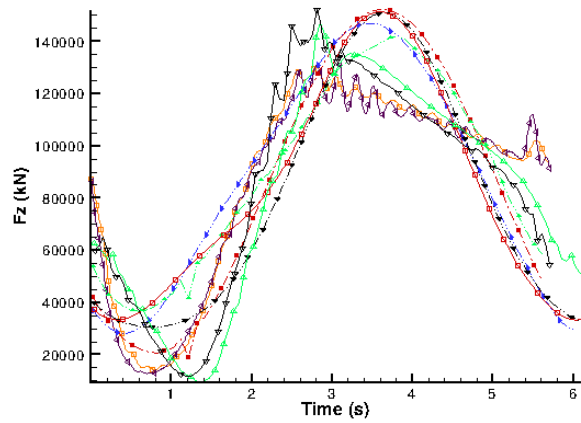
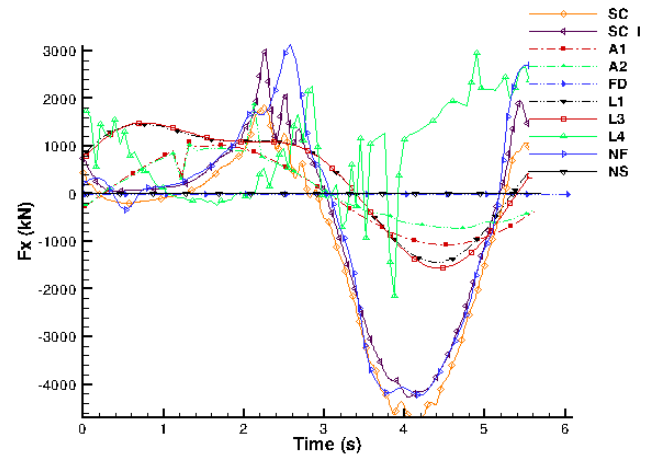
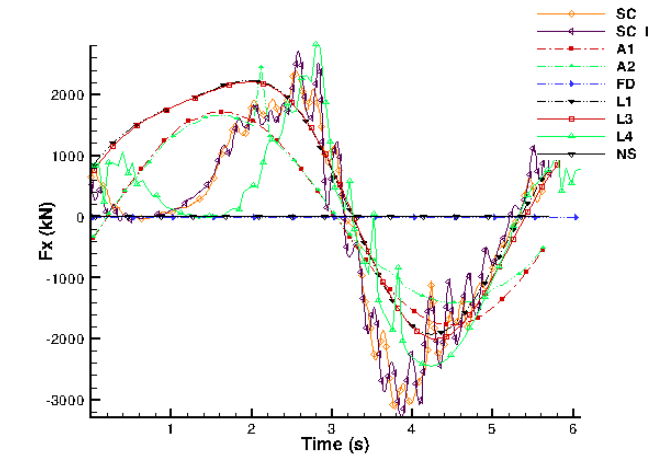


Figure 30. Oscillation in heave at frequency 1.1 rad/s, amplitude 4.4 m and F_n 0.0: longitudinal force (top), vertical force (middle) and pitch moment (bottom)

Figure 31. Oscillation in heave at frequency 1.1 rad/s, amplitude 4.4 m and F_n 0.3: longitudinal force (top), vertical force (middle) and pitch moment (bottom)

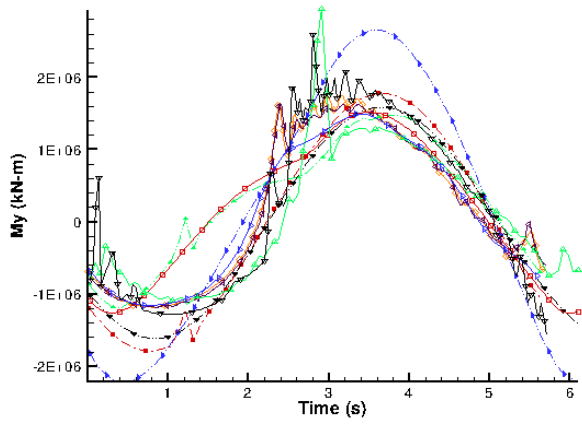
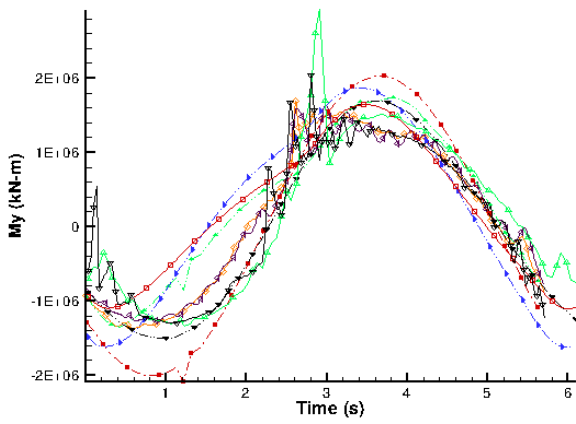
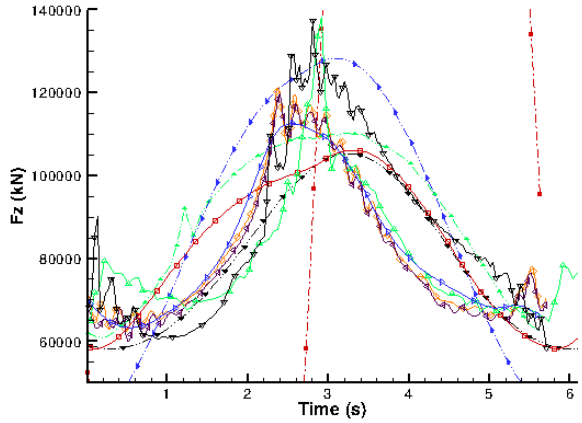
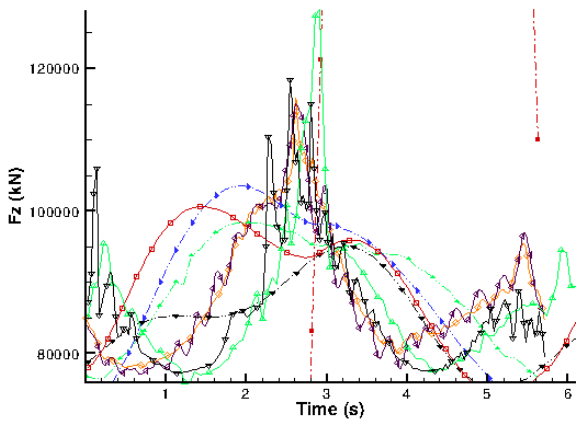
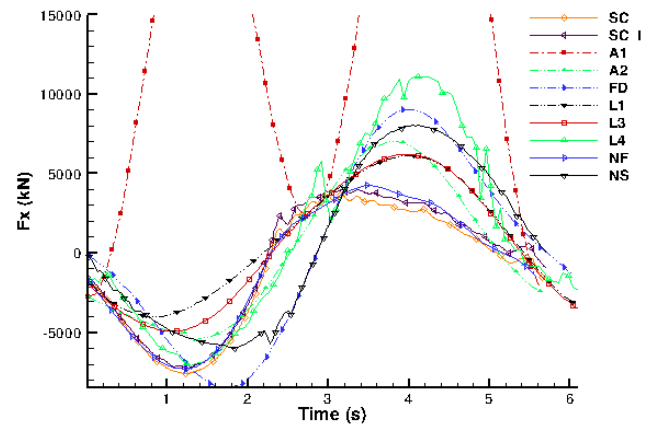
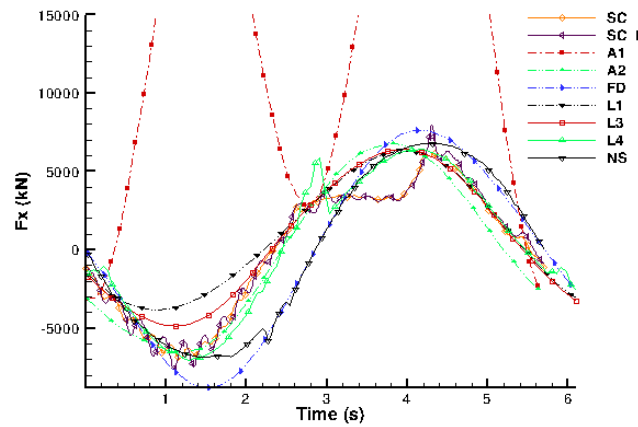


Figure 32. Oscillation in pitch at frequency 1.1 rad/s, amplitude 5 deg. and Fn 0.0: longitudinal force (top), vertical force (middle) and pitch moment (bottom)

Figure 33. Oscillation in pitch at frequency 1.1 rad/s, amplitude 5 deg. and Fn 0.3: longitudinal force (top), vertical force (middle) and pitch moment (bottom)

surface in a complicated flow field which induces hydrodynamic nonlinearities dependent upon previous interactions.

For the forward speed case of prescribed pitch with frequency 1.1 rad/s and 5 degree amplitude in Figure 33, the LAMP-4 vertical force is in better agreement with the VOF solutions than NSHIPMO over the second half of the pitch cycle as the stern reenters the water. Perhaps some three-dimensional effect is influential. However, the general character of the nonlinear strip-theory method NSHIPMO is still very near the other nonlinear methods. In fact, it is notable that the prediction of heave force and pitch moment by the two-dimensional method is generally quite similar to the three-dimensional, nonlinear code LAMP-4 [31] and the VOF methods NFA and STAR-CCM+ for all cases.

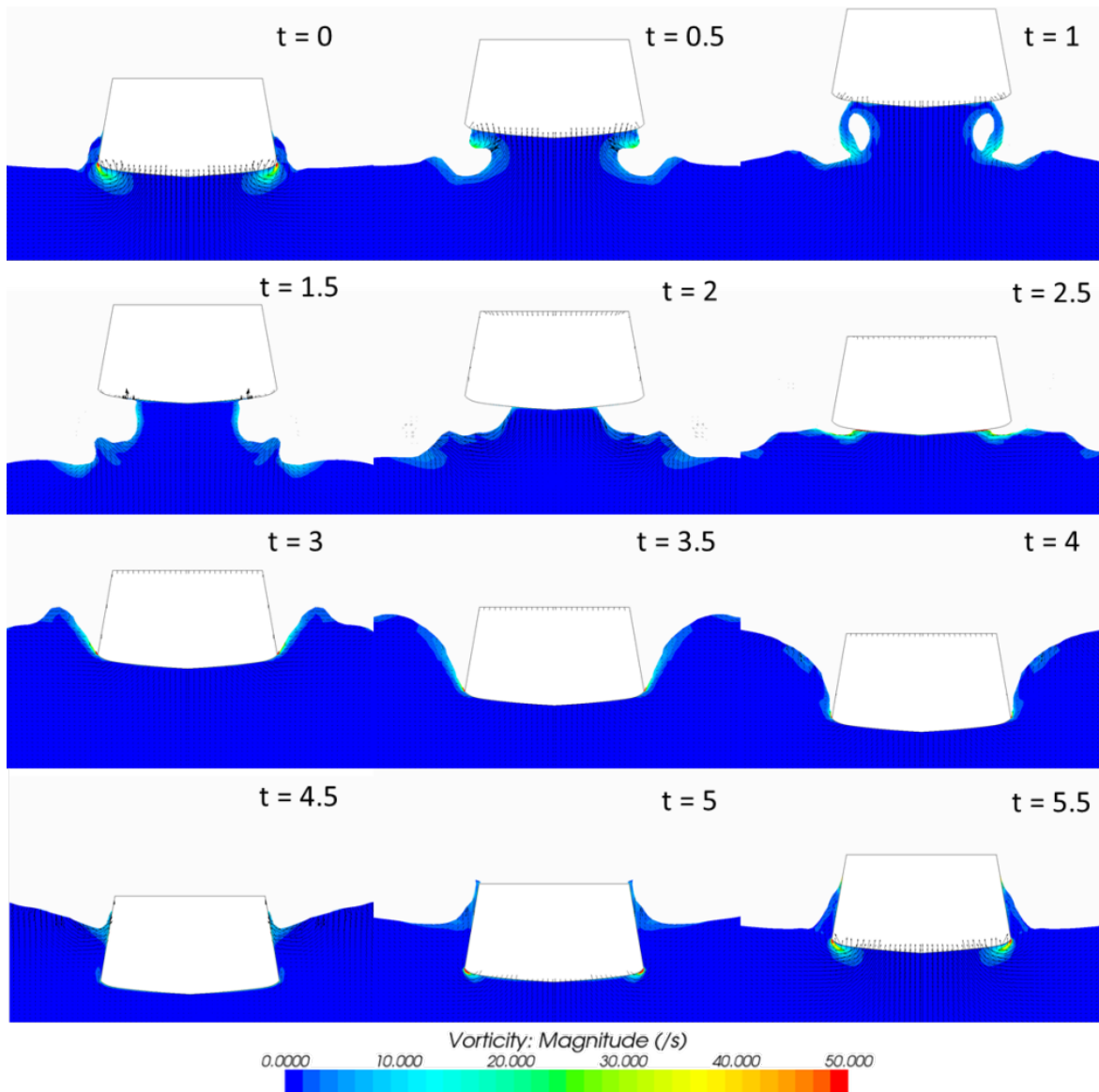


Figure 34. Velocity vector and vorticity contour time history from RANS for transverse section at 95% of L: oscillation in pitch at frequency 1.1 rad/s, amplitude 5 deg., and Fn 0.0

4.2.4 Evaluation of Simulation Parameters

In addition to examining the uncertainty associated with grid and time step refinement, several other parameters were considered in their effect on the solution. Figure 35 and Figure 36 show a comparison between 2nd and 1st order temporal discretization schemes for cases of 1.1 rad/s frequency and 4.4 m or 5 degree amplitude of oscillation in heave and pitch at zero forward speed. While a 2nd order discretization of the transient term offers greater accuracy for an unsteady simulation, the results show that a 1st order solution does not differ significantly for the chosen time step. Moreover, a 1st order scheme offers substantial benefits in stability and computational time. A 1st order temporal solution on a mesh which is body-fixed and rigidly oscillated is also shown for heave motion of 1.1 rad/s frequency and 4.4 m amplitude in Figure 35. In this mesh motion implementation, body oscillation involves translation of the entire domain rather than an overset region surrounding the body. The grid refinement used in this mesh is similar to that of the overset mesh. Close agreement between the rigid and overset mesh solutions confirms that no significant errors are introduced by interpolation between the overset and background regions of the overset mesh for this case.

Figure 37 and Figure 38 show solutions for cases of 1.1 rad/s frequency and 4.4 m or 5 degree amplitude of oscillation in heave and pitch respectively at zero forward speed using a $k-\omega$ turbulence model. Previously discussed solutions obtained using the $k-\varepsilon$ model are given for comparison. The formation and diffusion of vorticity about sharp edged stern sections does differ somewhat between methods. However, the difference between the two solutions is slight for both heave and pitch motion. This is in contrast with the findings for a two-dimensional rectangular cylinder in heave which showed that significant differences in force on the body resulted due to disparities in the formation and propagation of eddies approximated by the respective turbulence models during large amplitude motion.

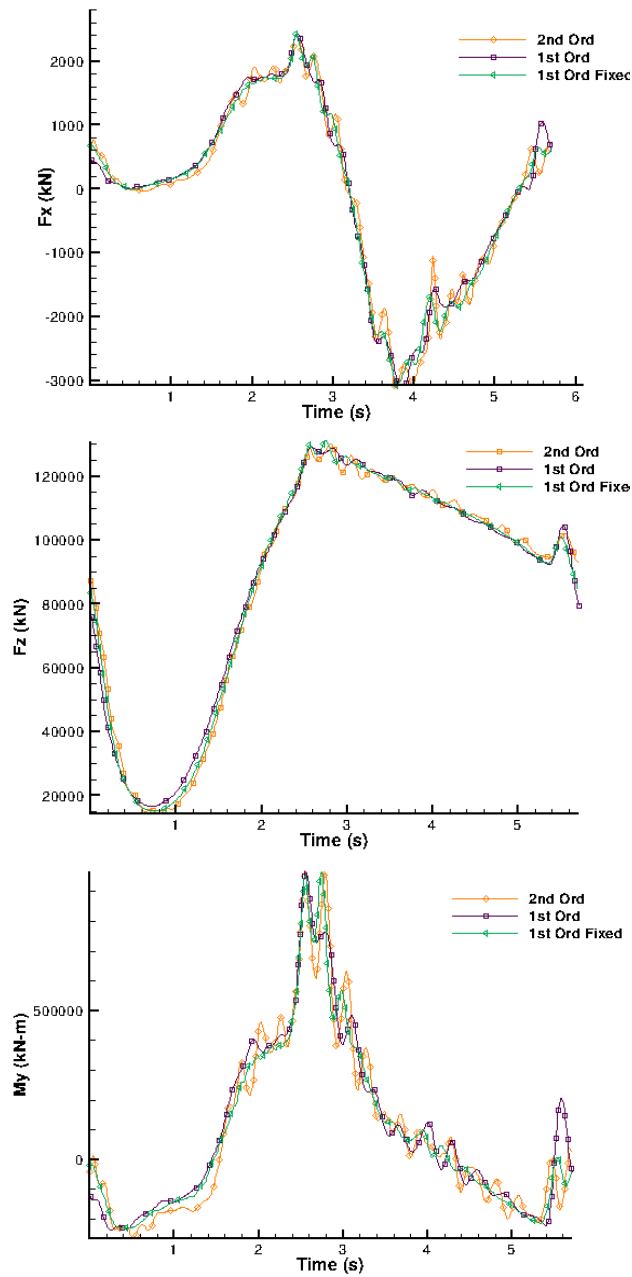


Figure 35. Comparison of temporal discretization order and fixed mesh; oscillation in heave at frequency 1.1 rad/s, amplitude 4.4 m and Fn 0.0: longitudinal force (top), vertical force (middle) and pitch moment (bottom)

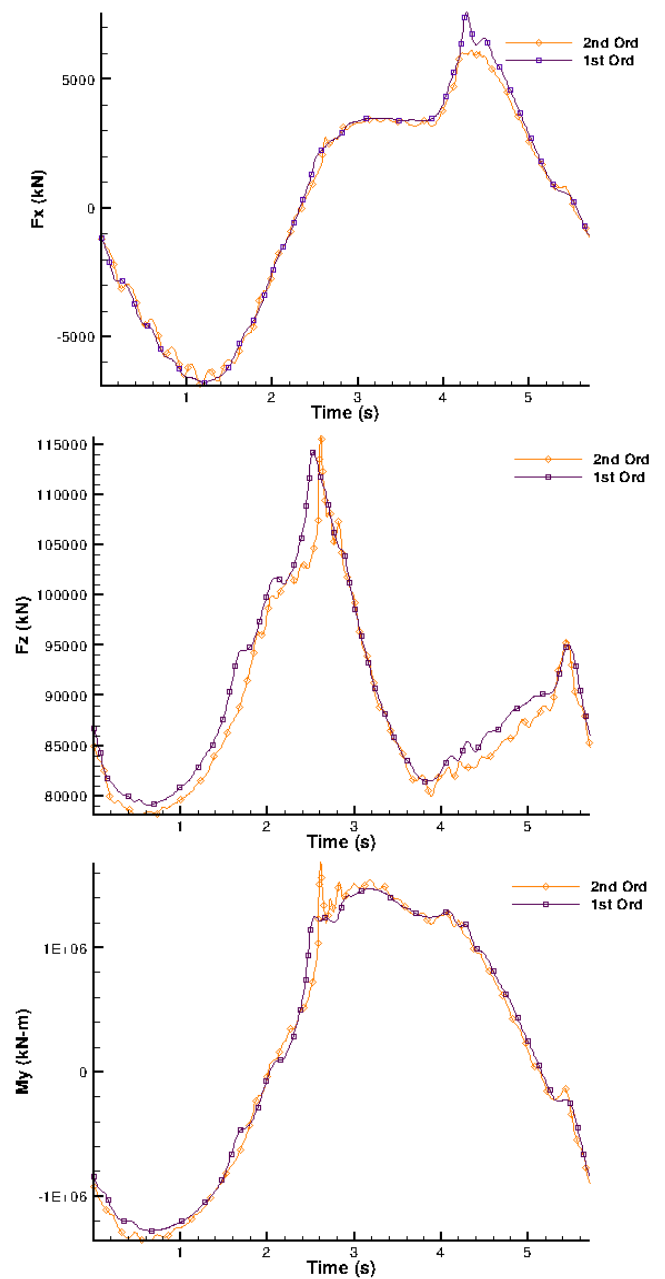


Figure 36. Comparison of temporal discretization order; oscillation in pitch at frequency 1.1 rad/s, amplitude 5 deg. and Fn 0.0: longitudinal force (top), vertical force (middle) and pitch moment (bottom)

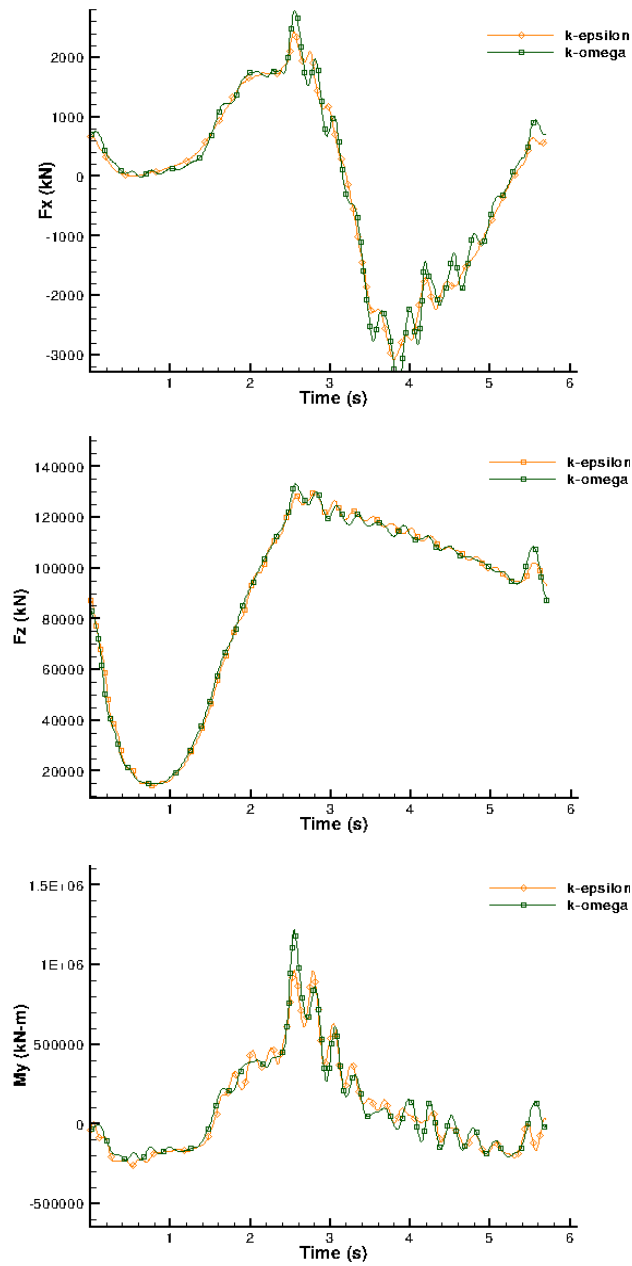


Figure 37. Comparison of $k-\epsilon$ and $k-\omega$ turbulence models; oscillation in heave at frequency 1.1 rad/s, amplitude 4.4 m and F_n 0.0: longitudinal force (top), vertical force (middle) and pitch moment (bottom)

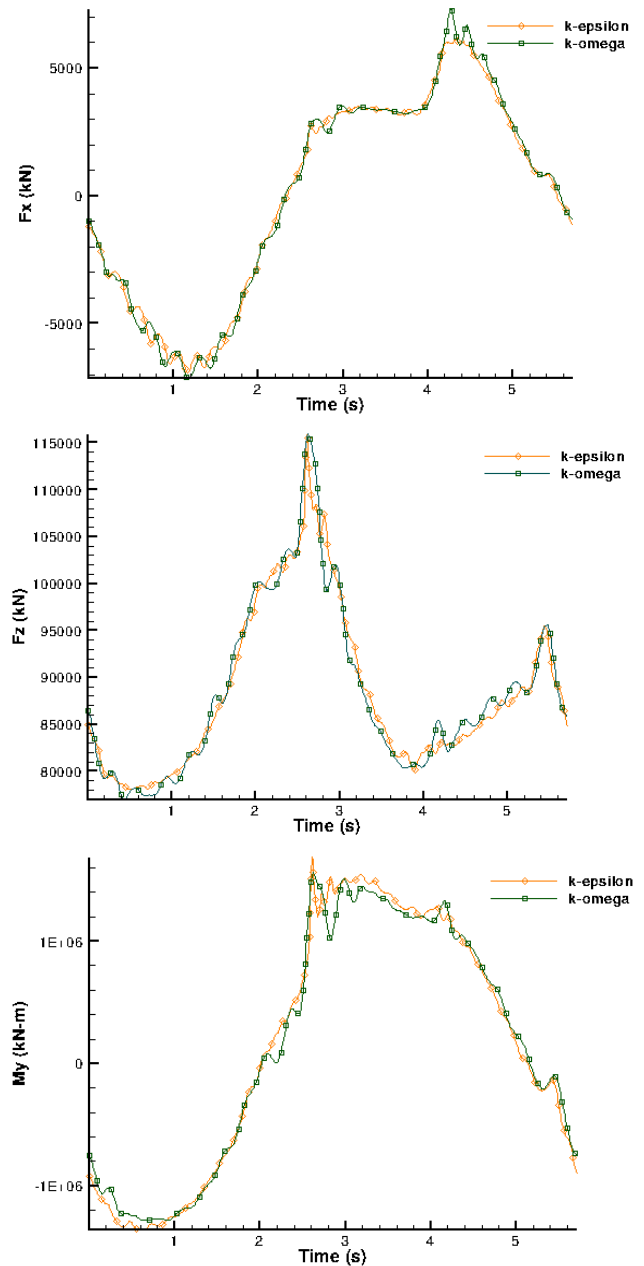


Figure 38. Comparison of $k-\epsilon$ and $k-\omega$ turbulence models; oscillation in pitch at frequency 1.1 rad/s, amplitude 5 deg. and F_n 0.0: longitudinal force (top), vertical force (middle) and pitch moment (bottom)

4.3 FIXED 0 DOF IN HEAD WAVES

ONRTH is examined in a 0-DoF fixed condition with incident head waves ($\beta=180^\circ$) at both zero speed and constant forward speed ($F_n=0.3$). This is commonly referred to as the diffraction problem. The smallest and largest wave steepnesses examined in the Force Study are considered to include cases in the linear regime and in which nonlinearity is likely important. The tested wave amplitudes, a , are 1.28 and 7.70 m, and wave steepness H/λ is 1/60 and 1/10. The wavelength, λ , in each case is equal to the ONRTH ship length or 154 m and deep water waves are assumed in all cases. Both forward speed and F_n 0.3 are examined. Table 12 gives the considered conditions.

Table 12. Fixed in head waves cases

H/λ	λ/L	a (m)	β ($^\circ$)	F_n	
1/10	1	7.70	180	0.0	0.3
1/60	1	1.28	180	0.0	0.3

Using linear wave theory the free surface elevation is given in the form

$$\eta = a \cos(kx - \omega t) \quad (28)$$

And the encounter period, T_e , is approximated as

$$U = F_n \sqrt{gL} \quad (29)$$

$$\omega = \sqrt{2\pi g/\lambda} \quad (30)$$

$$\omega_e = \omega - (\omega^2 U/g) \cos \beta \quad (31)$$

$$T_e = 2\pi/\omega_e \quad (32)$$

Where F_n is the Froude Number, U is the body velocity and β is the angle of incidence with 180° defined as head waves. Using Equations 29-32 the estimated encounter period of the chosen wavelength is 9.93 and 5.67 s for zero speed and F_n 0.3 respectively. The linear theory is valid only for small wave steepnesses. Several higher order theories are available which for deep water waves follow the Stokes expansion. For wave input conditions, either boundary or initial conditions, STAR-CCM+ offers linear waves and a 5th order Stokes theory approximation.

4.3.1 Computational Mesh and Approach

The overset mesh described in *Section 4.2.1* for prescribed motions of the ONRTH is employed again here with some differences. Extruded cells of increasing aspect ratio which began at a distance L forward of the ship and continue to the inlet boundary are eliminated. These cells created a numerical beach which dampened radiated waves during prescribed heave and pitch, but would distort incident waves in head seas before they encounter the body. Similar cells are maintained aft of the ship in order to dampen diffracted waves and the incident wave as it passes downstream of the body. Waves are additionally dampened in the zero forward speed case by introducing a smoothly increasing vertical resistance starting $2L$ aft of the ship and

continuing to the outlet boundary located 5L aft of the ship. The free surface region is further refined with cell sizes tailored to each wave steepness. Wave heights are discretized by 24 and 32 cells for wave amplitudes of 7.70 and 1.28 m respectively. Using aspect ratios greater than 1 in the free surface region there are 124 cells across the wavelength in each case. In the overset region an aspect ratio of 1 is maintained and the mesh is the same as shown in Figure 18 except for further refinement of the free surface in the vertical direction. Overset meshes are composed of 4.1 and 8.7 million cells and the background meshes contain 7.4 and 13.2 million cells for the large and small amplitude wave conditions respectively. Figure 39 shows the overset mesh in red and background mesh in blue for each wave amplitude. Though an overset mesh has no benefit in this static case, it is employed in order to examine the interpolation of waves across the background to overset mesh interface.

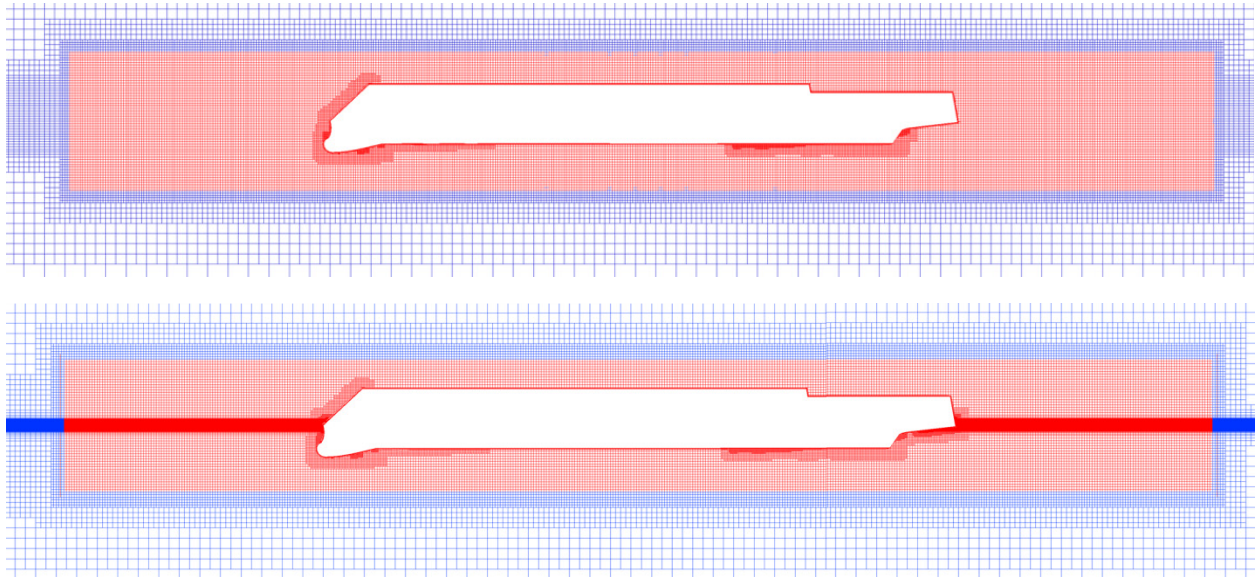


Figure 39. Overset (red) and background (blue) mesh: incident waves of 7.7 m amp. (top) and 1.28 m amp. (bottom)

The main difficulties in implementing free surface waves in a CFD simulation are generation at the inlet, resolution of the wave through the domain without dissipation, and outflow without reflection. Some experimentation was utilized in selecting the boundary conditions and mesh structure which best satisfied these criteria. The 5th order Stokes wave theory is used to specify boundary and initial conditions according to a close approximation of the nonlinear wave profile. A pressure outlet is specified on the downstream, top and bottom faces, symmetry planes are utilized at the centerline and side boundary, and the forward face is a velocity inlet which specifies the transient wave velocity and volume fraction. Turbulence is modeled using the SST $k-\omega$ approach. Six inner iterations are performed during each time step. Forward speed and waves were initialized throughout the domain with no ramping.

4.3.2 Mesh and Time Step Uncertainty

Incident waves of $H/\lambda = 1/10$ were considered for grid and time step uncertainty at zero forward speed. Convergence studies using the approach of *Section 4.2.2* were undertaken using the solutions on four grids and with four time steps. Medium and coarse meshes were

constructed from the fine mesh described in *Section 4.3.1* through progressive increases in cell size by a refinement ratio, $r_g = \sqrt{2}$. An additional extra fine mesh was created by reducing cell size by the same factor. A time step of 0.01 s was used for all grid convergence simulations. Grid uncertainty on the fine mesh was determined using the medium and coarse grids, and uncertainty on the extra fine mesh utilized the solution on fine and medium grids. Time steps of 0.005 s, 0.01 s, 0.02 s and 0.04 s were considered to determine uncertainty due to discretization in time on the fine grid. Uncertainty associated with a time step of 0.01 s was estimated using time steps of 0.02 s and 0.04 s while calculation of the extra fine time step, 0.005 s, uncertainty employed time steps of 0.01 s and 0.02 s.

Convergence study results on the fine grid and using the fine time step are given in Table 13 and Table 15. The time step uncertainty study shows monotonic convergence in all cases except for the mean of the vertical force which converges in an oscillatory manner. Uncertainties of the mean and first harmonic amplitude and phase are between 0.13 and 0.90 %, with the greatest uncertainty typically appearing in the phase. Unlike the prescribed heave and pitch results, a first harmonic approximation matches the solutions well in this case because they resemble a simple trigonometric form. Using the normalization approach, the uncertainty due to time step is between 3.91 and 10.40 %. For the reasons given in *Section 4.2.2* this estimate is likely overly conservative. Plots of the uncertainty time histories are given in Appendix B. In the fine mesh uncertainty study, divergent or oscillatory convergence occurs in the harmonic approach and divergence is shown for the vertical force using normalization. Grid refinement uncertainties for converging quantities in this case are between 43.11 and 89.45 % or 0.69 and 6.08 % for the normalization and harmonic approaches respectively. These values are significantly larger than those due to temporal discretization, and are higher than is expected based on previous uncertainty estimates for periodic ship motion simulations using the same approach [7].

Estimation of uncertainty due to discretization in time using the extra fine time step is shown in Table 15 and the convergence ratio, distance metric and factor of safety are provided in Table 14. Estimates using normalization are between 1.81 and 4.47 %, while the harmonic uncertainties range from 0.04 to 0.67 %. These values are somewhat less than uncertainties due to temporal discretization for the fine time step. Even so, the reduction in numerical error in the extra fine case is minimal and the uncertainty in the fine time step case is also small. The fine time step was consequently accepted for this study and is used in all subsequent simulation results. Estimates of uncertainty due to spatial discretization on the extra fine mesh range from 5.96% to 16.10 % using normalization and 0.45 to 5.88 % in the harmonics. This is a substantial improvement over uncertainty on the fine mesh and is comparable to previous seakeeping simulation uncertainty estimates. Based on this outcome, results in *Section 4.3.3.2* are presented on the extra fine mesh for $H/\lambda = 1/10$ with zero forward speed and at Fn 0.3. Figure 40 shows the extra fine mesh overset and background regions. Approximately 217 cells span the wave length on this refined mesh, with 34 cells across the wave height. The extra fine background mesh is composed of 19.2 million cells with the overset mesh containing 10.2 million cells. Average y^+ values are less than 16 and the maximum CFL number due to phase speed of the incident wave is less than 0.4 with no forward speed and 0.62 with forward speed. A more efficient approach would be to refine locally about areas of interest such as the free surface and body, but the uniform approach to refinement was used here since it is required for estimation of uncertainty.

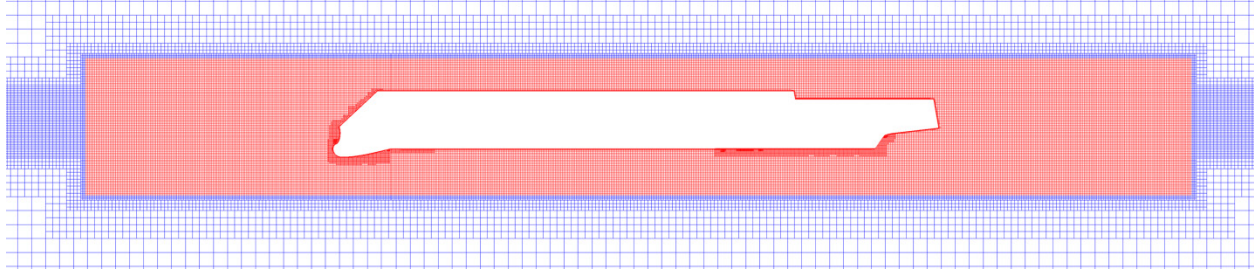


Figure 40. Extra fine mesh; overset (red) and background (blue) mesh: incident waves of 7.7 m amp.

In general, the mesh uncertainty was greater than the time step uncertainty and vertical force was the response most influenced by discretization error. Estimates of uncertainty using the normalization approach may be conservative and are much larger than the uncertainty associated with the mean, first harmonic amplitude and phase. However, because iterative and round-off errors were not assessed, refinement of the boundary layer mesh was uniform in only two-dimensions, and solutions were not in the asymptotic range, there is some ambiguity as to whether a 95 % confidence interval is achieved in the harmonic uncertainties and to what extent the normalization scheme may result in an overly conservative estimate.

Table 13. Verification parameter results: fine mesh, fine time step, $H/\lambda = 1/10$, Fn 0.0

		Grid Convergence			Time Step Convergence		
		R_g	P_g	FS_g	R_t	P_t	FS_t
Normalization	Fx	0.82	0.29	2.20	0.42	0.63	1.91
	Fz	1.01	D	D	0.52	0.47	2.05
	My	0.91	0.13	2.34	0.51	0.48	2.04
Harmonic	Fx₀, Fx₁, θ_{x1}	-0.6, -0.8, -0.8	OC, OC, OC	OC, OC, OC	0.3, 0.2, 0.3	0.8, 1.0, 0.8	1.8, 1.8, 1.8
	Fz₀, Fz₁, θ_{z1}	-1.0, -0.9, -1.1	D, OC, D	D, OC, D	-0.1, 0.3, 0.3	OC, 0.9, 0.9	OC, 1.7, 1.7
	My₀, My₁, θ_{y1}	-0.7, -0.7, -1.1	OC, OC, D	OC, OC, D	0.3, 0.05, 0.3	0.8, 2.2, 0.8	1.7, 21.2, 1.8

Table 14. Verification parameter results: extra fine mesh, extra fine time step, $H/\lambda = 1/10$, Fn 0.0

		Grid Convergence			Time Step Convergence		
		R_g	P_g	FS_g	R_t	P_t	FS_t
Normalization	Fx	0.58	0.80	1.77	0.57	0.41	2.10
	Fz	0.27	1.88	1.95	0.52	0.47	2.05
	My	0.67	0.58	1.95	0.42	0.63	1.91
Harmonic	Fx₀, Fx₁, θ_{x1}	-0.1, -0.3, -0.7	OC, OC, OC	OC, OC, OC	-0.0, -0.4, 0.2	OC, OC, 1.1	OC, OC, 3.9
	Fz₀, Fz₁, θ_{z1}	-0.2, -0.2, -0.3	OC, OC, OC	OC, OC, OC	0.4, -0.1, 0.2	0.7, OC, 1.3	1.9, OC, 6.2
	My₀, My₁, θ_{y1}	-0.2, -0.2, -0.8	OC, OC, OC	OC, OC, OC	0.6, -3, 0.1	0.3, D, 1.5	2.2, D, 9.4

Table 15. Grid and time step uncertainties, $H/\lambda = 1/10$, $Fn = 0.0$

		Fine Mesh, Time Step		Extra Fine Mesh, Time Step	
		U_g	U_t	U_g	U_t
Normalization	Fx	43.11 %	3.91 %	5.96 %	4.47 %
	Fz	D	10.40 %	16.10 %	5.12 %
	My	89.45 %	6.85 %	9.99 %	1.81 %
Harmonic	Fx₀, Fx₁, θ_{x1}	1.19, 5.07, 0.69 %	0.55, 0.42, 0.88 %	0.73, 4.12, 0.58 %	0.30, 0.36, 0.21 %
	Fz₀, Fz₁, θ_{z1}	D, 6.08, D %	0.36, 0.87, 0.76 %	5.88, 5.65, 1.32 %	0.04, 0.67, 0.23 %
	My₀, My₁, θ_{y1}	2.51, 3.54, D %	0.16, 0.13, 0.90 %	1.70, 2.53, 0.45 %	0.45, D, 0.17 %

4.3.3 Force and Moment Results

Results from STAR-CCM+ are given for total force and moment over one wave period and are compared with potential flow results from the Force Study. The free surface elevation, *eta*, is measured at the center of gravity position in the x-direction. For the RANS solution with no forward speed, the actual wave profile was measured at this location in an additional simulation with no body present so that an accurate representation was obtained without the influence of diffracted waves. In the forward speed case, diffracted waves propagate downstream, and the wave profile was monitored at the center of gravity in the x-direction and 250 m to starboard of the centerline. RANS results are shifted in time such that the initial zero crossing point of the wave profile matches with that of the potential flow codes. Simple harmonic waves are considered by codes in the Force Study with the exception of NFA which is an Euler code and calculates nonlinear waves. Results from NFA are provided only for forward speed and high wave steepness, and NSHIPMO results are only given for the smaller wave amplitude examined. Figure 41 and Figure 42 show the results for waves of amplitude 1.28 m at zero forward speed and $Fn = 0.3$ respectively. Results for amplitude 7.7 m are given in Figure 43 and Figure 44 for zero forward speed and $Fn = 0.3$ in turn.

4.3.3.1 $H/\lambda = 1/60$

No systematic study of time step size and mesh refinement was conducted for $H/\lambda = 1/60$. A time step of 0.01 s and the mesh shown in Figure 39 were used for results presented in this section. It was found that additional refinement below the waterline was necessary in this case in order to accurately capture the wave elevation and associated pressure and velocity profiles. Refinement to capture the wave height about the mean waterline did not extend sufficiently far below the surface. This area of added refinement is visible forward of the overset region in the low amplitude wave mesh of Figure 39. For this mesh, maximum CFL numbers due to phase speed are 0.25 and 0.44 for zero forward speed and $Fn = 0.3$ respectively. Typically y^+ values are less than 17.

At $H/\lambda = 1/60$, the force and moment responses are approximately linear for RANS and potential flow results. The $Fn = 0.0$ RANS wave elevation in Figure 41 displays a higher peak and shallower trough relative to the linear approximation which is characteristic of nonlinear waves. This free surface nonlinearity is not significant and appears to have little effect on the forces and

moment experienced by the body in this case. Potential flow results shown in Figure 41 are differentiated primarily by the code rather than the theory on which they are based. Interpretation of these differences is challenging because they are based on variations in how each code represents incident waves and calculates pressure on the hull. For instance: second order pressure terms are employed by the LAMP suite of codes and NSHIPMO but not in other codes, Wheeler stretching is used in NSHIPMO to correct the pressure within a linear wave while the LAMP codes use the fully nonlinear Bernoulli equation to compute pressure, and LAMP includes extra grid velocity terms even when there is no grid motion such that LAMP-1 force and moment computations do not match those computed by other linear codes [2]. The blended strip-theory code, FREDYN, displays the greatest variation from other potential flow methods. This is evident especially in the pitch moment and lateral force response of Figure 41. Vertical force solutions are the most inconsistent since deviation from the mean hydrostatic force is small. Grouping of solutions by the potential flow code rather than theory is most evident in this component, and the RANS vertical force response does not reach a periodic steady state. In general, lateral force and pitch moment results agree reasonably well between RANS and potential flow methods for this low wave steepness and zero forward speed.

Force and moment results at $F_n 0.3$ with $H/\lambda = 1/60$ shown in Figure 42 are mainly distinguished from potential flow solutions by inclusion of forward speed effects, though additional differences occur which are difficult to decipher as in the zero forward speed case. Lateral force in the negative x-direction from RANS is generally greater than the potential flow solutions due to inclusion of frictional resistance. As in the low amplitude and frequency prescribed motion cases, a sinkage effect is evident in the vertical force component. Because they include a steady sinkage force, the LAMP codes are able to match the RANS vertical force result rather well compared to other potential flow codes. Pitch moment results agree well between the LAMP suite of codes, NSHIPMO and RANS.

4.3.3.2 $H/\lambda = 1/10$

Modeling of the nonlinear wave using the inherently nonlinear free surface boundary conditions of RANS with a VOF technique provides a more accurate definition of the incident wave's kinematics and pressures near the free surface as compared to potential flow simulations. This ultimately has a significant impact in determining the total fluid force on the body. For $H/\lambda = 1/10$ the incident wave nonlinearity of the RANS simulation is substantial, possessing a peak about 20% higher and trough 22% shallower than the linear wave amplitude of 7.7 m. Phase velocity is weakly dependent upon the wave height in the nonlinear case, a phenomenon referred to as amplitude dispersion. Waves of larger height travel faster and in this case the average RANS wave period is 9.46 s whereas the linear prediction is 9.93 s. The larger height of the nonlinear wave peak has a secondary effect in this case; because the nonlinear peak is above the weather deck, shipping of green water occurs. This is shown in the time lapse of wave propagation past the body in Figure 45. Green water on deck does not appear to significantly affect the total force and moments experienced by the body however. In the linear and nonlinear wave representations the trough is below the draft of the ship which caused difficulty for some potential flow codes such as the noisy LAMP-4 result [2]. Despite the significant wave height, and nonlinearity in the RANS wave profile, the total force and moment results in Figure 43 do not deviate substantially from a simple trigonometric form for potential flow or RANS. No clear delineation between potential flow theories is apparent in the results and the RANS solution is not well matched by any single code. Interestingly, the RANS vertical force response matches

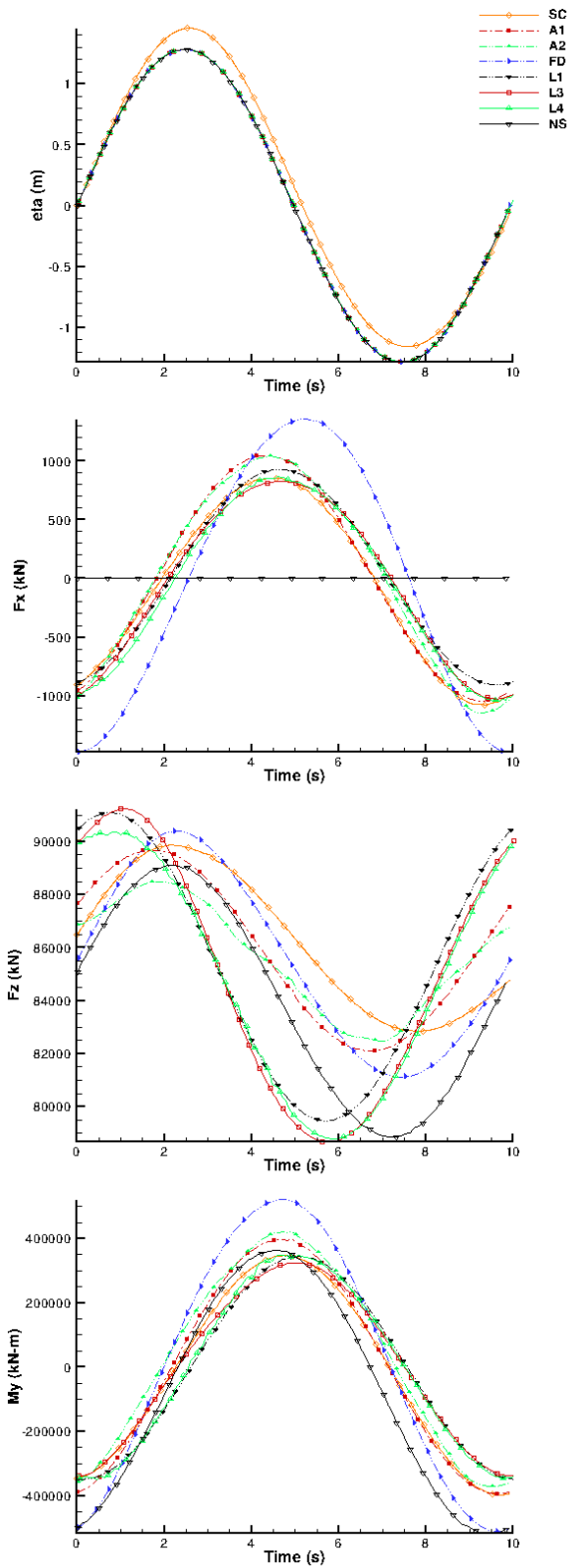


Figure 41. $H/\lambda = 60$ and $Fn = 0.0$: wave elevation (top), longitudinal force (1st middle), vertical force (2nd middle) and pitch moment (bottom)

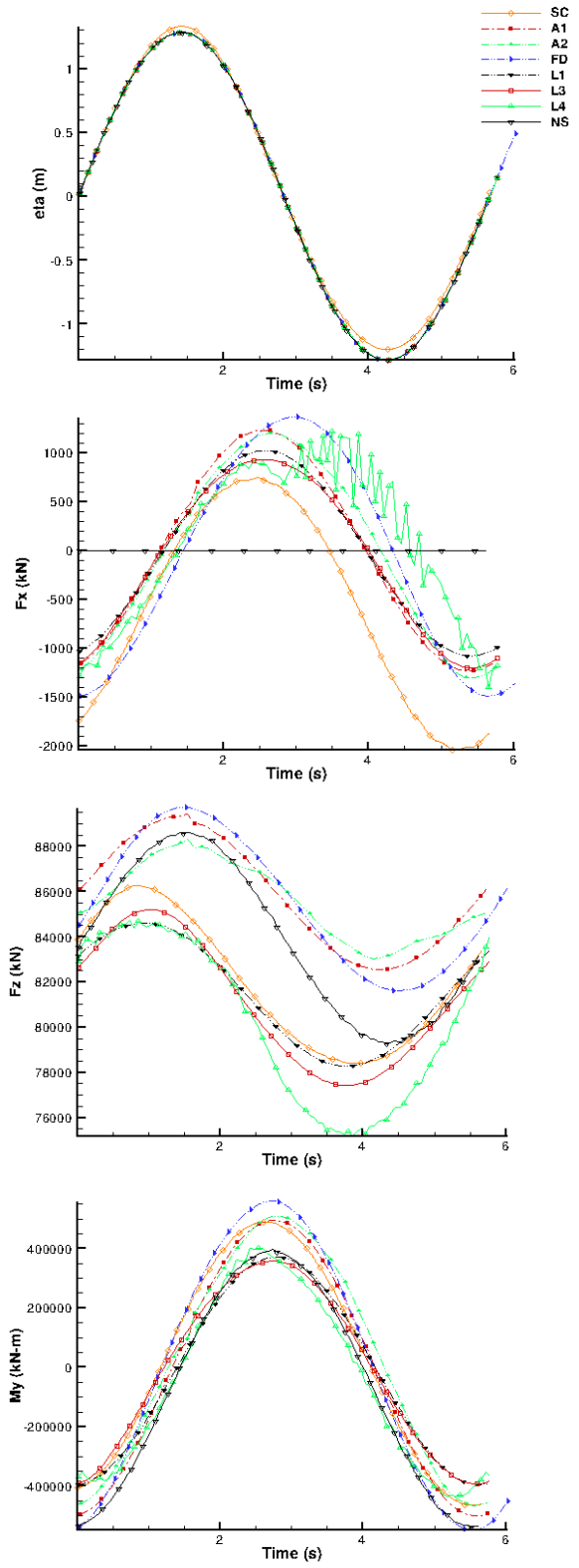


Figure 42. $H/\lambda = 60$ and $Fn = 0.3$: wave elevation (top), longitudinal force (1st middle), vertical force (2nd middle) and pitch moment (bottom)

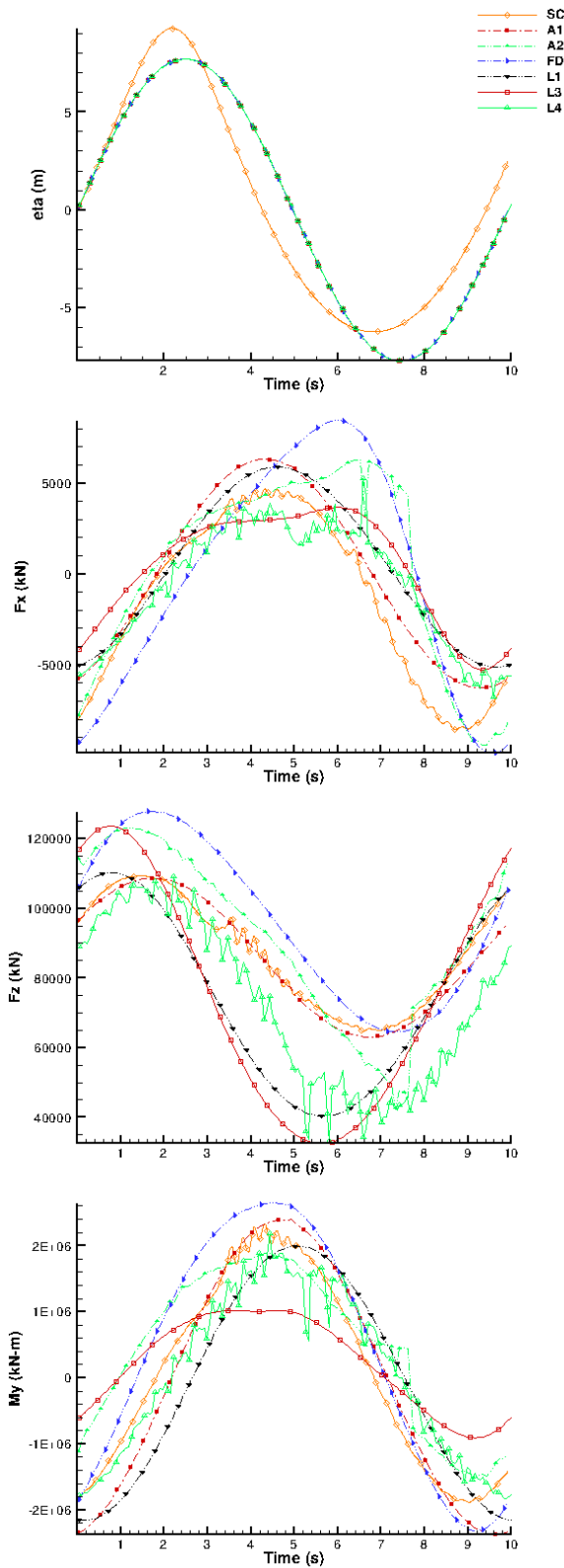


Figure 43. $H/\lambda = 10$ and $Fn 0.0$: wave elevation (top), longitudinal force (1st middle), vertical force (2nd middle) and pitch moment (bottom)

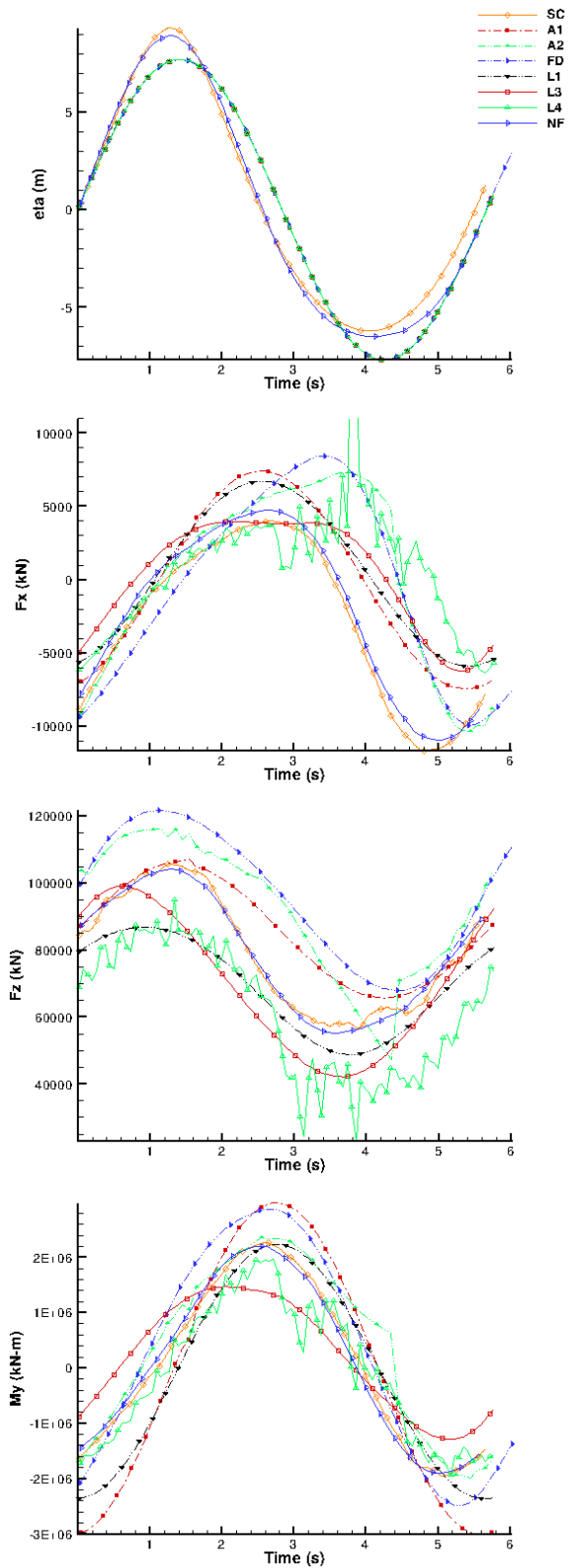


Figure 44. $H/\lambda = 10$ and $Fn 0.3$: wave elevation (top), longitudinal force (1st middle), vertical force (2nd middle) and pitch moment (bottom)

that of the linear code Aegir-1, though this may simply be by coincidence. The character of the LAMP-4 nonlinear potential flow result generally agrees with RANS, but the amplitudes often differ substantially and a phase difference is evident towards the end of the period. This difference in phase occurs in all potential flow results and is due to the amplitude dispersion effect in the RANS solution mentioned previously. Because the RANS results were shifted in time such that the initial zero crossing point of the wave elevation matches the potential flow solutions, this phase difference becomes most evident at the end of the period examined.

In the forward speed case with $H/\lambda = 1/10$ the NFA solution is available for comparison. Its wave profile agrees well with the STAR-CCM+ solution since both codes resolve the nonlinear wave using a VOF approach. There is some difference however at the peaks, and most noticeably in the phase and magnitude of the trough. It is unknown what boundary and initial conditions were utilized in running the NFA code for this case, but STAR-CCM+ solutions using linear wave initial and inlet boundary conditions showed behavior similar to that in the NFA wave elevation plot. Although linear wave input conditions are specified, the inherently nonlinear free surface calculations performed in STAR-CCM+ cause the linear wave profile to deform toward its true nonlinear profile as it propagates through the domain. For this reason, 5th order Stokes theory instead of a linear approximation was specified as the inlet boundary and initial conditions for the included STAR-CCM+ results. The difference in wave profile between NFA and STAR-CCM+ near the end of the period has some effect on the lateral force results at this time. With this exception, the NFA and STAR-CCM+ force and moment results match almost exactly. Yet agreement with potential flow solutions is generally poor and, as in previous cases, the variation between potential flow solutions is without order. The average period of the RANS result is 5.51 s compared to a linear prediction of 5.67 s due to amplitude dispersion.

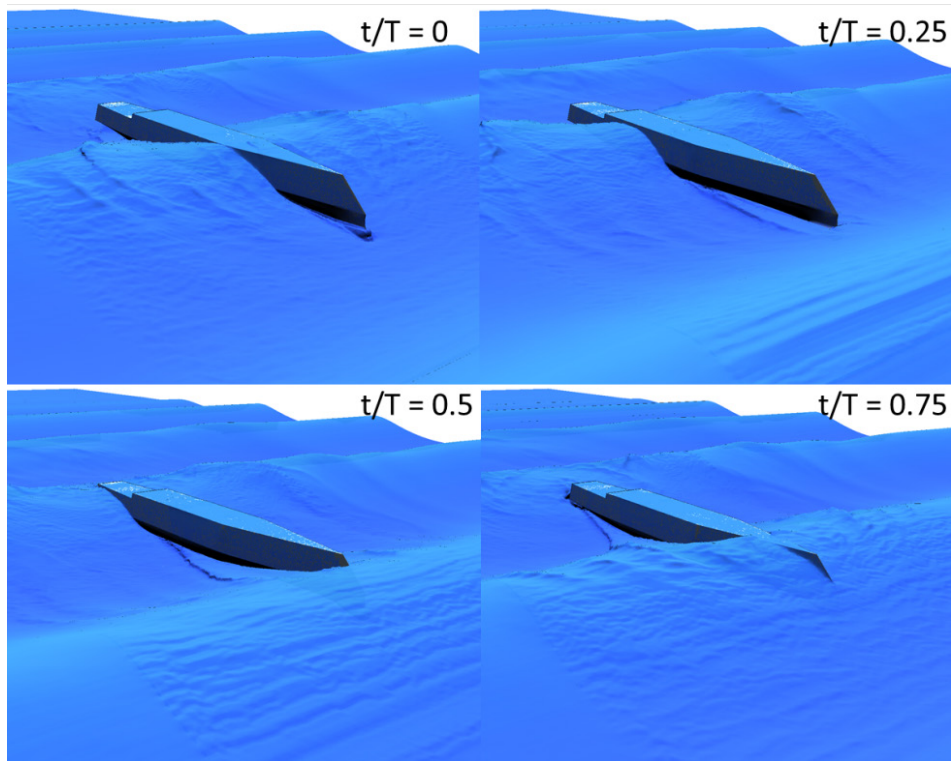


Figure 45. Time lapse of free surface at $t/T = 0, 0.25, 0.50, 0.75$: $F_n 0.0, H/\lambda = 1/10$

4.3.4 Influence of Overset Mesh Interpolation

Errors in the free surface elevation originate at the boundary between overset and background regions in the STAR-CCM+ RANS result and propagate through the overset region. These are visible as small perturbations in the free surface local to the overset region in Figure 45, and may stem from interpolation and a sharp change in cell aspect ratio at the boundary between background and overset mesh regions. In addition, wave reflections were seen to occur from the overset boundary, where the cell aspect ratio changes by a factor of two, at both $H/\lambda = 1/60$ and $H/\lambda = 1/10$ with zero forward speed. Using the STAR-CCM+ meshing tool, avoiding a change in aspect ratio at this point is difficult. The influence of reflections at the overset boundary is most evident in Figure 41. Here the peak and trough of the measured RANS wave elevation for $Fn = 0.0$ and $H/\lambda = 1/60$ are somewhat above that for the same wave steepness at forward speed, and a slight difference in phase appears relative to the linear potential flow solutions. At $Fn = 0.3$, similar reflections did not appear to occur.

In order to assess the impact of overset mesh interpolation on the force and moment response, additional simulations were run with zero forward speed. A fixed mesh similar to that shown in Figure 39 and Figure 40 for $H/\lambda = 1/60$ and $H/\lambda = 1/10$ respectively was employed with no overset mesh or corresponding interpolation. A transition in the cell aspect ratio remained where the mesh was refined near the body. The resulting force and moment time histories are compared to overset mesh solutions for the same excitation period in Figure 46 and Figure 47. Some difference in the solutions due to overset mesh interpolation is seen, particularly for $H/\lambda = 1/60$ and vertical force at $H/\lambda = 1/10$. Perturbations in the free surface remain in the fixed mesh cases within the refined region around the body which previously constituted the overset mesh. These perturbations are thus a consequence of the change in mesh refinement, having occurred on both overset and fixed meshes. No cases were run without a body present on the fixed mesh and consequently wave reflection due to transitions in the cell aspect ratio was not measured.

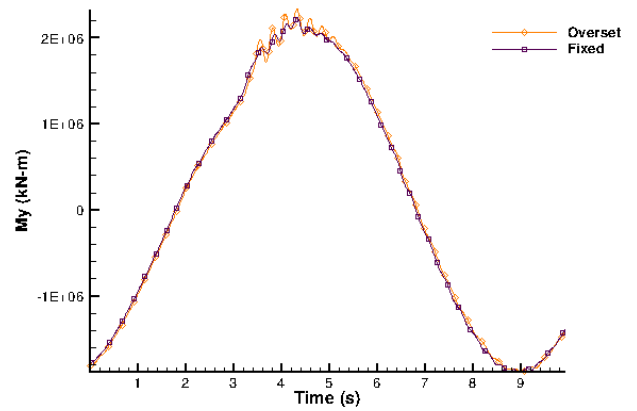
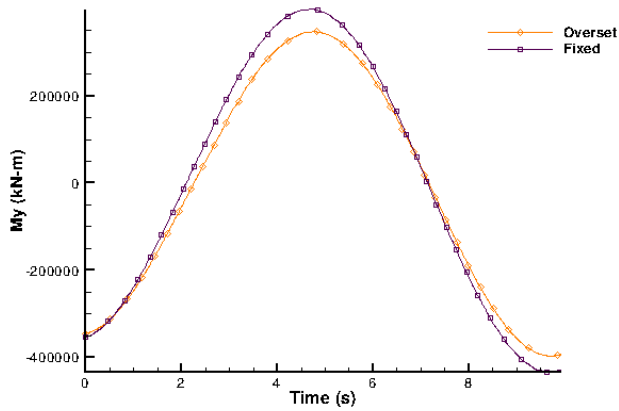
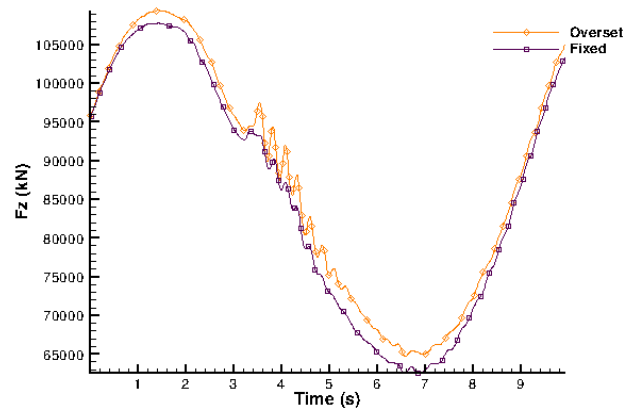
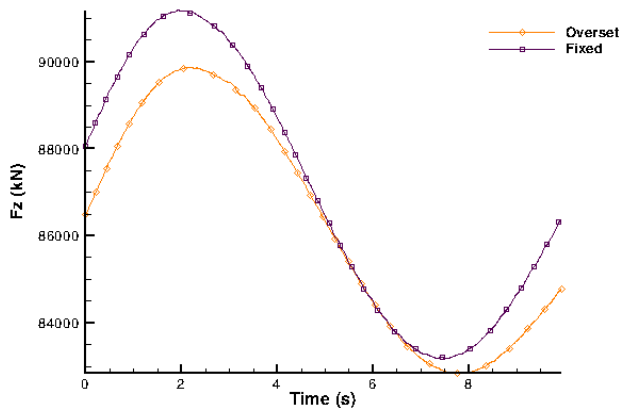
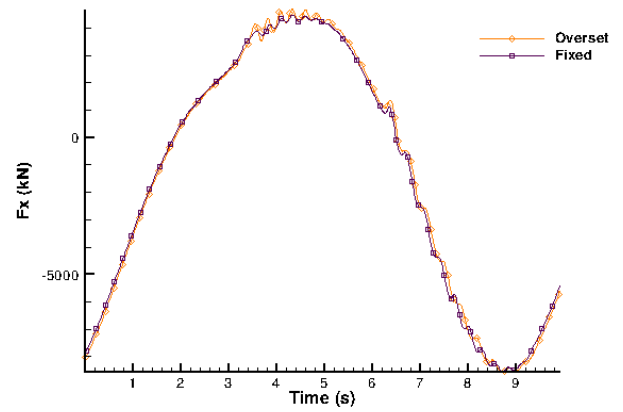
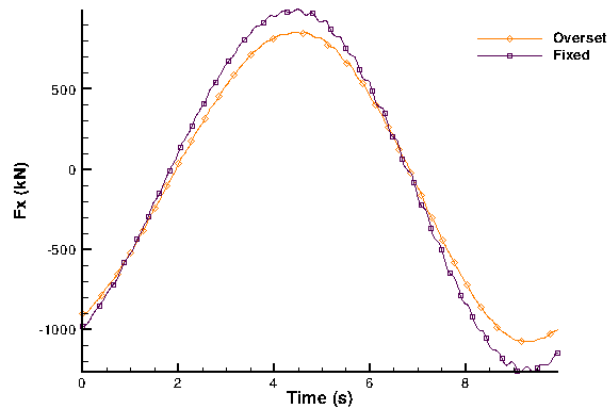


Figure 46. Comparison of overset and fixed mesh solutions; $H/\lambda = 60$ and $Fn = 0.0$: longitudinal force (top), vertical force (middle) and pitch moment (bottom)

Figure 47. Comparison of overset and fixed mesh solutions; $H/\lambda = 10$ and $Fn = 0.0$: longitudinal force (top), vertical force (middle) and pitch moment (bottom)

5 SUMMARY, CONCLUSIONS AND FUTURE WORK

5.1 SUMMARY

The STAR-CCM+ RANS solution was first validated for a two-dimensional rectangular cylinder oscillating in an unbounded fluid via comparison with the analytical potential flow result. A calm free surface was then added and the rectangular cylinder was oscillated at several amplitudes and over a range of frequencies in heave and sway. At low frequencies, bottom effects due to the finite depth of the experimental basin were shown to be important. By using an overset mesh, these effects were considered and a good approximation of the experimental hydrodynamic coefficients obtained with RANS. In oscillations of high frequency and amplitude, the influence of viscous effects was demonstrated predominantly for heave motion. The viscosity introduced a nonlinear, time-dependent component to the hydrodynamic force on the body in these cases. Which turbulence model was chosen impacted the viscous flow features and thus the time histories of force and approximations of added mass and damping. In general, RANS and linear potential flow methods were shown to match experimental added mass and damping coefficients for the two-dimensional rectangle in heave and sway about a calm free surface well, though the RANS solution provided better agreement for high amplitude and frequency oscillations in heave and in the coupling coefficients between sway motion and roll moment response.

A three-dimensional radiation problem was considered in which the full-scale ONR Tumblehome hullform was oscillated according to 1-DoF prescribed heave and pitch motions. Combinations of amplitude and frequency of oscillation ranging from small to large were considered at zero forward speed and F_n 0.3 such that responses in both the linear and nonlinear regime might be evaluated. Motion of the body was permitted in STAR-CCM+ using an overset mesh approach. Uncertainty in the numerical result due to discretization was assessed through a systematic refinement study of the mesh and time step. Calculations of force and moment on the body by the RANS solver were compared with established solutions from potential flow codes with theories ranging from linear to blended to nonlinear. Linear potential flow methods provided poor approximations for large amplitude motions in which geometric nonlinearity was significant, and blended approaches did not match nonlinear potential flow and RANS results well for high amplitude and frequency cases in which nonlinear radiation forces were important. In general, the character of the RANS and nonlinear potential flow solutions agreed well. To some extent, nonlinearity in the free surface and viscous effects may have caused differences between these method's results in the most extreme cases considered; heave and pitch with 4.4 m or 5 degree amplitude and 1.1 rad/s frequency. Regardless, the primary nonlinearities were those associated with the changing wetted hull form and radiation force.

The ONR Tumblehome was also examined in a three-dimensional diffraction problem in which incident head waves impacted the fixed body at zero forward speed or F_n 0.3. Two wave conditions were considered, with wave steepness $H/\lambda = 1/60$ and $1/10$ and the wavelength, λ , equal to the ship length. Mesh and time step uncertainty were determined for $H/\lambda = 1/10$, and all solutions were compared with previous results from the same potential flow codes used in the radiation problem. In the low amplitude wave case, the force and moment results were approximately linear, and agreed reasonably well between RANS and potential flow codes for pitch moment and lateral force at zero forward speed. Vertical force responses were small relative to the hydrostatic force and differed substantially though there was no systematic variation in potential flow results due to the underlying theory as in the prescribed motions case.

Instead, inconsistencies in the results reflected, at least in part, on differences in how the codes treated incident waves, calculated pressures and handled the complex geometry. Nonlinearity in the wave representation was substantial in the RANS solution for the large amplitude wave condition, while all potential flow methods considered only a simple harmonic representation. This led to substantial differences in the wave profile, and corresponding discrepancies in the force and moment results. There was no meaningful grouping of potential flow solutions, and their agreement with the RANS result was poor although the forces and moments were approximately linear. The RANS result did agree well with an Euler code of similar formulation which was run with the potential flow methods only for the large amplitude wave case at forward speed.

5.2 CONCLUSIONS AND FUTURE WORK

A comparison was made between the commercial CFD code STAR-CCM+ as a RANS solver and several potential flow methods in the calculation of forces and moments on bodies in vertical plane radiation and diffraction seakeeping problems. The aim was to correlate the characteristics of each solution method with differences in the results in order to show the significance of particular sources of nonlinearity. Linear potential flow methods are still the most common approach to seakeeping computations for design due to their speed and adequate results for simple cases. Blended and nonlinear potential flow approaches account for the most significant nonlinearities which are associated with the changing underwater hull shape. Yet in some cases, the nonlinear, time-dependent nature of viscous phenomenon and the free surface have a considerable effect on the resulting pressure force on the body. The main advantage of RANS is its capability to model all of the nonlinear effects, including those due to viscosity, large deformations of the free surface and the behavior of incident, radiated and diffracted waves. In addition, RANS is able to provide detailed local flow information useful for examination of particular flow phenomenon. While potential flow methods generally offer an efficiency advantage over RANS, even the more subtle nonlinearities may have a considerable influence on predictions of hull motion in waves. RANS thus has the potential to produce superior results in the prediction of a ship's dynamic response in the vertical plane and, to a greater extent, in motions where viscous effects are more prominent such as roll. Future work will be to extend the present simulations in STAR-CCM+ to permit free heave and pitch motion of a ship in head waves. Comparison with experimental data will provide validation of the RANS approach and models. This is sought first for small amplitude waves, which have been studied previously using RANS and shown good agreement with experiments (e.g. [10]). Eventually it is hoped that validation of large amplitude motions in the vertical plane and in coupled vertical and horizontal plane motions is achieved.

REFERENCES

- [1] P. J. Finn, R. F. Beck, A. W. Troesch, and Y. S. Shin, "Nonlinear Impact Loading in an Oblique Seaway," *Journal of Offshore Mechanics and Arctic Engineering*, vol. 125, p. 190, 2003.
- [2] J. G. Telste and W. F. Belknap, "Potential Flow Forces and Moments from Selected Ship Flow Codes in a Set of Numerical Experiments (CD-ROM)," DTIC Document 2008.
- [3] N. Salvesen, E. Tuck, and O. Faltinsen, "Ship motions and sea loads," *Trans. SNAME*, vol. 78, pp. 250-287, 1970.
- [4] R. Beck and A. Reed, "Modern seakeeping computations for ships," in *Twenty-Third Symposium on Naval Hydrodynamics*, 2001.
- [5] M. S. Longuet-Higgins, E. Cokelet, M. Longuet-Higgins, and E. Cokelet, "The deformation of steep surface waves on water. I. A numerical method of computation," *Proceedings of the Royal Society of London. A. Mathematical and Physical Sciences*, vol. 350, pp. 1-26, 1976.
- [6] A. K. Subramani, "Computations of Highly Nonlinear Free Surface Flows, with Applications to Arbitrary and Complex Hull Forms," Ph.D, University of Michigan, 2000.
- [7] F. Stern, J. Yang, Z. Wang, H. Sadat-Hosseini, M. Mousaviraad, S. Bhushan, *et al.*, "Computational Ship Hydrodynamics: Nowadays and Way Forward," in *29th Symposium on Naval Hydrodynamics*, Gothenburg, Sweden, 2012.
- [8] G. D. Weymouth, R. V. Wilson, and F. Stern, "RANS computational fluid dynamics predictions of pitch and heave ship motions in head seas," *Journal of ship research*, vol. 49, pp. 80-97, 2005.
- [9] P. M. Carrica, R. V. Wilson, R. W. Noack, and F. Stern, "Ship motions using single-phase level set with dynamic overset grids," *Computers & fluids*, vol. 36, pp. 1415-1433, 2007.
- [10] L. Larsson, F. Stern, and M. Visonneau, "Gothenburg 2010, A Workshop on Numerical Ship Hydrodynamics," 2010.
- [11] S. H. S. Hosseini, "CFD prediction of ship capsizing: parametric rolling, broaching, surf-riding, and periodic motions," Ph.D, Mechanical Engineering, University of Iowa, 2009.
- [12] R. Miller, C. Bassler, P. Atsavapranee, and J. Gorski, "Viscous Roll Predictions for Naval Surface Ships Appended with Bilge Keels Using URANS," in *Proc. 27th Symp. Naval Hydro*, 2008.
- [13] W. Belknap, C. Bassler, M. Hughes, P. Bandyk, K. Maki, D. Kim, *et al.*, "Comparisons of Body-Exact Force Computations in Large Amplitude Motion," in *Proc. 28th Symp. on Naval Hydrodynamics*, 2010.
- [14] A. Grasso, D. Villa, S. Brizzolara, and D. Bruzzone, "Nonlinear motions in head waves with a RANS and a potential code," *Journal of Hydrodynamics, Ser. B*, vol. 22, pp. 172-177, 2010.
- [15] T. Bunnik, E. van Daalan, G. Kapsenberg, Y. Shin, R. Huijsmans, G. Deng, *et al.*, "A comparative study on state-of-the-art prediction tools for seakeeping," presented at the 28th Symposium on Naval Hydrodynamics, Pasadena, California, 2010.
- [16] W. Belknap and J. Telste, "Identification of Leading Order Nonlinearities from Numerical Forced Motion Experiment Results," presented at the 27th Symposium on Naval Hydrodynamics, Seoul, Korea, 2008.

- [17] "User Guide STAR-CCM+ Version 7.02 CD-Adapco," ed, 2012.
- [18] J. H. Ferziger and M. Peric, *Computational Methods for Fluid Dynamics*: Springer, 1999.
- [19] F. R. Menter, M. Kuntz, and R. Langtry, "Ten Years of Industrial Experience with the SST Turbulence Model," *Turbulence, Heat and Mass Transfer*, 2003.
- [20] A. Quérard, P. Temarel, and S. Turnock, "Influence of viscous effects on the hydrodynamics of ship-like sections undergoing symmetric and anti-symmetric motions, using RANS," presented at the 27th International Conference on Offshore Mechanics and Arctic Engineering, Estoril, Portugal, 2008.
- [21] L. Bonfiglio, S. Brizzolaro, and C. Chryssostomidis, "Added Mass and Damping of Oscillating Bodies: a fully viscous numerical approach," *Recent Advances in Fluid Mechanics, Heat & Mass Transfer and Biology*, pp. 210-215, 2011.
- [22] J. Vugts, "The hydrodynamic coefficients for swaying, heaving and rolling cylinders in a free surface," Laboratorium voor Scheepsbouwkunde, Technische Hogeschool, Delft, The Netherlands 1968.
- [23] R. W. Yeung, S.-W. Liao, and D. Roddie, "Hydrodynamic Coefficients of Rolling Rectangular Cylinders," *International Journal of Offshore and Polar Engineering*, vol. 8, 1998.
- [24] J. Newman, "Added moment of inertia of two-dimensional cylinders," *Journal of Ship Research*, vol. 23, 1979.
- [25] R. C. Bishop, W. Belknap, C. Turner, B. Simon, and J. H. Kim, "Parametric investigation on the influence of GM, roll damping, and above-water form on the roll response of model 5613," Naval Surface Warfare Center, Carderock Division, Bethesda, MD 2005.
- [26] F. Stern, R. Wilson, and J. Shao, "Quantitative V&V of CFD simulations and certification of CFD codes," *International journal for numerical methods in fluids*, vol. 50, pp. 1335-1355, 2006.
- [27] T. Xing and F. Stern, "Factors of Safety for Richardson Extrapolation," *Journal of Fluids Engineering*, vol. 132, p. 061403, 2010.
- [28] M. P. Ebert and J. J. Gorski, "A Verification and Validation Procedure for Computational Fluid Dynamics Solutions," Naval Surface Warfare Center, Carderock Division, Bethesda, MD 2001.
- [29] H. Sadat-Hosseini, P. C. Wu, P. M. Carrica, H. Kim, Y. Toda, and F. Stern, "CFD verification and validation of added resistance and motions of KVLCC2 with fixed and free surge in short and long head waves," *Ocean Engineering*, vol. 59, pp. 240-273, 2013.
- [30] D. Liut, K. Weems, and W. M. Lin, "Nonlinear Green Water Effects on Ships with Large-Amplitude Motions," presented at the 24th Symposium on Naval Hydrodynamics, Fukuoka, Japan, 2002.
- [31] A. M. Reed, "A Naval Perspective on Ship Stability," in *10th Intl. Conf. Stability of Ships and Ocean Vehicles*, St. Petersburg, Russia, 2011, pp. 793-823.

Appendix A: ONRTH Prescribed motion results

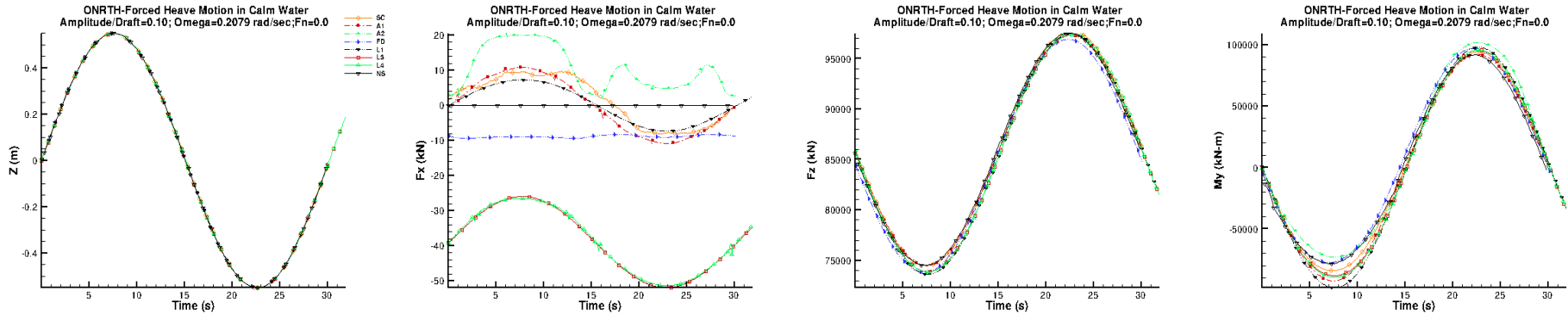


Figure A-1. Prescribed heave: F_n 0.0; z_a 0.55 m; ω 0.2079 rad/s

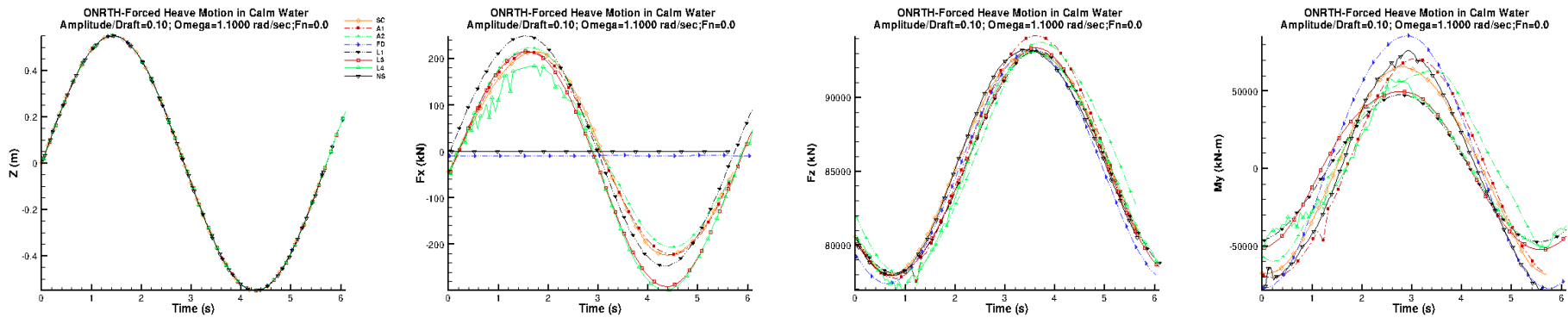


Figure A-2. Prescribed heave: F_n 0.0; z_a 0.55 m; ω 1.1 rad/s

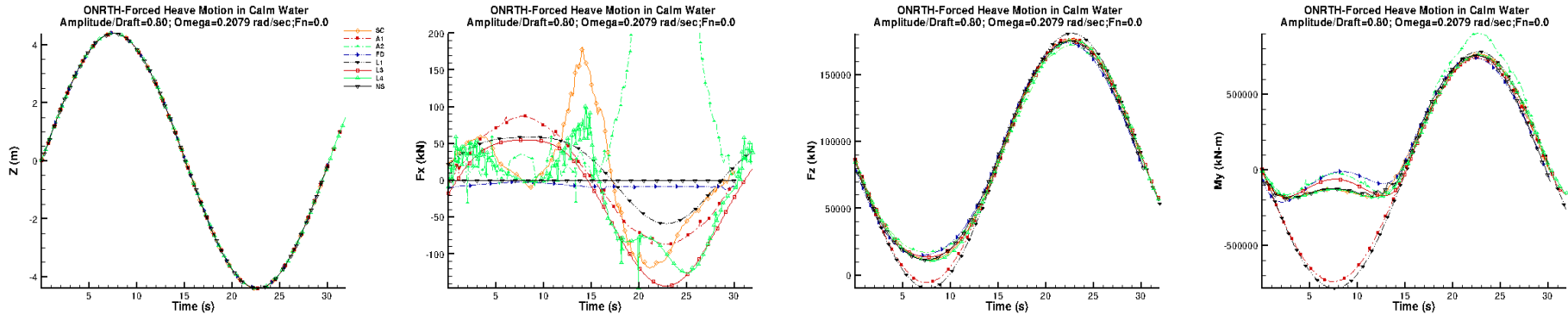


Figure A-3. Prescribed heave: F_n 0.0; z_a 4.4 m; ω 0.2079 rad/s

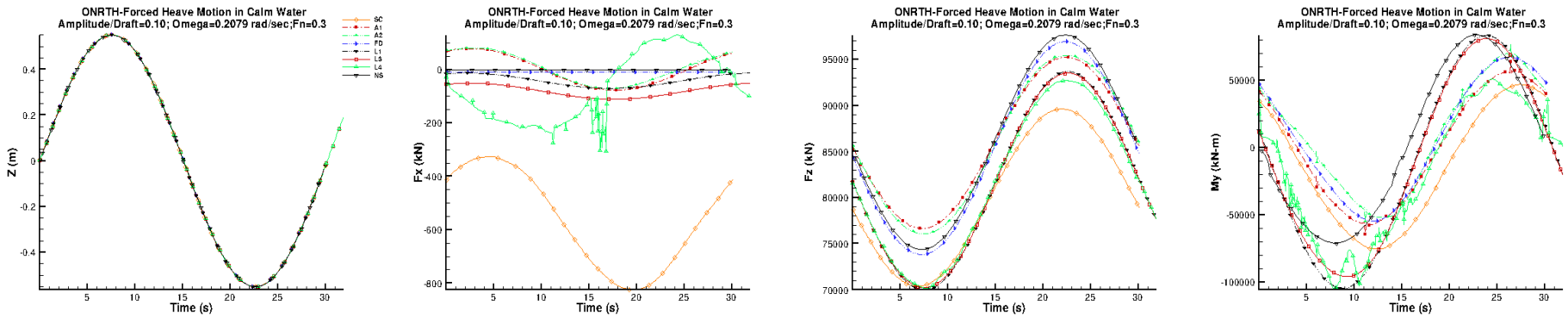


Figure A-4. Prescribed heave: F_n 0.3; z_a 0.55 m; ω 0.2079 rad/s

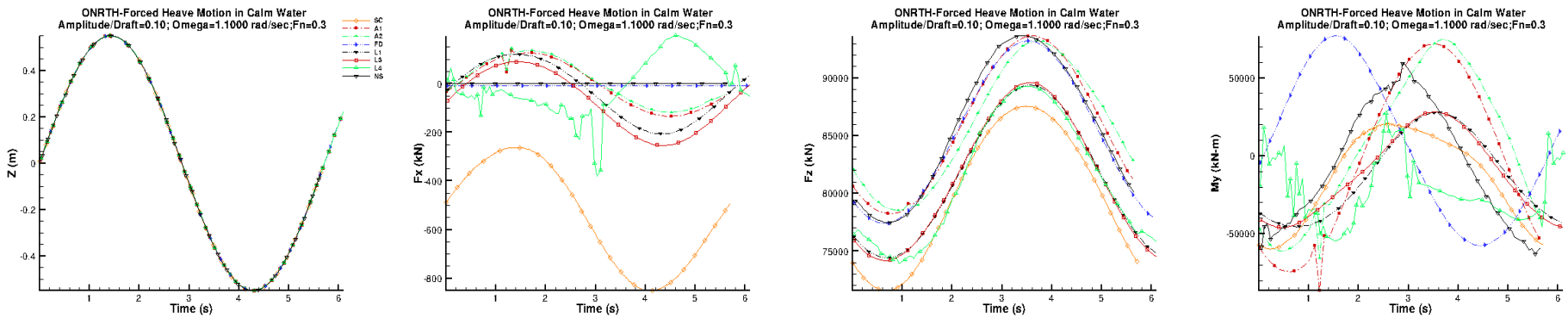


Figure A-5. Prescribed heave: F_n 0.3; z_a 0.55 m; ω 1.1 rad/s

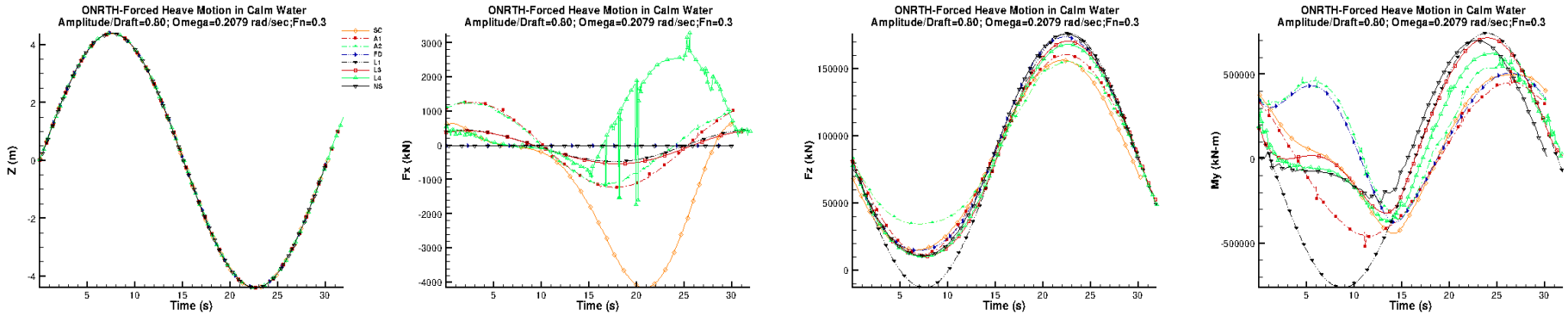


Figure A-6. Prescribed heave: F_n 0.3; z_a 4.4 m; ω 0.2079 rad/s

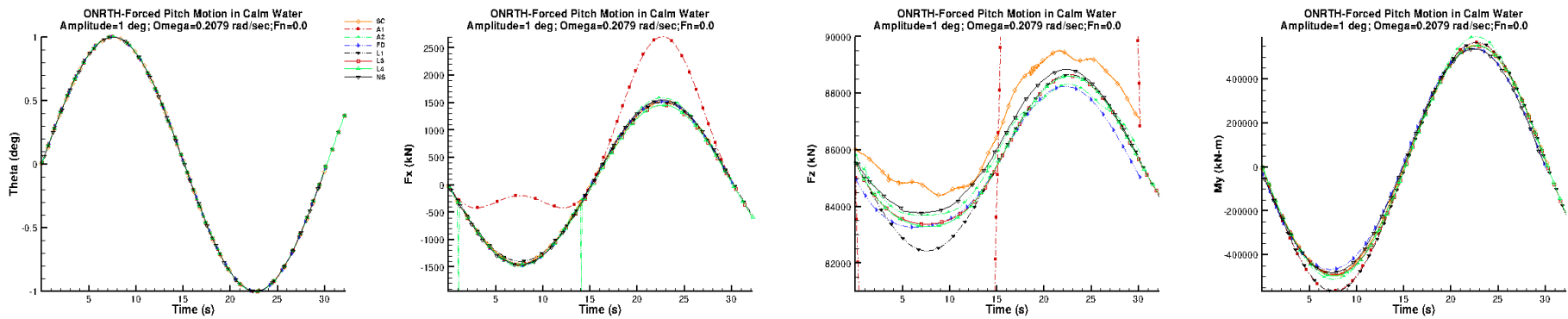


Figure A-7. Prescribed pitch: F_n 0.0; θ_a 1 deg; ω 0.2079 rad/s

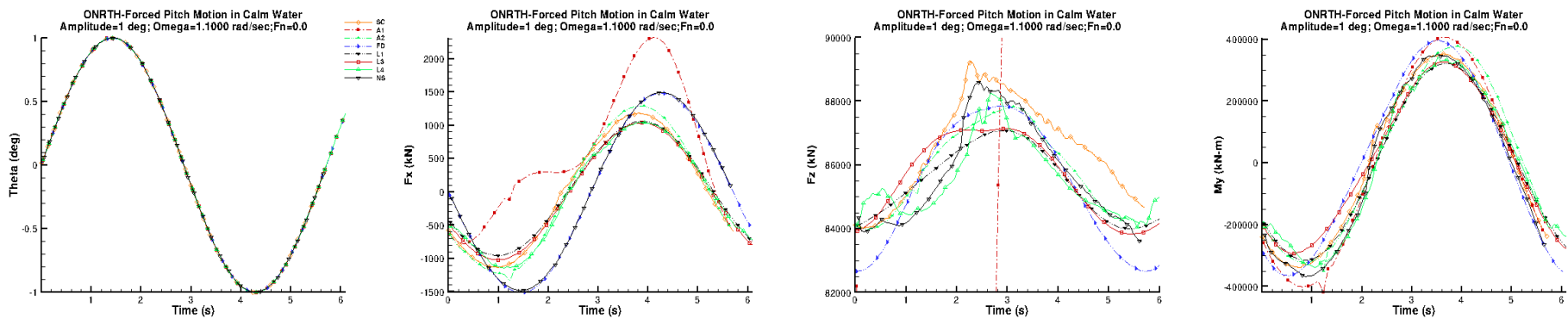


Figure A-8. Prescribed pitch: F_n 0.0; θ_a 1 deg; ω 1.1 rad/s

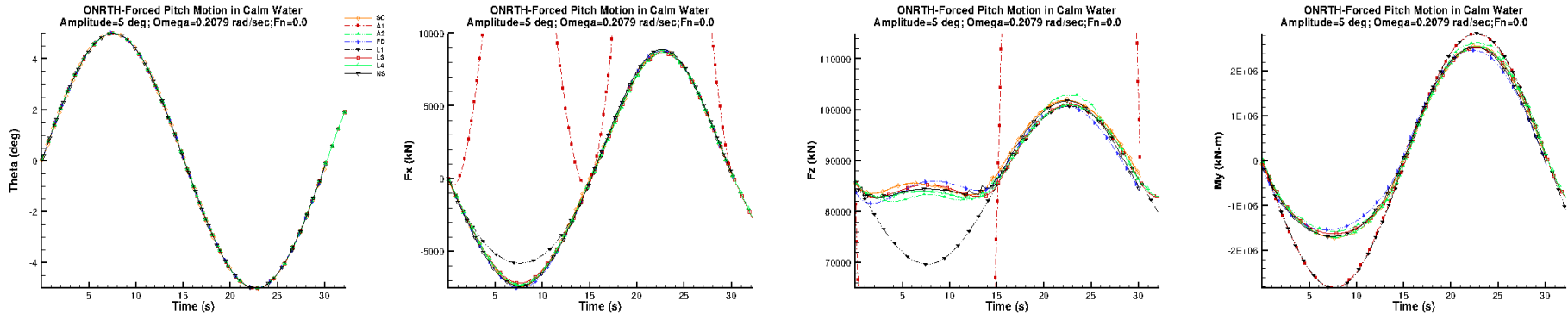


Figure A-9. Prescribed pitch: F_n 0.0; θ_a 5 deg; ω 0.2079 rad/s

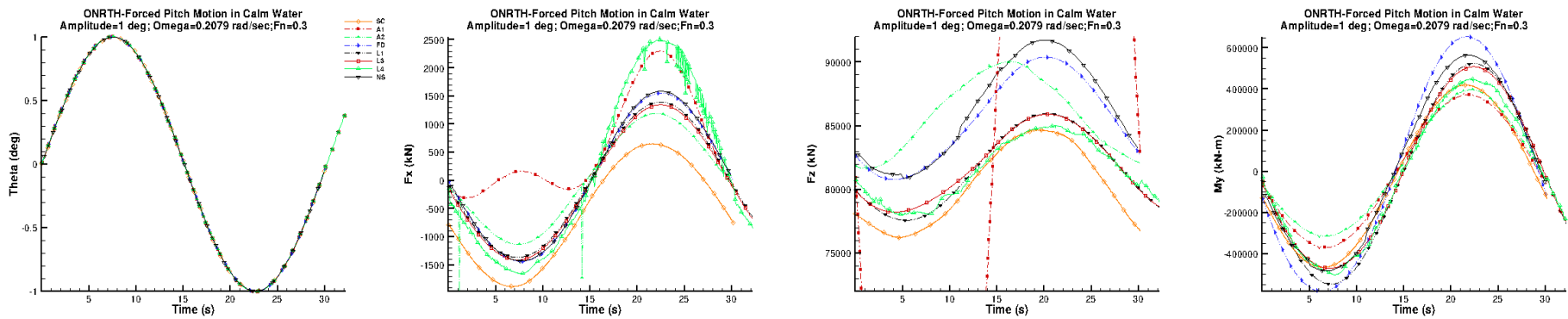


Figure A-10. Prescribed pitch: Fn 0.3; θ_a 1 deg; ω 0.2079 rad/s

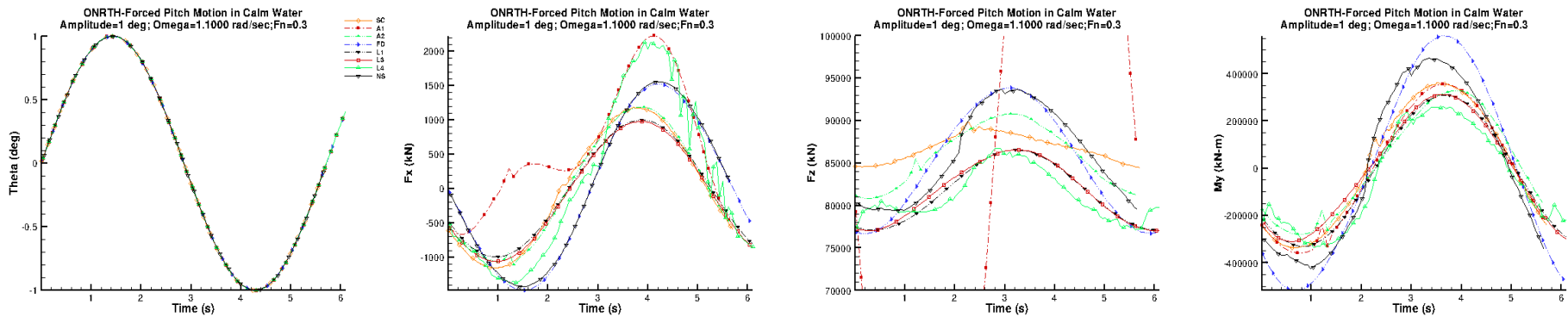


Figure A-11. Prescribed pitch: Fn 0.3; θ_a 1 deg; ω 1.1 rad/s

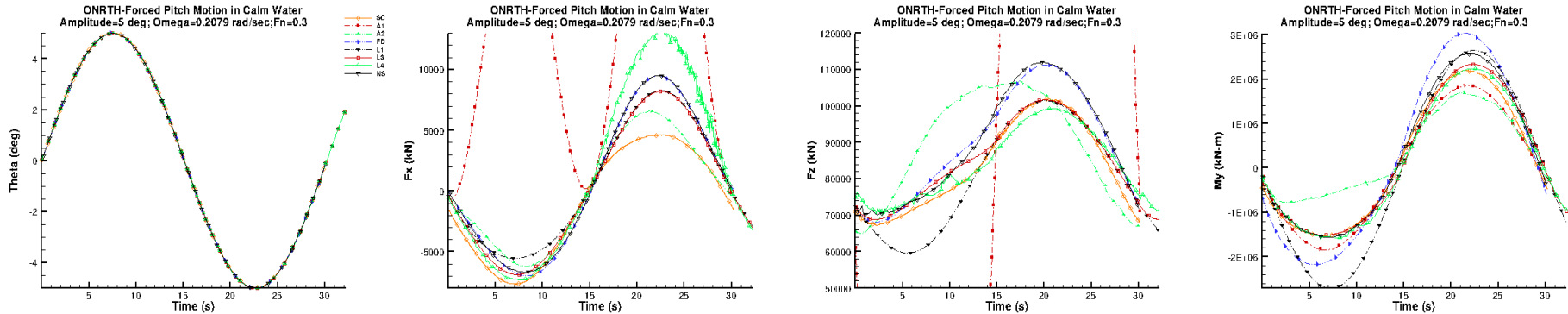


Figure A-12. Prescribed pitch: Fn 0.3; θ_a 5 deg; ω 0.2079 rad/s

Appendix B: ONRTH Incident wave uncertainty time histories

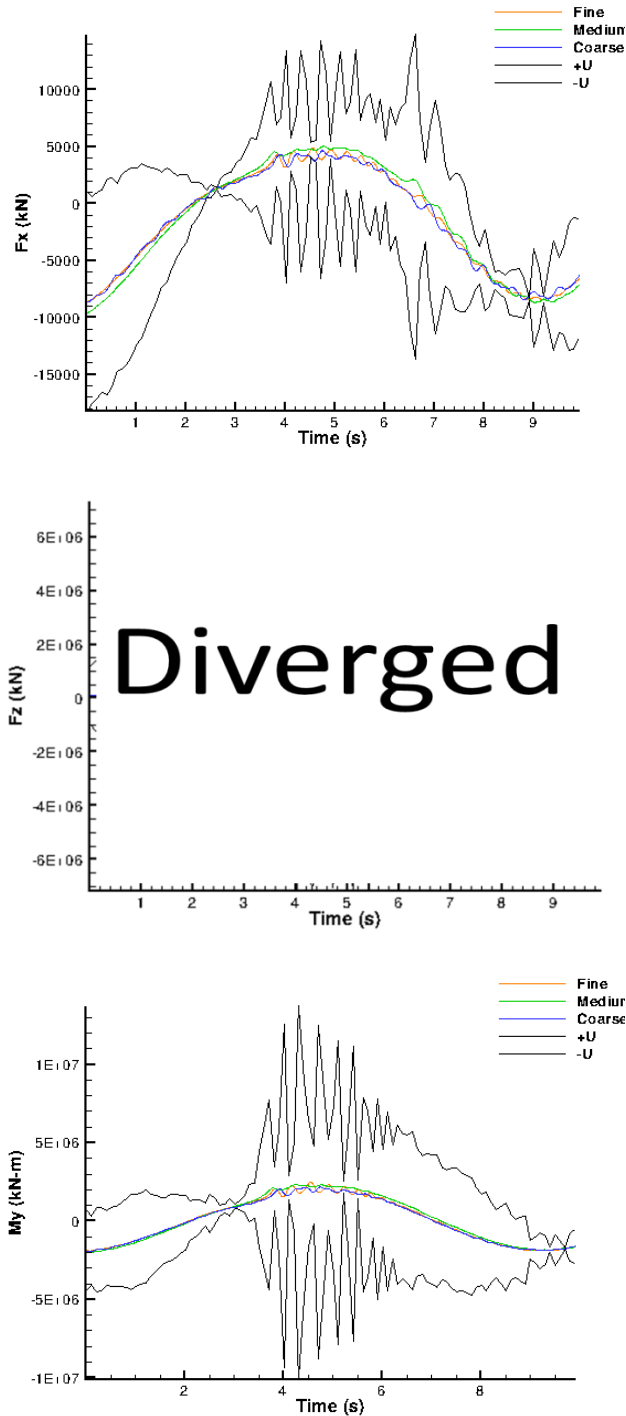


Figure B-1. Fine grid refinement study, $H/\lambda = 1/10$: longitudinal force (top), vertical force (middle) and pitch moment (bottom)

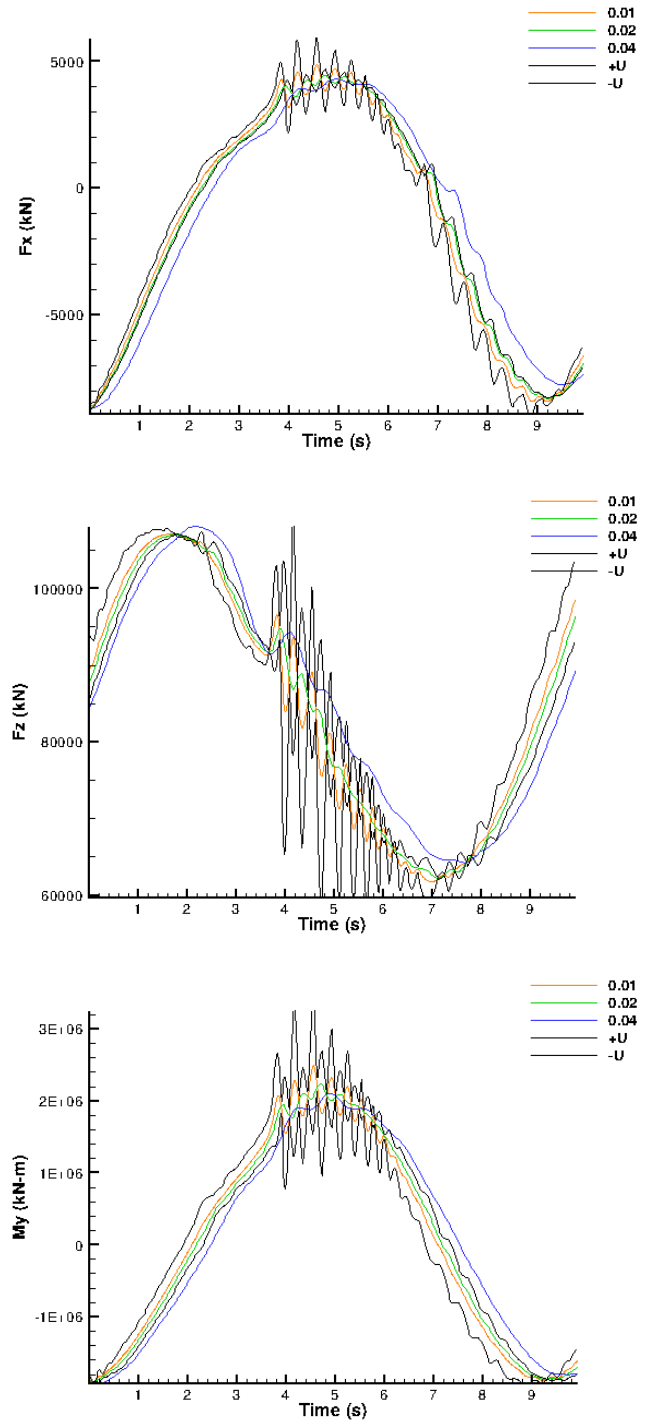


Figure B-2. Fine time step refinement study, $H/\lambda = 1/10$: longitudinal force (top), vertical force (middle) and pitch moment (bottom)

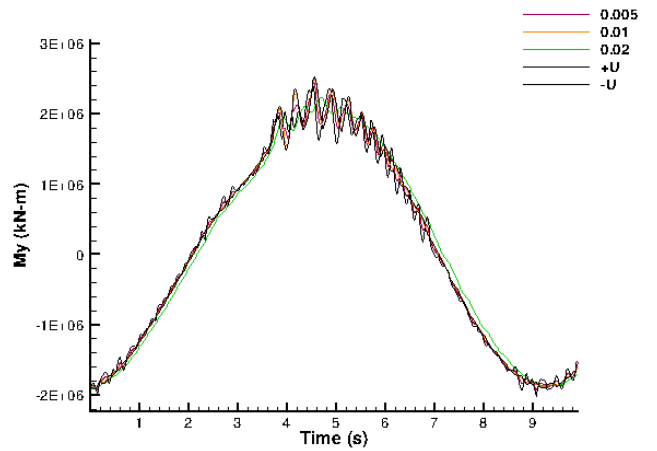
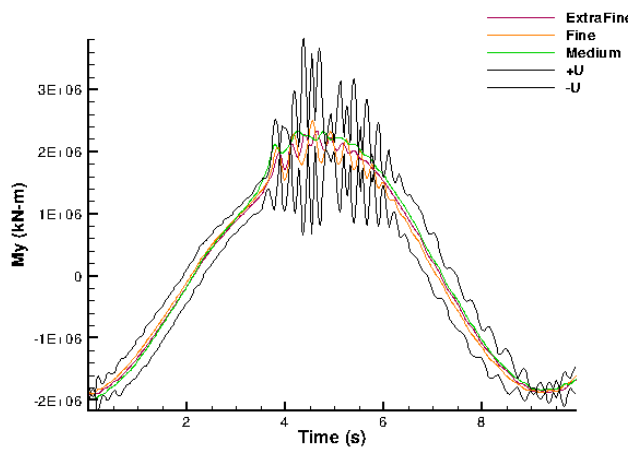
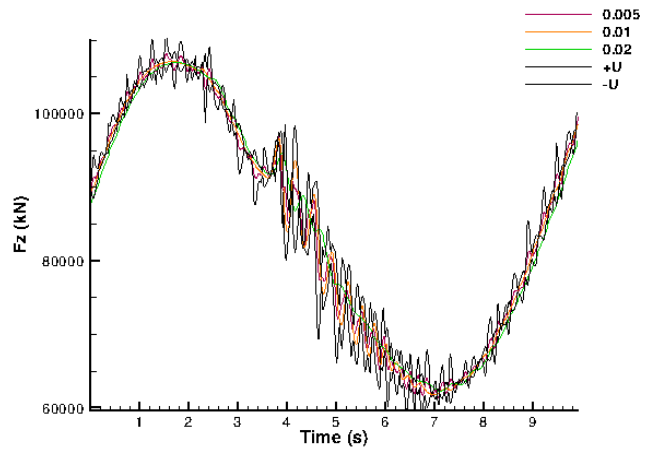
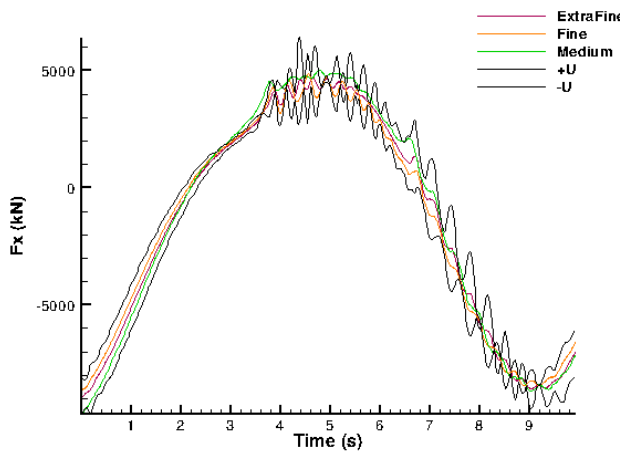
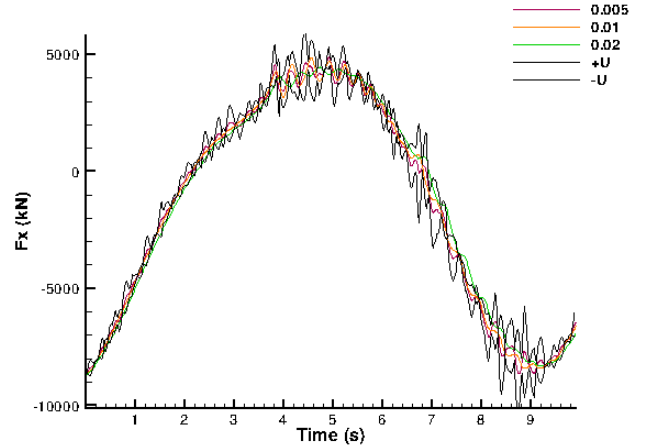
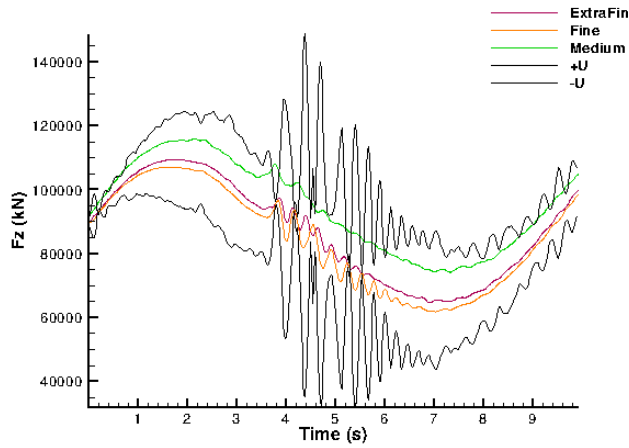


Figure B-3. Extra fine grid refinement study, $H/\lambda = 1/10$: longitudinal force (top), vertical force (middle) and pitch moment (bottom)

Figure B-4. Extra fine time step refinement study, $H/\lambda = 1/10$: longitudinal force (top), vertical force (middle) and pitch moment (bottom)